UNIVERSITY OF CALIFORNIA
SANTA CRUZ

MODELING ASYMMETRY IN THE ROTATION OF DISK GALAXIES

A dissertation submitted in partial satisfaction of the
requirements for the degree of

Doctor of Philosophy

in

ASTRONOMY AND ASTROPHYSICS

by

Brian DiGiorgio

June 2023

The Dissertation of Brian DiGiorgio is approved:

Puragra GuhaThakurta, Chair

Kevin Bundy

Kyle B. Westfall

Peter Biehl
Vice Provost and Dean of Graduate Studies

Table of Contents

List of Figures

Abstract

Modeling Asymmetry in the Rotation of Disk Galaxies

by

Brian DiGiorgio

Galaxy rotation has been studied for over a century, using spectroscopic measurements to construct rotational models that describe the motions of their gas and stars. However, only a small subset of this work has recognized that galaxies are not entirely radially symmetrical, but are instead often disrupted in ways that simple velocity field models cannot capture. In this dissertation, I describe my work modelling nonaxisymmetric galaxy rotation and the astrophysical insights gained from these models.

Gravitational lensing distorts a galaxy's velocity field in a manner distinct from the distortions of its photometric shape, an effect called kinematic weak lensing. This allows for the construction of a model that uses this difference to extract lensing information about the system. I detail the properties and strengths of such a model, finding that for mock observations of source galaxies at moderate redshifts, the signal-to-noise of the lensing measurements improves by up to a factor of six over previous works, enabling the possibility of future lensing studies independent of current weak lensing systematic constraints.

I also describe the development of Nirvana, a Bayesian nonparametric velocity field fitting code designed to describe the bisymmetric motions present in barred galaxies. Using a sample of barred galaxies from the MaNGA survey, I construct the Nirvana-MaNGA sample, which is comprised of velocity field models of > 1000 local

barred galaxies, as well as a matched control sample of unbarred galaxies. Nirvana determines bar strength and location independent of imaging, providing an independent and direct test of dynamical models of higher-order noncircular motions in bars, agreeing with visual bar classifications on bar angle. I also find direct evidence of flattening in stellar population gradients along bar kinematic axes as compared to surrounding disk regions at the same radii, verifying results reliant on visual classifications and affirming the dynamic connection between the presence of bars and radial mixing of stellar populations.

Acknowledgments

I have many people to thank for getting me to where I am today as a student, astronomer, teacher, and scientist.

First, I would like to thank my middle and high school teachers for planting the seeds of my passion for astronomy and my desire to learn. In particular, thank you to Paul Trudelle, whose "earth science" class started me on my path in astronomy and whose lessons I continue to borrow from in my own teaching. Thank you also to Steve Marsheck, for allowing me and my classmates to run wild in our differential equations class and discover mathematics together through inquiry and fun. I went into college knowing who I was as a student and as a learner because of the challenges and opportunities I was given in high school.

Next, I would like to thank my Carleton professors, in the physics department and beyond, for passing on to me their profound value of teaching and learning in a liberal arts atmosphere. In particular, I owe my entire astronomy career to Cindy Blaha, who took a chance on a precocious freshman and taught me to use an whole observatory and start astronomy research in her spare time, and to Frank McNally, who taught me the tools and methods of modern astronomy research and whose personal mentorship style provides a model for how I want to advise undergraduates in the future. My Carleton experience is a huge part of who I am as a person, and the Carleton physics department is the reason I see myself as a "liberal arts astronomer" and why I chose a career in small college teaching.

I also need to thank UCSC, the astronomy department, and the city of Santa

Cruz for how they both have shaped my grad school experience. First, thank you to UCSC and its students for giving me the opportunities to grow my teaching skills and put them into practice. Thank you to the astronomy department for opening up opportunities to learn about astronomy from professors, speakers, the public, and my peers throughout my six years here. And thank you to Santa Cruz, for being a great place to ride out a pandemic and for teaching me that real societal change happens in local government.

Thank you to my friends Ben, Ibad, Michael, and Shaun, whose interesting conversations, apt political insights, and mind-bending games have given me constant distractions from my life in astronomy, and whose friendships I hope to keep for decades to come.

And of course, thank you to my best friend and fiancée Annie Zanger, who has been the best partner I could have asked for throughout my entire grad school process, whose constant support and companionship has been the most stable and rewarding part of my life, and without whom I may not have made it to the finish line.

I of course need to thank my parents, Chris and Eileen, for all of the support I have received over the course of my entire life. Between buying me a telescope to use as a middle schooler so I could learn about the night sky, coming out at night in the cold to look through my telescope at fuzzy blobs I excitedly found, or driving me to the middle of nowhere in Nevada to stare at the night sky, my parents have always supported me in my passion. And also thank you for supporting me in a much more literal sense throughout my time in Santa Cruz with countless airport runs, overnight stays,

and extended escapes from the pressures of grad school. My life will be substantially changed when I truly move away from my home in northern California for the first time, but I will come back to visit often.

And lastly and most importantly, I of course have to thank the people who have most directly contributed to the existence of this dissertation. First, thank you to my informal co-advisor Kyle Westfall, whose practical and regular help taught me to be a better researcher and coder, and whose regular check-ins always steered me back in the right direction when I was lost. I look forward to continuing to collaborate on our projects that have gone into this dissertation, and to continuing to hear your voice in my ear (whether real or imagined) whenever I write bad code or don't fully understand and characterize my errors. And finally, to my advisor Kevin Bundy, whose support led to this entire dissertation happening. Your scientific work throughout my time in Santa Cruz has fostered my love for galactic astronomy and IFU astronomy, and your flexibility as an advisor allowed me to change my plans to chase whatever paper plan or teaching opportunity I had just come up with. I have always admired your ability to quickly absorb a month's worth of work and immediately ask one simple question to completely turn it upside-down, and I hope that one day I can match your level of deep insight into the core meanings and motivations of research and not get too lost in the details.

Kevin and Kyle (as well as everyone else on this list) took me from a clueless undergraduate who didn't know how grad school worked to a professor-to-be getting ready to take on student researchers of my own, and I can't wait to put all I have learned

into practice next year and beyond.

Scientific Acknowledgements

I would like to acknowledge Andrew Leung and his former advisor Niv Drory, whose Master's thesis work on a Bayesian velocity field fitting code for MaNGA data informed early work on Nirvana. Though Andrew left astronomy years ago and I have not been able to talk to him since early 2019, his work lives on in the completion of the Nirvana catalog. Thank you to Niv for sending along Andrew's code and helping me to adapt it into Nirvana.

I acknowledge use of the lux supercomputer at UC Santa Cruz, funded by NSF MRI grant AST 1828315.

Funding for the Sloan Digital Sky Survey IV has been provided by the Alfred P. Sloan Foundation, the U.S. Department of Energy Office of Science, and the Participating Institutions. SDSS-IV acknowledges support and resources from the Center for High-Performance Computing at the University of Utah. The SDSS web site is www.sdss.org.

SDSS-IV is managed by the Astrophysical Research Consortium for the Participating Institutions of the SDSS Collaboration including the Brazilian Participation Group, the Carnegie Institution for Science, Carnegie Mellon University, the Chilean Participation Group, the French Participation Group, Harvard-Smithsonian Center for Astrophysics, Instituto de Astrofísica de Canarias, The Johns Hopkins University, Kavli Institute for the Physics and Mathematics of the Universe (IPMU) / University of Tokyo, Lawrence Berkeley National Laboratory, Leibniz Institut für Astrophysik

Potsdam (AIP), Max-Planck-Institut für Astronomie (MPIA Heidelberg), Max-Planck-Institut für Astrophysik (MPA Garching), Max-Planck-Institut für Extraterrestrische Physik (MPE), National Astronomical Observatories of China, New Mexico State University, New York University, University of Notre Dame, Observatário Nacional / MCTI, The Ohio State University, Pennsylvania State University, Shanghai Astronomical Observatory, United Kingdom Participation Group, Universidad Nacional Autónoma de México, University of Arizona, University of Colorado Boulder, University of Oxford, University of Portsmouth, University of Utah, University of Virginia, University of Washington, University of Wisconsin, Vanderbilt University, and Yale University.

We also made use of the following software: Astropy (Astropy Collaboration et al. 2013, 2018); Numpy (Harris et al. 2020); emcee (Foreman-Mackey et al. 2013); Colossus (Diemer 2018); Scipy (Virtanen et al. 2020); matplotlib (Hunter 2007); fftw Frigo & Johnson (2005).

Published Material

The text of this dissertation includes reprints of the following published material led by DiGiorgio, with the permission of the listed coauthors.

Chapter 2 was published in the literature as DiGiorgio et al. (2021). I was responsible for the producing the work contained within the text, writing the text, and creating the figures, with Kevin Bundy and Kyle Westfall supervising the work that provides the basis for this dissertation. Alexie Leauthaud provided guidance on weak gravitation lensing, and David Stark provided early help on position angle variations in MaNGA galaxies.

Chapters 3 and 4 are expected to be submitted to *The Astrophysical Journal* in the coming months.

For all of my students, past, present, and future

Chapter 1

Introduction

When Vesto Slipher observed M31 and NGC 4594, better known now as the Andromeda Galaxy and the Sombrero Galaxy, using the spectrograph at Lowell Observatory in 1914 (despite "exasperating circumstances"), he made the unexpected discovery that the absorption lines in the galactic centers were slanted (Slipher 1913, 1914). From these observations, he inferred that the Andromeda spiral nebula was rotating at a velocity of ∼300 km/s, which he noted "is the greatest hitherto observed" and suggests that "the spirals as a class have higher velocities than do the stars."

Of course, it was not until more than a decade later that Hubble (1926) conclusively proved that these spiral nebulae were in fact other galaxies, so Slipher was not aware at the time that he had invented the field of galaxy kinematics (Sofue & Rubin 2001). The study of galaxies and how they rotate has yielded some of the most monumental discoveries in astrophysics in the century since. This dissertation aims to contribute to the century-long study of galaxy kinematics by using the information

contained within the finer details of galaxy rotational data to learn about the galaxy, its history, and the Universe it inhabits, and this introduction seeks to give a background on how galaxy rotation has been studied and understood over time to better motivate these advances.

1.1 The Flattening of Galaxy Rotation Curves

It has been known since the time of Kepler and Newton that rotational velocity correlates directly with the overall mass of a system, and astronomers quickly applied this logic to disk galaxies upon discovering their rotation. It was noticed as early as 1932 that the rotational velocity in the solar neighborhood in the Milky Way did not match up with observed mass concentrations (Oort 1932), and this was confirmed in extragalactic regimes a short time later when Oort (1940) found an "unknown flattening of the attracting mass" in nearby elliptical galaxies.

However, given the difficulty in obtaining reliable rotation curves for large numbers of galaxies at high spatial and spectral resolution, galaxy rotation was probed instead with radio observations. Tully & Fisher (1977) famously used the width of radio emission lines to construct a relation between disk galaxy absolute magnitude and peak-to-peak width, which can be extrapolated to a relationship between mass and maximum rotational velocity. The Tully-Fisher Relation (TFR) was a valuable tool for determining distances to galaxies in the absence of other methods, as well as directly linking a galaxy's mass to its rotational properties.

It was not until the 1970s that large enough samples of kinematic measurements

were assembled to verify these results. By then, enough rotation curves had been obtained to document a consistent rise in the outer rotation curves in late-type spirals (Rubin et al. 1978), and to subsequently proclaim that it was "inescapable that non-luminous matter exists beyond the optical galaxy" (Rubin et al. 1980), which we now know as dark matter. They described the averaged rotation curves of their galaxy sample using the TFR and found good agreement, but did not attempt to describe the kinematics of the disks themselves.

1.2 Modeling Disk Rotation

It took until 1965 before the first two-dimensional representation of a galaxy's rotation was published (an H I map of M31 in Argyle 1965), but the wider availability of these *velocity fields* in the 1970s and 1980s led to a rise in interest in quantitative models of disk rotation. When using long-slit observations, it is simple enough to align the spectroscopic observation with the galaxy's major axis to capture the maximum rotation and avoid trigonometric effects, but with 2D velocity fields, a full circular model is necessary.

The first prominent use of such techniques was in Warner et al. (1973), who assumed the disk component of the galaxy was infinitely thin, and divided the galaxy into a series of annuli and the velocity measurements within each annulus are averaged, using a least-squares optimizer to construct a global model with the best inclination i, position angle, center, and systemic velocity V_{sys}. This thin disk model can be

summarized in the following format:

$$V_{obs} = V_{sys} + V(r) \cos\theta \sin i, \tag{1.1}$$

where the observed velocity V_{obs} is constructed using only the extrapolated velocity values V as a function of the on-sky projected and position angle-adjusted elliptical polar coordinates r and θ. This approach was modified in Begeman (1987, 1989) to allow for independent inclination and position angle values for each of the annular bins, a so-called tilted ring model meant to capture features in velocity fields that changed with radius.

In the 1990s, interest shifted from purely descriptive and non-parametric velocity field models to predictive models based on dynamical theory. Such models often relied on replacing the rotation curve function with a physics-based parametric function in order to describe galaxies as a whole (Glazebrook 2013). One simple example of this approach is the arctangent model from Courteau (1997), which is rooted in dark matter halo profiles:

$$V(R) = \frac{2}{\pi} V_{max} \arctan R. \tag{1.2}$$

A significantly more complex model is the "Universal Rotation Curve" from Persic et al. (1996) based solely on luminosity:

$$V^2 = V_{disk}^2 + V_{halo}^2 \tag{1.3}$$

$$V_{disk}^2 = V^2(R_{opt})\,\beta\,\frac{1.97x^{1.22}}{(x^2+0.78^2)^{1.43}} \tag{1.4}$$

$$V_{halo}^2 = V^2(R_{opt})(1-\beta)(1+\alpha^2)\,\frac{x^2}{x^2+\alpha^2} \tag{1.5}$$

$$x = \frac{R}{R_{opt}} \tag{1.6}$$

$$\alpha = 1.5\left(\frac{L}{L_*}\right)^{1/5} \tag{1.7}$$

$$\beta = 0.72 + 0.44\log\frac{L}{L_*} \tag{1.8}$$

where R_{opt} is the radius encircling 83% of light. Though they differ significantly in complexity, both of these models had success in describing rotation in large and widely-varied samples of galaxies using only a small, successfully reproducing the TFR in the visual regime.

These models give an insight into the dynamic and kinematic properties of the galaxies they describe. For instance, a more rigorous approach based on the dynamics of an exponential disk yields the following rotation curve model from Freeman (1970):

$$V(R) = \left(\frac{2GM}{h}\right)^{1/2} x\left(I_0(x)K_0(x) - I_1(x)K_1(x)\right)^{1/2} \tag{1.9}$$

for disk scale length h and $x = r/2h$. Such a model allows for the direct determination of the total disk mass M and a more direct look into the dark matter content of the galaxy.

1.3 Modeling Nonaxisymmetric Disks

One major sacrifice of the parametric rotation curve models described in the previous section is that they are tailored to fit broad classes of galaxies at the expense of describing the peculiarities within each galaxy where they deviate from the simplified model. For instance, warps are portions of disks that deviate from ideal flat disks in the z direction, spiral arms can cause higher-order disruptions in velocity fields that change with both radius and azimuth, and inflows/outflows create noncircular motions that are not described by the simple structure of Equation 1.1 (Teuben 2002).

Such nonaxisymmetric features (i.e. features that are not symmetrical about the central axis of the disk) can be described by nonparametric models such as the tilted ring model mentioned in the previous section. By allowing each annulus to behave independently and have unique inclinations and position angles, the radial inclination change caused by a warp or the azimuthal variations of spiral arms can be accurately represented. However, on their own, these descriptive, nonparametric models do not provide insight into the dynamical properties of the galaxy without further astrophysical analysis. Other methods such as the Radon transform (Stark et al. 2018) are also able to describe variations in disk parameters as a function of radius, but require further analysis and classification to fully characterize their causes.

A particularly prominent example of an analysis framework that bridges the gap between physics-based simplified parametric models and descriptive nonparametric models is kinemetry (Krajnović et al. 2006a). Extending the principles of Fourier decomposition of nonaxisymmetric features that have been in common use in extended-

source photometry for decades, kinemetry models small-scale perturbations in galactic disks using higher-order spatial modes. As the highest spatial order N goes to infinity, any 2D velocity field can be described to arbitrarily high precision using the rotation curve model

$$V(R) = \sum_{n=1}^{N} V_{n,t}(R)\cos(n(\theta - \phi_n)) + V_{n,r}(R)\sin(n(\theta - \phi_n)), \tag{1.10}$$

for spatial order n and position angle ϕ_n for each order. Kinemetry is able to describe radial motions and off-axis disks present in early-type galaxies, producing detailed models with $N = 5$ (Krajnović et al. 2006a). However, we are again presented with the problem of a model that is descriptive at the expense of physical basis. These descriptive models allow for greater flexibility in physical models later on, but in order to directly extract meaning from these fits, they must be restricted to apply only to perturbations with astrophysical basis.

The velocity field model in Spekkens & Sellwood (2007) works similarly to kinemetry but is restricted to $N < 2$, focusing primarily on bisymmetric distortions caused by bars:

$$V(R) = V_t(R)\cos\theta - V_{2t}(R)\cos\big(2(\theta - \phi_b)\big)\cos\theta - V_{2r}(R)\sin\big(2(\theta - \phi_b)\big)\sin\theta. \tag{1.11}$$

Adding second-order radial and tangential spatial terms V_{2r} and V_{2t} to a thin disk model enables the characterization of radial flows along the bar major axis, a real astrophysical effect, while not sacrificing physical meaningfulness by overfitting a model

with unphysically high-order spatial terms. This model and the accompanying software packages *Velfit* (Spekkens & Sellwood 2007; Sellwood & Sánchez 2010) and later *DiskFit* (Sellwood & Spekkens 2015)) has been successful in reproducing barred velocity fields (e.g. Bisaria et al. 2022; Garma-Oehmichen et al. 2022; Holmes et al. 2015).

Traditional velocity field models can also be modified to suit other specific kinematic features of a galaxy. For instance, kinematic weak lensing (KWL) is the distortion of background galaxy velocity fields in the presence of a foreground gravitational lens. Such distortions would create a nonaxisymmetric distortion in a tilted ring model of the velocity field that could be used to measure lensing shear (Blain 2002). Modification to the rotation curve model is thus necessary to extract this additional information from the galaxy velocity field, otherwise such information will be lost.

This KWL modification can take a number of forms. Morales (2006) quantifies the shear through the measurement of the angle between the kinematic major and minor axes, which is no longer expected to be perpendicular in a sheared coordinate system. Gurri et al. (2020) constructs a parametric velocity field model similar to Equation 1.2 but with an added fit parameter for lensing shear to capture the distortion in lensed velocity fields.

1.4 Outline of This Work

Galaxy rotation can be modeled in such a way that we can learn about the astrophysics of the underlying system, but the modeler must take special care that they do not construct a model that does not accurately account for nonaxisymmetries present

in the velocity field. Doing so would not only mischaracterize the data but also lose out on valuable information contained within those asymmetries.

The structure of this dissertation is as follows: Chapter 2 details a novel kinematic weak lensing velocity field model that combines both kinematic and photometric information to improve the fidelity of lensing shear models. Chapter 3 expands on previous kinematic models of bisymmetric velocity field distortions by creating the largest sample of barred galaxy velocity field fits assembled to date, and Chapter 4 uses these fits to directly tie stellar population gradient flattening to noncircular bar motions on a large scale for the first time. Chapter 5 Summarizes these results and discusses future lines of inquiry.

Chapter 2

A Novel Framework for Modeling Weakly Lensing Shear Using Kinematics and Imaging at Moderate Redshift

2.1 Introduction

Weak gravitational lensing is a powerful and increasingly utilized tool for measuring how mass is distributed throughout the Universe (e.g. Mandelbaum 2018). Applications include use of cosmic shear to probe the mass density and the growth of structure in the Universe (e.g. Troxel et al. 2018; Gatti et al. 2020; Hikage et al. 2019), galaxy-galaxy lensing to characterize halo masses of galaxies in different stellar-mass

regimes and perform 3×2 correlation studies (e.g. Leauthaud et al. 2012; Krause et al. 2017), and cluster lensing profiles to measure cluster-scale halo mass profiles and halo shapes (e.g. Umetsu et al. 2018; Mandelbaum et al. 2006). These science goals have motivated large-scale weak-lensing surveys with new instruments, telescopes, and even satellite missions. Major projects include the Hyper Suprime Cam (HSC, Aihara et al. 2018), the Kilo Degree Survey (KiDS, Kuijken et al. 2015), the Legacy Survey of Space and Time (LSST, Ivezić et al. 2019), *Euclid* (Laureijs et al. 2011), the Nancy Grace Roman Space Telescope (Spergel et al. 2015), and the Dark Energy Survey (DES, Krause et al. 2017; Troxel et al. 2018; Gatti et al. 2020).

Weak-lensing surveys seek to measure distortions in a galaxy's shape caused by lensing shear, a geometric effect caused by the gravitational lensing of a background source by mass in the foreground. To first order, this distortion results in background galaxies becoming elongated in the direction tangential to the surface-density gradient of the foreground mass distribution.

A number of factors complicate lensing measurements in conventional surveys that use imaging to measure galaxy shapes. Weak lensing distortions only induce a $<1\%$ change in observed ellipticity. Measurements at this level of precision are typically achieved by statistically stacking results from multiple sources, but our uncertain knowledge of the intrinsic or "pre-lensed" galaxy ellipticity distribution ("shape noise") typically necessitates thousands of stacked sources to detect a lensing signal. Potential biases become a greater concern with added complications, such as intrinsic alignments of source galaxies with near-foreground dark matter structure (e.g., filaments) and sys-

tematic errors in shape measurements resulting from instrumentation (e.g., Troxel & Ishak 2015; Mandelbaum 2018). Very large samples are therefore required to drive down statistical errors and test for systematics that can otherwise overwhelm the shear signal.

For instance, the CLASH survey (Umetsu et al. 2014) used $\sim 10^4$ background galaxies around each of 20 foreground Abell clusters to recover mass density profiles precise enough to constrain dark matter halo mass profiles. Meanwhile, cosmic shear surveys like the DES (Troxel et al. 2018) use $\sim 10^7$ galaxies to sufficiently characterize their signal, but even these large samples remain susceptible to systematic biases. All of these efforts require deep imaging over wide areas, typically carried out on 2 meter- to 8 meter-class telescopes.g

The burgeoning subfield of kinematic weak lensing (KWL), also referred to as "precision weak lensing" in the literature (Gurri et al. 2020, 2021), provides an additional means of inferring lensing shear by measuring distortions in the projected velocity field of source galaxies. Although KWL requires more expensive spectroscopic observations, many fewer galaxies are needed to detect a signal. This is because the velocity field encodes a trace of the galaxy's original, pre-lensed coordinate space. The induced lensing distortions can be fit directly, eliminating or at least dramatically reducing the shape noise. If future weak-lensing analyses could make use of KWL, they could enable higher spatial resolution maps of foreground mass, more sensitive mass measurements, and independent checks on results from conventional imaging surveys (Huff et al. 2019).

The literature investigating applications of KWL has fallen into two regimes:

high-spatial-resolution kinematic measurements on small samples, and lower-precision kinematic measurements derived from large samples. The idea of KWL was first put forward by Blain (2002), who determined that weak lensing shear would change the symmetry of a galaxy's rotational velocity as measured in an azimuthal ring of constant radius. The idea was further developed by Morales (2006), who proposed measuring the angle between the kinematic major and minor axes, which are no longer perpendicular in a lensed galaxy. A similar idea was developed by de Burgh-Day et al. (2015), who suggested searching for lensing-induced asymmetries in the reflection symmetries of galaxy kinematic data. All these authors emphasize the potential of making a shear measurement with a single galaxy and obtaining a measurement that would be independent of shape noise. However, none of these studies reported a detection due to the small size of lensing effects at nearby redshifts where the high-spatial-resolution spectroscopic measurements required for precise measurements are most readily available.

Huff et al. (2019) instead proposes implementing KWL on a survey scale, considering large samples where individual measurements with less kinematic information are statistically stacked. Building on the work of Huff et al. (2013), they propose targeted measurements of lensing-induced differences in the projected velocity along the major and minor axes. Wittman & Self (2021) performs a Fisher Matrix analysis of this technique in a hypothetical DES-scale survey to derive theoretical limits on the covariances of the derived lensing parameters.

In the first reported detection of kinematic weak lensing, Gurri et al. (2020) stake out a middle ground in sample size versus per-galaxy information content. They

collect and analyze 2D velocity fields of ∼20 galaxies at $z < 0.15$, and report a positive mean shear amplitude detected at 2.5σ. They forward-model each source galaxy with a rotating thin-disk model that allows shear to vary and apply their technique to selected source galaxies likely to be sheared by foreground halos. The detection reported by Gurri et al. (2020) is an exciting development in the young field of KWL, but also highlights upcoming observational challenges. For instance, they find discrepancies between their theoretical and observed shear magnitudes, which they say likely arise from a combination of intrinsic kinematic irregularities in their sample galaxies ("dynamical shape noise") and the scatter in the stellar-halo mass relation (see Gurri et al. 2021). It will be difficult to obtain the kinds of highly-sampled and high-S/N velocity fields in Gurri et al. (2020) for source galaxies at $z \lesssim 1$, but it is at these redshifts where probes of structure formation are most needed and the lensing kernel more favorable (Weinberg et al. 2013).

With this challenge in mind, we build on the techniques of Gurri et al. (2020) by introducing additional constraints from galaxy shape measurements into the KWL formalism using a Bayesian forward model. We show that by including measurements of the major-axis position angle of an ellipse fit to the surface brightness profile and comparing it to the position angle derived for the sheared velocity field, we can improve the per-galaxy shear S/N by several times in many cases. This motivates us to explore the potential use case of measuring the mass and shape of galaxy cluster halos at $z \sim 0.3$ (Bartelmann & Maturi 2017) with IFU observations of 50–100 galaxies at $z \sim 0.7$. Immediately valuable for studies of individual clusters, a future survey program could

aid mass calibrations required for cluster cosmology (e.g. Bocquet et al. 2019) and opens new possibilities for wide-scale KWL surveys at $z \lesssim 1$ with a dedicated survey.

The chapter is structured as follows: Section 2.2 gives background on relevant weak-lensing theory and introduces our formalism for how lensing affects the shape of a galaxy. Section 2.3 studies the impact of lensing shear on the shape of a rotating galaxy and compares the merits of different techniques for measuring kinematic shear observables. Section 2.4 develops our modeling framework for including offsets between the kinematic axes and axes derived from imaging for a given galaxy and characterizes the improvement of the precision of lensing measurements and the important increase of S/N that results. Section 2.5 gives a summary and looks forward to future applications of the technique.

Throughout this chapter, we assume a Planck 2018 cosmology (Planck Collaboration et al. 2018) as implemented in the `Colossus` cosmology package from Diemer (2018), with $H_0 = 67.36$ km s^{-1} Mpc^{-1} and $\Omega_m = 0.3111$ at $z = 0$.

2.2 Weak Lensing Effects on Imaging

To understand the benefits image position angle measurements can have for KWL, we first review key aspects of how lensing geometry changes the shape of galaxies. Imaging-based lensing surveys typically model background galaxies as ellipses with a measured on-sky position angle and ellipticity that are used to derive lensing amplitude. This serves both as context for the current state of the field and as a basis for the techniques developed in Section 2.4. For a more detailed treatment of the subject, see

Bartelmann & Maturi (2017).

2.2.1 General Lensing Theory

Gravitational lensing is a well-established result of general relativity and its effects have been well-characterized (Miralda-Escude 1991). Because photons travel along geodesics, when they pass through regions of spacetime that have been distorted by a mass distribution, the geodesic is deflected, curving their paths. So the observed image of a background galaxy will be distorted by any foreground mass along the line of sight.

If we assume that the characteristic scale of the foreground mass distribution is small compared to the other relevant distance scales in the system — the angular diameter distance from the observer to the foreground mass, D_L, the distance from the observer to the background source, D_S, and the distance from the foreground mass to the background source, D_{LS} — we may adequately describe the system using the thin lens approximation. This stipulates that the deflection of the photons in the system happens in an infinitely thin plane located at the lens position and that the photon travels in a straight line everywhere else. The magnitude of the angular deflection relates to the projected surface density Σ of the 3D foreground mass distribution ρ, where

$$\Sigma(\boldsymbol{\xi}) = \int \rho(\boldsymbol{\xi}, \boldsymbol{z}) d\boldsymbol{z}, \tag{2.1}$$

for $\boldsymbol{\xi} = \sqrt{\boldsymbol{x}^2 + \boldsymbol{y}^2}$ with $\boldsymbol{x}$ and $\boldsymbol{y}$ being the physical coordinates of the mass distribution

on-sky and $\boldsymbol{z}$ being the line of sight vector from the observer. The angular deflection of a photon is given by

$$\boldsymbol{\alpha}(\boldsymbol{\xi}) = \frac{4G}{c^2} \int \Sigma(\boldsymbol{\xi'}) \frac{\boldsymbol{\xi} - \boldsymbol{\xi'}}{|\boldsymbol{\xi} - \boldsymbol{\xi'}|^2} \, d^2\boldsymbol{\xi'}. \tag{2.2}$$

The deflection angle can also be given in terms of the lensing potential ψ as

$$\boldsymbol{\alpha}(\theta) = \frac{D_S}{D_{LS}} \nabla_\theta \psi, \tag{2.3}$$

where θ is the angular separation of the source as seen from the perspective of the observer: $\theta = |\boldsymbol{\xi}|/D_L$. For a point mass lens in the weak lensing regime, ψ can be written as

$$\psi = \frac{4GM}{c^2} \frac{D_{LS}}{D_L D_S} \ln |\boldsymbol{\xi}|. \tag{2.4}$$

The magnitude of the lensing effect is often expressed in terms of the critical surface mass density, which defines the characteristic angular scale of a lensing system:

$$\Sigma_{\text{crit}} = \frac{c}{4\pi G} \frac{D_S}{D_L D_{LS}}. \tag{2.5}$$

The distortion manifests itself in two ways. The first is the convergence κ, which has magnitude $\kappa = \Sigma/\Sigma_{\text{crit}}$ and magnifies the background source. However, for the purposes of this chapter, we will be more interested in the lensing shear.

The shear, as its name implies, distorts the coordinate system of the source, changing its observed shape. This distortion can be broken into two separate compo-

nents defined by their relation to the derivatives of the lensing potential:

$$\gamma_+ = \frac{1}{2}\left(\frac{\partial^2\psi}{\partial\theta_x^2} - \frac{\partial^2\psi}{\partial\theta_y^2}\right), \quad \gamma_\times = \frac{\partial^2\psi}{\partial\theta_x\partial\theta_y}. \tag{2.6}$$

where θ_x and θ_y are perpendicular angular coordinates in the arbitrarily defined coordinate system projected onto the lens plane. Following the formalism of Huff et al. (2013), the shear aligned with the coordinate axes is called γ_+, while the cross term $\gamma_\times$ is aligned with the diagonals of the coordinate system. For a simplified case of an axisymmetric lens, the shear magnitude is given by

$$|\gamma| = \frac{\Delta\Sigma}{\Sigma_{\rm crit}}, \tag{2.7}$$

where $\Delta\Sigma$ is the differential projected surface mass density, the difference between the value of Σ at a given radius r_0 and the mean Σ within that radius:

$$\Delta\Sigma = \bar{\Sigma}(r < r_0) - \Sigma(r_0). \tag{2.8}$$

In the simplified axisymmetric case, the two shear components can also be expressed as

$$\gamma_+ = |\gamma|\cos 2\theta \quad \gamma_\times = |\gamma|\sin 2\theta, \tag{2.9}$$

with $\theta = \tan^{-1}(\theta_y/\theta_x)$. Positive and negative values for the shear result in distortions in opposite directions. We assume $|\gamma| < 0.1$ in this chapter to remain in the weak-lensing regime where the magnitude of the distortions are small and the small angle approximation is still valid.

2.2.2 Image Distortions

In the weak-lensing regime, the recognizable features of strong lensing, like arcs and multiple images, give way to tiny distortions in background sources that are usually only detectable through statistical methods applied to large samples. Weak lensing effects are well-parameterized by a single transformation matrix that can be applied to the coordinate system of the background source:

$$A = \begin{pmatrix} 1 - \kappa + \gamma_+ & \gamma_\times \\ \gamma_\times & 1 - \kappa - \gamma_+ \end{pmatrix} \tag{2.10}$$

If we do not care about the size and luminosity of the source, we may disregard the convergence κ since it is small in the weak-lensing regime, so we may simplify A to be:

$$A \approx \begin{pmatrix} 1 + \gamma_+ & \gamma_\times \\ \gamma_\times & 1 - \gamma_+ \end{pmatrix}. \tag{2.11}$$

The effect of γ_+ is to symmetrically elongate the source along the tangential axis[1], meaning the on-sky orientation of the source is not substantially affected. However, $\gamma_\times$ shears the source, causing an effective rotation.

We can apply this transformation to a toy model of a galaxy, a typical background source in a weak-lensing survey. We may model the galaxy as a circle inclined at some angle relative to the observer, so it is seen simply as a series of concentric elliptical isophotes, each satisfying

[1]Note that this is distinct from κ, which elongates the galaxy in all directions equally, causing a perceived magnification.

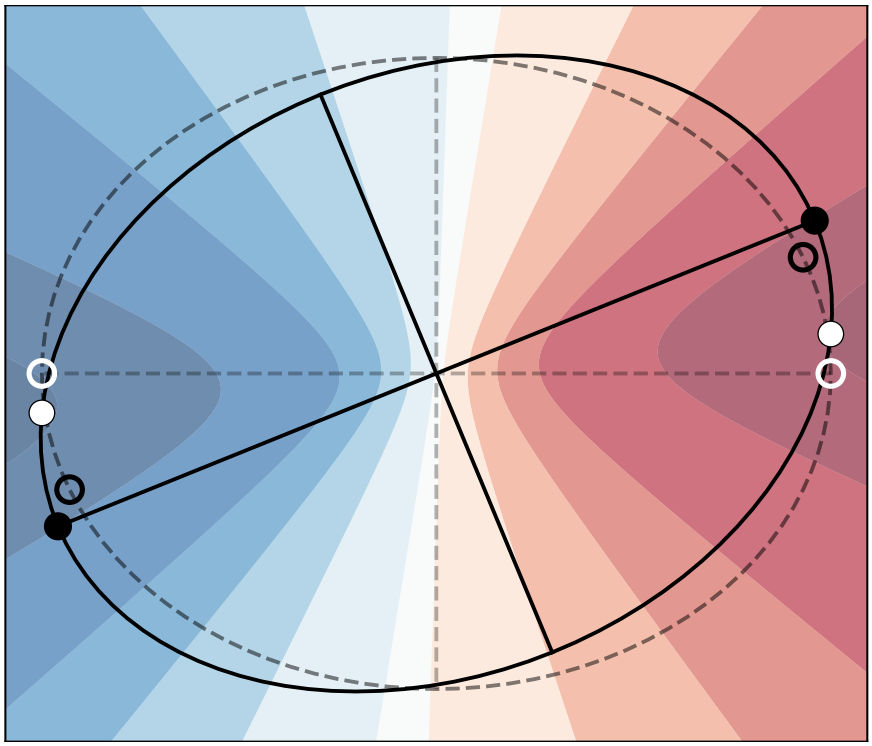

Figure 2.1: Representation of how shear from gravitational lensing affects the positions of major and minor axes derived from kinematics and imaging/photometry. The original orientation of the galaxy is shown as a dashed elliptical isophote, with the dashed lines marking the positions of the unlensed major and minor axes (photometric and kinematic are the same). A lens to the upper left of the galaxy applies a shear, distorting the galaxy's intrinsic coordinate system and velocity field contours according to the transformation matrix A (Equation 2.11). The solid ellipse represents how a new elliptical isophote would be fit to the sheared galaxy, along with its new imaged major and minor axes. The colored contours represent the observed velocity field, with red and blue indicating receding and approaching sides of the galaxy, respectively, and darker colors indicating higher velocity magnitude. The point along the lensed isophote that is measured as the lensed imaged major axis (filled black circle) was not on the major axis of the unlensed galaxy (unfilled black circle), leading to a discrepancy between the lensed axis observed in imaging and the kinematic axis (filled white circle). A similar effect happens with the minor axis. The galaxy shown has an axis ratio $q = 0.8$ and the shear applied is $\gamma_\times = 0.1$.

$$1 = q^2 x^2 + y^2, \tag{2.12}$$

where q is the axis ratio of the projected ellipse. Applying the shear transformation matrix to this object, we find that, post-lensing, the coordinate system has become $\boldsymbol{x}' = A^{-1}\boldsymbol{x}$ for $\boldsymbol{x} = (x, y)^T$, so

$$1 \approx q^2 x'^2(1 - 2\gamma_+) + y'^2(1 + 2\gamma_\times) - 2x'y'\gamma_\times(1 + q^2), \tag{2.13}$$

where we have dropped higher order terms in γ_+ and $\gamma_\times$ since we expect the magnitude of these terms to be small in the weak lensing regime.

We then treat the deformation of the elliptical isophote as a rotation rather than a shear. The general equation of an ellipse rotated by angle α relative to the origin is

$$1 = \left(\frac{\cos^2\alpha}{a^2} + \frac{\sin^2\alpha}{b^2}\right)x^2 + \left(\frac{\sin^2\alpha}{a^2} + \frac{\cos^2\alpha}{b^2}\right)y^2 - 2\cos\alpha\sin\alpha\left(\frac{1}{b^2} - \frac{1}{a^2}\right), \tag{2.14}$$

where a and b are the lengths of the major and minor axes, respectively. We may greatly simplify this equation if we restrict ourselves to the weak-lensing regime. By assuming α to be small, we can apply the small angle approximation and ignore higher order terms in α. If we then multiply through by b^2 to put everything in terms of the axis ratio $q = b/a$ and set $b = 1$ in arbitrary units, we have

$$1 \approx q^2x^2 + y^2 - 2\alpha xy\left(1 - q^2\right). \tag{2.15}$$

Equations 2.13 and 2.15 are identical except for the cross term. If we assume that the shear can indeed be thought of as a rotation, we can set these two equations equal to each other to find

$$\alpha(1 - q^2) \approx \gamma_\times(1 + q^2) \quad \Rightarrow \quad \alpha \approx \gamma_\times \frac{1 + q^2}{1 - q^2}. \tag{2.16}$$

So the effect of the shear on an isophote can be well-approximated in the weak-lensing regime as a rotation, as seen in Figure 2.1. The rotation angle is determined by $\gamma_\times$, which depends on the magnitude of the overall shear, the relative positions of the foreground lens and the background source, and the axis ratio of the background source, which are in turn determined by Equation 2.9 and the inclination of the galaxy. The magnitude of α is maximized when the background source has a low inclination, has a position angle that is misaligned with the radial vector by 45°, and when the foreground lens is more massive.

The axis ratio q changes as a result of lensing as well, as seen by the effect of the transformation matrix A on a point at (a, b):

$$\begin{pmatrix} 1+\gamma_+ & \gamma_\times \\ \gamma_\times & 1-\gamma_+ \end{pmatrix} \begin{pmatrix} a \\ b \end{pmatrix}$$

$$= \begin{pmatrix} (1+\gamma_\times+\gamma_+)\,a \\ (1+\gamma_\times-\gamma_+)\,b \end{pmatrix} = \begin{pmatrix} a' \\ b' \end{pmatrix}, \quad (2.17)$$

where we have defined (a', b') as the major and minor axis lengths of the lensed galaxy. Thus, the lensed axis ratio q' is

$$q' = \frac{b'}{a'} = \frac{(1+\gamma_\times-\gamma_+)}{(1+\gamma_\times+\gamma_+)}\frac{b}{a} \approx \left(1 - \frac{2\gamma_+}{1+\gamma_\times}\right) q, \quad (2.18)$$

where we have again exploited a Taylor series expansion to make a first order approximation. What observers see is the post-lensing axis ratio q' rather than q, so we again approximate to write this as

$$q \approx \frac{q'}{1-2\gamma_+}. \quad (2.19)$$

We see that for small γ_+, $q \approx q'$, and because we will be concerned mostly with cases where this is true, we will ignore the distinction between pre- and post-lensing axis ratios for the remainder of the chapter.

However, neither the angular distortion nor the axis ratio distortion can be directly measured in images of any single galaxy because nothing is known about its original shape. Before the galaxy is lensed, it has some intrinsic position angle and ellip-

ticity that provide the baseline for any lensing distortions. With conventional imaging surveys, the only way we can perceive changes is by looking at the statistical properties of the sample in aggregate. A large sample of galaxies under the same shear will show a net alignment perpendicular to the induced shear that deviates from a random distribution of position angles. Measuring this net alignment is a primary goal of imaging-based weak lensing surveys.

2.3 Weak Lensing Effects on Kinematics

While it is impossible to tell the difference between an elliptical isophote that has been rotated and elongated due to lensing shear and one that was never sheared, the same is not true for projected kinematics of a rotating disk. By taking spectroscopic measurements across the face of a rotating galaxy, the relative velocity of different parts of the galaxy can be determined from the Doppler shift of spectral features compared to the systemic velocity of the galaxy.[2] The kinematic measurements that make up the velocity field are associated with specific coordinates in the galaxy's intrinsic plane, a relationship that is not broken by gravitational lensing. This probe of the galaxy's intrinsic geometry enables much more precise per-galaxy lensing measurements.

In what follows, our analysis is motivated by reducing the final statistical errors on a galaxy's shear measurement, as limited by the quality of the data. We do not treat here the per-galaxy error that stems from intrinsic irregularities in the physical structure of the galaxy. Features that deviate from the model used in the fit will bias the results

[2]In this chapter, we assume an infinitely thin, rotating disk. This assumption may cause problems with highly inclined disks.

regardless of the quality of the data. However, this dynamical shape noise (Gurri et al. 2020) is expected to be randomly distributed across a sample and should beat down as the sample size increases. We will return to the role of statistical and systematic errors in Section 2.4.2.

2.3.1 Kinematic Axis Distortion

Unlike the photometric measurements made by fitting isophotes, the transformation of a galaxy's velocity field cannot be modeled simply as a rotation of the projected field. In order to illustrate the effect of shear on the velocity field, we examine the behavior of two reference locations: a point on the major axis and one on the minor axis.

A point on the major axis of the unlensed galaxy (unfilled white circle on Figure 2.1) can be described by the coordinates $(x, 0)$ for a rectilinear coordinate system aligned with the major and minor axes. We define the on-sky angle of the major axis in a particular reference frame to be the kinematic position angle (PA). Applying the transformation matrix A to this coordinate location, we find that this point gets moved to $((1+\gamma_+)\,x,\ \gamma_\times x)$ (filled white circle), so the angular displacement of the lensed major axis from the original major axis is

$$\theta_{maj} = \tan^{-1}\left(\frac{\gamma_\times}{1+\gamma_+}\right) \approx \frac{\gamma_\times}{1+\gamma_+}, \tag{2.20}$$

where we have performed a Taylor series expansion of the inverse tangent and taken just the first order since we expect the shear to be small in the weak-lensing regime.

We can do a similar transformation to a point on the unlensed minor axis $(0, y)$ to find

$$\theta_{min} = \tan^{-1}\left(\frac{1-\gamma_+}{\gamma_\times}\right) \approx \frac{\pi}{2} - \frac{\gamma_\times}{1-\gamma_+}, \tag{2.21}$$

where we have again performed a first-order Taylor series expansion.

We can again exploit Taylor series to expand Equations 2.20 and 2.21 with respect to γ_+:

$$\theta_{maj} \approx \gamma_\times(1-\gamma_+); \qquad \theta_{min} \approx \frac{\pi}{2} - \gamma_\times(1+\gamma_+). \tag{2.22}$$

The dependence of the angular differences on γ_+ is on the order of $|\gamma|^2$ (assuming that $\gamma_+ \approx \gamma_\times$, which is true for most galaxy-lens orientations). This means that we can neglect the γ_+ term[3] and just write

$$\theta_{maj} \approx \gamma_\times; \qquad \theta_{min} \approx \frac{\pi}{2} - \gamma_\times. \tag{2.23}$$

These simple relations allow us to estimate the shear by measuring how much the axes differ from being orthogonal, as was proposed by Morales (2006). In an ideal velocity field, the angle between the major and minor kinematic axes should be

$$\theta_\perp \approx \frac{\pi}{2} \pm 2\gamma_\times. \tag{2.24}$$

[3]The same is true for the κ term that we have already neglected. If we had kept it, it would have shown up in the denominator here as well and could be neglected with the same logic.

If we could determine the position angles of the velocity maximum, minimum, and zeros and see how they differ from perpendicularity using a technique like the Radon transform (Stark et al. 2018) or kinemetry (Krajnović et al. 2006b), we could use the above result to gain an estimate of the induced shear.

2.3.2 Sheared Velocity Field Fitting

We can produce a more complete picture of the shear of a velocity field if we model the distortion of the entire galaxy rather than just its major and minor axes. We construct a Bayesian forward model that allows us to utilize all of the velocity measurements to obtain a best-fit sheared velocity field.

For the purpose of comparing different KWL techniques in our regime of interest, we create a simulated observation of a galaxy. We consider a source galaxy at $z = 0.7$ behind a $7 \times 10^{14}\ M_{\odot}$ foreground cluster (approximately equal in mass to the Coma cluster, Gavazzi et al. 2009) at $z \sim 0.3$. We assume the mass profile of the cluster follows a Navarro-Frenk-White profile (NFW, Navarro et al. 1997). Two-dimensional emission-line kinematics are feasible at this redshift with 8m-class ground-based optical telescopes (e.g., Contini et al. 2016). We assume an impact parameter of 0.3 Mpc in the plane of the lens corresponding to a 1 arcminute separation from the cluster center, which is the field of view in the MUSE wide-field configuration (Bacon et al. 2010). This system yields a shear magnitude of $|\gamma| = 0.0589$. We assume that the kinematic major axis of the background galaxy is at a 45° angle to the radial vector to the lens, meaning $\gamma_{\times} = 0.0589$ and $\gamma_{+} = 0$. With this shear magnitude in mind, we explore what types of measurements are possible.

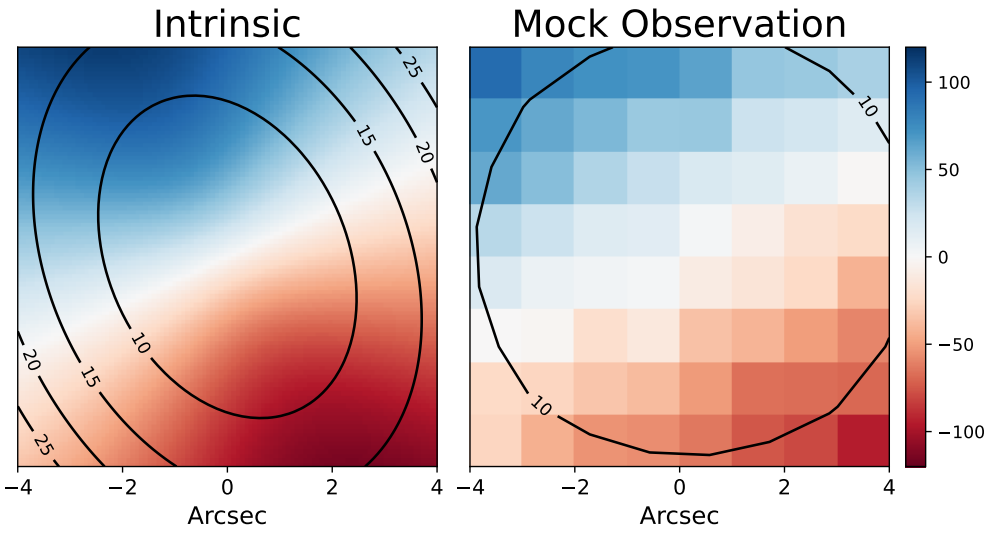

Figure 2.2: Left: A mock intrinsic velocity field to test our KWL shear extraction. This galaxy was generated using the model in Equation 2.25 with parameters $v_{max} = 220$ km/s , $i = 45°$, $\phi = 2$ rad, $h = 2$ kpc, and $v_{sys} = 0$ km/s. A shear of $\gamma_\times = 0.0589$ has been applied to it. The overlaid contours show the error on the velocity measurements in km/s, which are normalized to a central value of 5 km/s. The inverse variance on the velocity measurements is assumed to be proportional to surface brightness, which is modeled as a Sérsic profile of the same galaxy with $n = 1$ and $R_e = 2$ kpc. The velocity inverse variance has been normalized to 0.05 $(\text{km/s})^{-2}$, typical of a MaNGA galaxy. Right: The velocity field from the left panel but smeared and sampled coarsely to emulate an observation at $z \sim 0.7$ with a FWHM of 0.7" on a MUSE-like instrument. See details in Section 2.3.2.

We assume that the inverse variances on the velocity measurements are proportional to surface brightness, which we set as an $n = 1$ Sérsic profile. The scale, inclination, and position angle of the Sérsic profile are defined by the same parameters that define the mock velocity field. normalized to a peak value of 0.05 $(\mathrm{km/s})^{-2}$, corresponding to a velocity error of about 4.5 km/s at the center of the galaxy. This value was chosen because it was the most common value for galaxies in MaNGA (Bundy et al. 2015) and should capture some of the errors from approximating rotation as a thin disk as well.

For the velocity field, we first generate an idealized toy model of a rotating galaxy using a simple model:

$$v(r, \theta) = \frac{2}{\pi} v_{max} \arctan\left(\frac{r}{h}\right) \sin i \, \cos(\theta - \phi) + v_{sys}. \tag{2.25}$$

Here r and θ are polar coordinates of the spectroscopic measurements, v_{max} is the asymptotic rotation speed, h is the characteristic scale radius, i is the inclination, ϕ is the kinematic PA, and v_{sys} is the systemic velocity of the galaxy. The positions of the primary kinematic axes, the part of the velocity field model that the shear measurement primarily relies on, are not sensitive to the specific shape of the rotation curve model. We compared results from this model with the more complex empirically-derived Universal Rotation Curve from Persic et al. (1996) and found negligible difference for the results of this work, as did Wittman & Self (2021) in their analysis. We then apply the transformation matrix (Equation 2.11) to the data to shear the velocity field, an effect more easily seen in Figure 2.1. For the remainder of this chapter, we will use

this model to both simulate mock velocity fields and to fit our mock data, allowing the model complete freedom to describe the mock galaxy.

To simulate a real ground-based observation, we first convolve the velocity field with a Moffat point-spread function (PSF) with a full-width half maximum (FWHM) of 0.7" and $\beta = 2.9$ to the velocity field and inverse variance to model atmospheric distortions, a very good night at a mountaintop observatory. We weigh the PSF convolution using the observed surface brightness profile of the galaxy. We then assume a spatial sampling of 0.2×0.2 arcsec^2, the same as the wide field mode for MUSE, corresponding to $\sim$1 kpc spatial resolution at redshift $z = 0.7$. We generate a velocity field with a characteristic scale radius $h = 2$ kpc and apply a shear of $\gamma_\times \approx 0.06$ to its spatial coordinates. We assume measurements extending out to $\sim 2R_e$ for an $n = 1$ Sérsic profile also with $R_e = 2$ kpc[4], meaning we should have a grid of 8×8 spatial samples across the field of the galaxy. We also apply this same PSF convolution step when fitting this model to data in order to more accurately recover the input parameters.

We also apply random Gaussian errors in the measured velocity according to the assumed inverse variance profile, perturbing the results from the ideal velocity field. The resulting measurements, shown in Figure 2.2, qualitatively resemble actual data taken by MUSE (see Contini et al. 2016, Fig. 5). Because we generate our mock data from ideal rotation curve models, we do not expect per-galaxy systematic errors from dynamical shape noise to be present, leaving only statistical errors. We do not apply this step when fitting the model to the data, instead using the ideal unperturbed model.

[4]For all other mock galaxies generated in this chapter, we will always make the simplification that the characteristic scale radius of the velocity field h and the effective radius of its surface brightness profile R_e are equal.

To find the best velocity field parameters for each mock galaxy, we use the Markov Chain Monte Carlo (MCMC) package `emcee` (Foreman-Mackey et al. 2013), feeding in the velocity measurements across the face of a galaxy. We use the same rotation curve model as was used to generate the velocity field, but we add shear by simply applying the inverse of the transformation matrix given in Equation 2.11 to the underlying coordinates of the measurements and letting $\gamma_\times$ be a free parameter in the fit. Because our velocity field model is sheared directly by the transformation matrix, it is not affected by the approximations we made in Section 2.3.1. This, however, comes at the price of analytic simplicity of the model.

We apply uniform priors to inclination and position angle to allow for random variation in orientation. We use a Gaussian prior on asymptotic velocity with mean 200 km/s and standard deviation 100 km/s and is truncated at 0, parameters that are loosely based off of the MaNGA sample (Bundy et al. 2015). We allow the rotation scale to vary uniformly up to 4 arcseconds. For $\gamma_\times$, we apply a uniform prior bounded at ± 0.5 to allow for a reasonable amount of variation, but not so much as to allow the model to fit any irregularities it sees in the data with unphysical amounts of shear. We use a standard Gaussian likelihood function for comparing the model to the mock data at each iteration. This model produces shear magnitudes and statistical errors that are similar to those measured by Gurri et al. (2020) when applied to the same data.

With these assumptions, we apply our Bayesian velocity-field model to the simulated data and recover the posteriors shown in black in Figure 2.3. We can see that the posteriors include the true values for most of the model parameters, although only

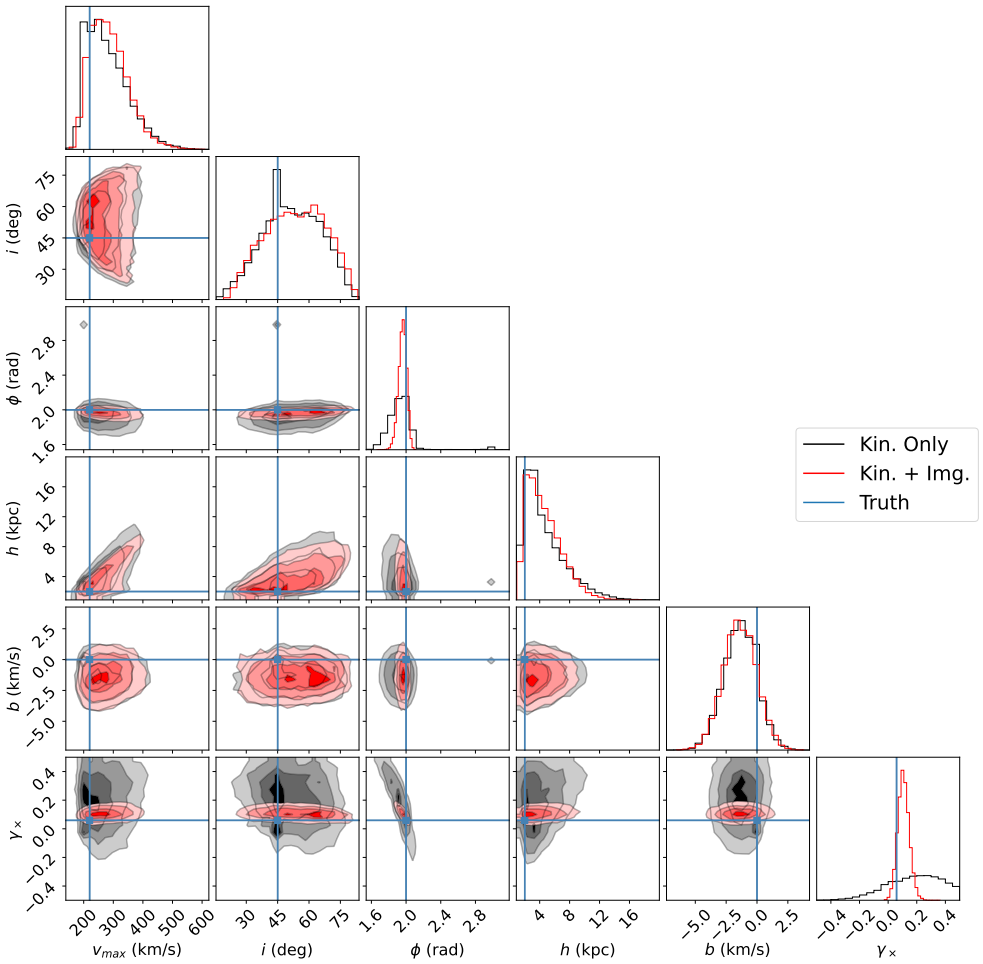

Figure 2.3: Black: The resulting posteriors from applying the Bayesian velocity field model from Equation 2.25 with a free shear parameter to the simulated sheared galaxy described in Section 2.3.2. Most posteriors are centered near their true values (shown as blue lines), but the uncertainty is inflated by injected Gaussian errors, blurring from the PSF, and low spatial resolution. This is especially apparent in inclination and shear. Since the magnitude of the introduced errors greatly outweighs the signal from weak lensing, the posterior for $\gamma_\times$ has very poor precision and the statistical error dominates the measurement. Red: The performance of the model is greatly improved when image PA is included as described in Section 2.4. With a 3 degree error on the image PA, the posteriors are noticeably more constrained than the kinematics-only model, especially the shear, which has a factor of 5 reduction in spread, and the position angle ϕ. The degeneracy between ϕ and $\gamma_\times$ is also resolved.

some appear near the median of the posterior distributions. Two primary factors in the model precision are the effects of the PSF and the added Gaussian noise. Inclination relies on the specific shapes of isovelocity contours, but much of their variation with inclination is masked by the PSF. In addition, the width of the shear posterior σ_γ is hampered by the relatively shallow velocity gradient, limited spatial resolution, and a significant degeneracy with the kinematic position angle. So while we can use this method to extract some of the parameters of the velocity field, we cannot fit our key parameter of interest with much precision. More information on the shear is needed if we want to lower statistical errors enough to produce a successful fit for data of this spatial resolution.

2.4 Combining Imaging and Kinematics

2.4.1 Kinematic and Photometric Position Angle Offset

To better constrain the lensing distortion of the velocity field, we incorporate the image distortion we explored in Section 2.2.2. Comparing the kinematic axis differences derived in Equations 2.22 and 2.23 to the photometric angular difference from Equation 2.16, we can see (as in Figure 2.1) that there is a difference between the angle measured by fitting an isophote and the angle from the velocity field for the major and minor axes:

$$\Delta\theta_{maj} = \gamma_\times \frac{1+q^2}{1-q^2} - \gamma_\times = \gamma_\times \left(\frac{1+q^2}{1-q^2} - 1 \right) = \frac{2\gamma_\times q^2}{1-q^2} \tag{2.26}$$

$$\Delta\theta_{min} = \left(\gamma_\times \frac{1+q^2}{1-q^2} + \frac{\pi}{2}\right) - \left(\frac{\pi}{2} - \gamma_\times\right) = \gamma_\times \left(\frac{1+q^2}{1-q^2} + 1\right) = \frac{2\gamma_\times}{1-q^2}. \tag{2.27}$$

The minor axis deviates more because the velocity field shearing effect goes in the opposite direction of the apparent rotation of the image. A comparison of the dependencies of $\Delta\theta$ on $\gamma_\times$ and q for the major and minor axes is seen in Figure 2.4. More face-on galaxies have larger apparent rotation angles because their shape is easy to distort. A slight elongation of an elliptical isophote in a given direction will have much more effect on the orientation of the isophote if it starts off as relatively round rather than relatively extended.

We can also see that these angular differences mainly depend on $\gamma_\times$ and q. We can then solve for the shear $\gamma_\times$ in terms of the two observables: $\Delta\theta$ (the difference between measured kinematic axis and imaged axis) and the axis ratio q. The relationship between $\gamma_\times$ and the deflection of the major and minor axis position angles differ by a factor of q^2:

$$\gamma_{\times,maj} \approx \frac{\Delta\theta_{maj}(1-q^2)}{2q^2} \tag{2.28}$$

$$\gamma_{\times,min} \approx \frac{\Delta\theta_{min}(1-q^2)}{2}. \tag{2.29}$$

The dependencies we recover here agree well with Wittman & Self (2021) and we will use them in the next section to derive an improved lensing inference based on a combination

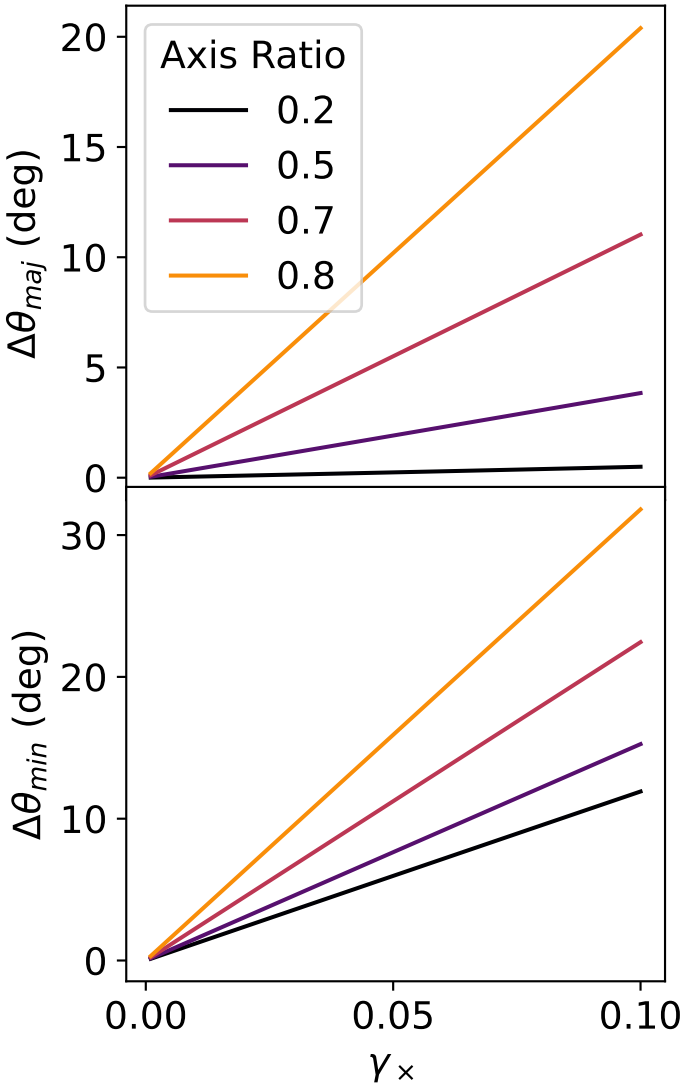

Figure 2.4: The angular difference between the imaged and kinematic axis for the major axis (top) and minor axis (bottom) as a function of the shear $\gamma_\times$ and the axis ratio $q = b/a$. The magnitude of the rotation of the photometric axis increases more quickly for more face-on galaxies because less elongated ellipses are more easily distorted in an arbitrary direction than more elongated ellipses. The major axis shows slightly less angular difference than the minor axis because the imaged and kinematic axes are being shifted in the same direction, while for the minor axis, they are shifted in opposite directions. This is also why the edge-on $q = 0.2$ line for the minor axis still shows some difference.

of imaging and kinematic measurements. By combining the imaging measurements of position angle and axis ratio with velocity measurements of the *kinematic* position angle, we can gain access to a constraint on the gravitational shear induced on the galaxy.

2.4.2 KWL Models with Imaging Information

We rerun the previously described Bayesian velocity field fitting models but with added constraints on the difference between the kinematic and image PAs. We feed the model a mock image position angle, setting the value by perturbing the expected value derived using Equation 2.26 with a Gaussian error based on the assumed level of photometric uncertainty. Commonly-used photometric codes like GALFIT (Peng et al. 2002) often drastically under-report the magnitude of their PA errors. Accurate error accounting must be done by comparing intrinsic PAs in simulated galaxies with the values recovered by photometric fitting. Häussler et al. (2007) suggests that photometric PA measurements have average errors between 1 and 6 degrees depending on image depth, so we will largely restrict our analyses to that range.

We then allow the model to fit the angular difference between the kinematic PA and the perturbed image PA with its shear parameter, incorporating the result as a new Gaussian term in the likelihood function. With this added information, we see a significant reduction in the width of the posteriors σ_γ, as shown by the red posteriors in Figure 2.3. Adding in the image PA allows for the degeneracy between the kinematic PA and the shear strength to be broken much more effectively, resulting in a factor of 5 reduction in σ_γ for an image PA with an error of 3 degrees. This vast reduction in statistical errors has large implications for regimes where the measurement error would

be dominated by statistical error.

These improvements persist even for larger PA errors, as shown in Figure 2.5. Within the range of expected image PA errors (shown as the shaded blue region), we see a reduction in σ_γ by a factor of 2–6, meaning that a KWL technique utilizing imaging shape information is more sensitive. We also see that for large image PA errors, σ_γ approaches its value from before imaging information was added. As expected, as uncertainty in the image PA measurement increases, the statistical error in the measured shear tends towards what is obtained in a fit without image PA constraints.

In Figure 2.6, we explore differing combinations of image PA error and velocity error for a relatively face-on source galaxy (30 degree inclination). Larger errors in image PA or velocity measurement may come from shallower exposures, poor seeing or angular resolution, or irregularities in the galaxy. At this low inclination, improvements in image PA precision improve the KWL shear measurements as much or more than improvements to the velocity precision, reducing the need for higher S/N or higher resolution spectroscopy. Even with moderate image PA uncertainties on the order of several degrees, the precision of KWL measurements can reach levels comparable to those of velocity-field-only fits relying on kinematic measurements at a fraction of the velocity error.

These gains are much larger for lower-inclination galaxies since their imaged axes are much more distorted, allowing them to contribute more to the shear measurement. Higher-inclination galaxies, as shown in Figure 2.7, gain less from their photometric information because the magnitude of the angular deflection is greatly reduced,

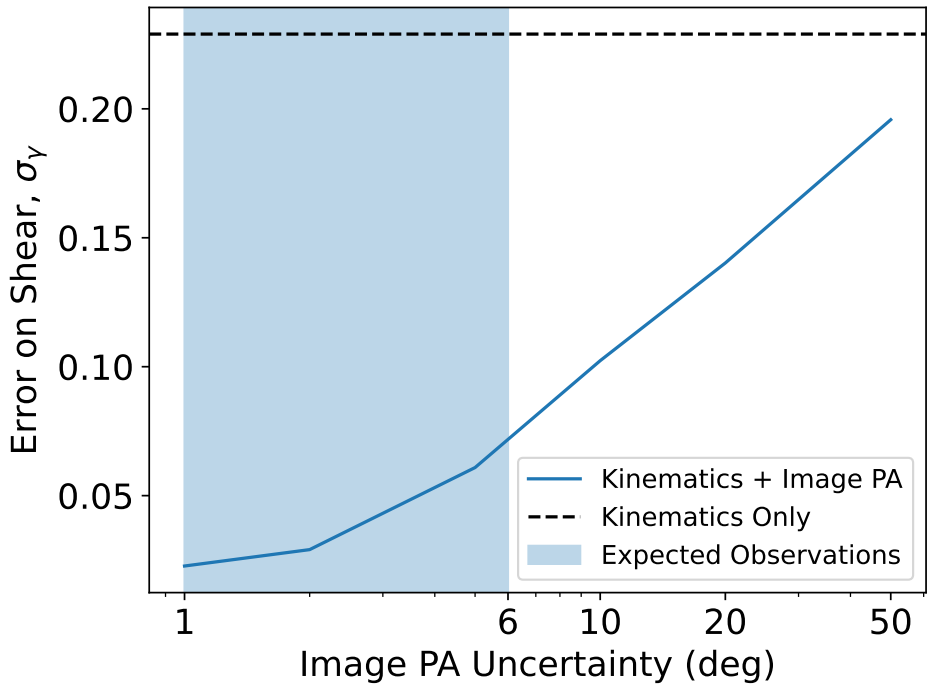

Figure 2.5: The gains in precision seen after adding information on image position angle to our Bayesian KWL model for a mock galaxy like the one in Figure 2.2, including the applied shear of $\gamma_\times \approx 0.06$. The model that fits both the kinematic and imaging distortion (blue line) has an error on the shear posterior σ_γ that is 3-6 times smaller than the model with only kinematics (dashed line) was able to achieve within the region of expected errors on image PA in real data (blue shaded area). If borne out in real observations, this could lead to significant decreases in necessary sample sizes and exposure times to obtain a given lensing S/N. For very large errors in image PA, σ_γ tends back towards the value obtained with no imaging information.

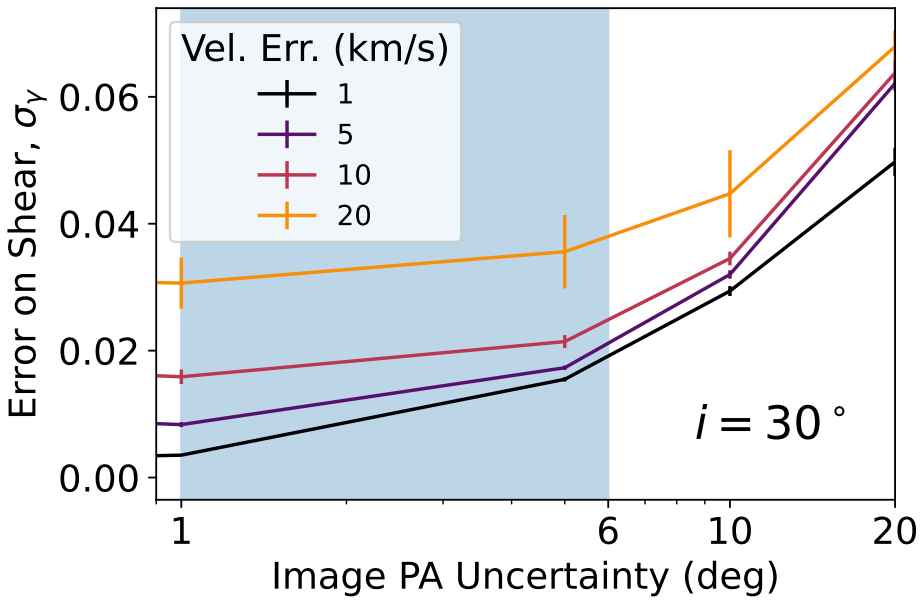

Figure 2.6: The change in the error on the shear measurement σ_γ for a mock velocity field with simulated seeing with different amounts of error on the image PA and different central velocity errors. The input shear is $\gamma_\times \approx 0.06$ and the model velocity field is identical to those used in previous figures except that it has a 30° inclination with respect to the observer. The blue shaded region represents the expected range for image PA errors in real observations. Smaller errors on the image PA lead to higher precision in shear, as is expected. For larger image PA errors, the precision approaches the value derived from just the velocity field, but the value it levels off at depends on the errors in the velocity field itself and the inclination of the galaxy. For image PA errors expected in real data, even poor-quality velocity fields can match the precision reached by very good velocity field-only KWL measurements, presenting opportunities for exposure time savings.

forcing the shear measurement to rely more on kinematic distortion. The distribution of inclinations within a population of randomly-oriented disks is uniform over $\sin i$ (Law et al. 2009), so the inclination distribution of a random sample from a survey will be weighted towards the high end, with a mean inclination angle of 1 radian (about 57°) or a mean axis ratio of $q \approx 0.54$. So unless a survey sample is deliberately designed to sample low-inclination galaxies, most galaxies will see improvements on par with Figure 2.7 rather than Figure 2.6.

Still, adding imaging information to KWL measurements for these higher-inclination galaxies that would make up the majority of a random sample would cut required exposure times dramatically for spectroscopic observations. If we assume that S/N scales with the square root of exposure time, then even a factor of two improvement in S/N from including the image PA can cut exposure time by a factor of four.

Comparison to Previous Work

As mentioned in Section 2.3.2, our kinematics-only model delivered similar statistical errors as that of Gurri et al. (2020) when tested on their data, so to quantify the benefits of our kinematics + imaging technique on presently-available data sets, we again benchmark against their approach by modifying our mock data to better match the Gurri et al. (2020) data. We move the source galaxy to $z = 0.15$ and the lens to $z = 0.03$, increase the FWHM of the PSF to 1.5", and increase the spatial element size to 0.5" to roughly mimic their data set. We add mock image PA measurements, as we have done for the rest of our mock data, and we assume an error on the image PA of 3 degrees, which is in the middle of the expected error range.

Applying our kinematics + imaging algorithm to these simulated galaxies results in significantly improved statistical uncertainties. Our estimate on the resulting σ_γ values are lower by a factor of $\sim$6 on a per-galaxy basis, consistent with the results from higher redshift mock data in Figure 2.5. This result demonstrates that even for existing data sets at lower redshifts, this technique can increase lensing precision.

However, our inclusion of imaging data does not address the dynamical shape noise term. In order to account for this error, Gurri et al. (2020) estimate the magnitude of the error using a different sample of unsheared galaxies, and find an amplitude that is similar to the statistical error on a per-galaxy basis. This dynamical shape noise term is added in quadrature to determine the final error for each galaxy in their sample. As a result, our estimated factor of 6 improvement in the statistical error, when applied to the full sample in Gurri et al. 2020, only increases their overall 2.5σ shear detection to 3σ.

2.4.3 Survey Design Considerations

While statistical error is small relative to systematic error for low redshift samples, the same is not true at higher redshifts. Resolved spectroscopic measurements become more difficult at higher redshifts due to lower spatial resolution and surface brightness, resulting in higher statistical errors. So the gains made by our imaging + kinematics model will be especially salient at increased redshifts, where there are the added benefits of greater lensing magnitudes (thanks to more favorable lensing kernels) and higher on-sky source densities, allowing for easier collection of larger sample sizes.

If we observe a 1×1 arcmin^2 field near a galaxy cluster (e.g. using MUSE), we

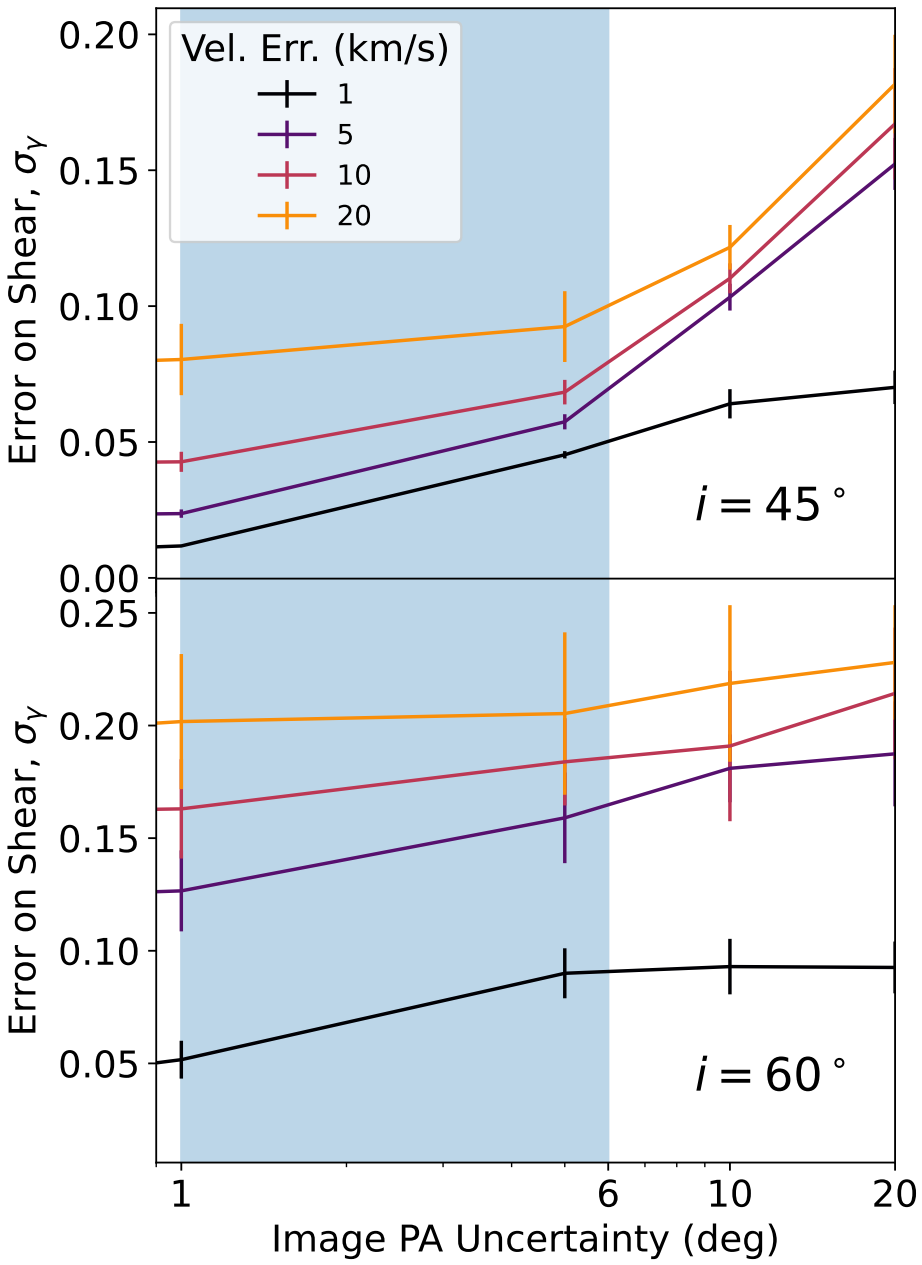

Figure 2.7: The same as Figure 2.6 but for a 45° and 60° galaxies. Higher-inclination galaxies have a much smaller image distortion than lower-inclination galaxies, meaning the model cannot rely on this information as much when constraining the shear. This creates a much larger stratification in velocity error than for lower-inclination galaxies. Overall, σ_γ values are larger, particularly in the 60° galaxy, but improvements to the image PA observation have little effect.

will catch tens of galaxies with velocity fields that are well-defined enough to perform our KWL analysis. A multiplexed fiber IFU instrument like the proposed FOBOS (Bundy et al. 2019) would be able to patrol a significantly wider field and collect velocity data from only the most promising galaxies, enabling a larger sample in less overall exposure time. We can stack the lensing information from the multiple galaxies to obtain higher precision and reduce the random errors introduced by noise or galaxy irregularities either by a weighted average of shear results (as was done in Gurri et al. 2020) or a hierarchical Bayesian model that simultaneously fits all galaxies in a given spatial bin. We expect these individual galaxy "dynamical shape noise" errors to average out to zero in a large sample because they will be randomly and symmetrically distributed (Gurri et al. 2020).

Figures 2.6 and 2.7 show that, with attainable observational errors and low inclinations, it is possible to obtain a σ_γ value comparable in magnitude to the applied shear, resulting in a $\sim 1\sigma$ KWL measurement per galaxy for the input shear of $\gamma_\times \approx 0.06$. However, if we stack multiple such measurements within a radial bin defined by a selection of foreground lenses and assume that the source measurements are statistically independent samples of the ensemble mass density profile of the lenses, then the error on this galaxy–galaxy shear measurement should scale as $n^{-1/2}$. So for a sample of only $n = 9$ galaxies in a spatial bin, σ_γ should be lowered by a factor of 3, raising a 1σ detection to 3σ. This scaling should apply to the systematic error as well since we expect individual galaxy errors to average to zero over a large sample.

Source Redshift

Depending on the instrumentation, if we want to build a larger sample size, higher source density on-sky may be beneficial if the number of independent pointings can be minimized. Source density increases with redshift, as does the magnitude of lensing effects according to Equations 2.5 and 2.7, but there is a trade-off because surface brightness and physical size decrease with redshift. To explore this trade-off, we run our KWL model that incorporates imaging information on the same mock galaxy placed at a range of redshifts. We ignore complications from galaxy evolution like mass/radius growth or dynamical changes. We simulate the observations of different inclination source galaxies at the varying distances as if they are behind a lens at $z = 0.3$. We hold the rest of the observational parameters constant, on-sky spatial resolution, image PA error, central velocity error, and PSF width (unless specified). Maintaining constant errors would require deeper exposures for both imaging and spectroscopy, which we do not account for in this chapter.

Although closer source galaxies have smaller σ_γ uncertainties because of their greater number of spatial resolution elements, Figure 2.8 shows that they deliver a poorer S/N per galaxy because they are simply not sheared as much as more distant galaxies. The top panel shows a high degree of S/N stratification in inclination because the change in image PA is much greater for lower inclinations. We find that there is modest gain in S/N for all inclinations with redshift before leveling off around $z \sim 0.7-1$, the redshift range assumed in this chapter, before keeping a relatively constant value at higher z. This mirrors the trend seen in the overall shear magnitude seen as the red

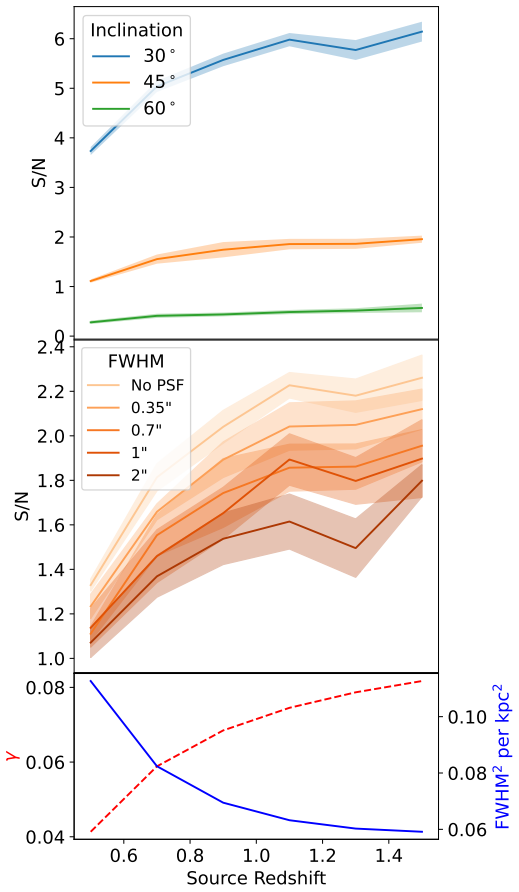

Figure 2.8: Top: The KWL S/N per galaxy for source galaxies at varying inclinations with different redshifts behind a massive halo at $z = 0.3$. We maintain constant on-sky spatial resolution, imaging and velocity errors, and PSF width, ignoring the effects of surface brightness dimming and galaxy evolution. Error bars are based on the random variation from running 10 identical velocity fields with distinct randomized errors. Middle: The 45° inclination galaxy from the top panel but with FWHM of the PSF varied to simulate different observing conditions, still holding on-sky instrumental resolution constant. Realistic observing conditions provide measurements that are a factor of 2–3 lower in S/N compared to an ideal observation without PSF smearing. Improving the PSF by a factor of 2 with something like a ground-layer adaptive optics system to 0.35" leads to S/N gains of about 50%. Bottom: The overall magnitude of the lensing shear, shown in the red dashed line, increases with redshift, making the effects of KWL more noticeable. The fraction of a square FWHM covered by a square kpc in the on-sky plane of the source galaxy, shown in blue solid line, indicates that the PSF becomes very large compared to the spatial scales of the source galaxy, worsening the quality of the fit. S/N largely tracks with shear magnitude.

dashed line in the bottom panel of Figure 2.8.

Another factor that influences precision is the FWHM of the spatial PSF of the resolved kinematic field. The blue line in the bottom panel of Figure 2.8 shows that as the source galaxy redshift increases, the size of the galaxy on-sky becomes smaller relative to the size of the PSF, here represented as the ratio of the square FWHM compared to the size of a square kpc in the plane of the galaxy. Reductions to the FWHM result in higher surface brightness in many cases and more independence of the spatial resolution elements of an IFU observation, which would improve the precision of the velocity field fit even if the spatial sampling is not changed. These types of gains could be obtained in the real world using a ground-layer adaptive optics system (e.g. Chun et al. 2018; Hartke et al. 2020), which would lead to an improvement in seeing by a factor of 1.5 to 2 over a several arcminute-wide field. In the middle panel of Figure 2.8, we vary the FWHM to simulate different observing conditions, from an ideal observation without seeing to a FWHM of 2". We find modest gains in S/N with better seeing, especially at moderate and higher redshifts. However, even fits with poor seeing are able to locate the kinematic axes with acceptable precision, so the effects of better seeing are limited. Still, the increase in surface brightness is valuable for driving down exposure time.

Lens Redshift

To test KWL's ability to probe lenses at various redshifts, we also simulate systems where the source is held at a constant $z = 1$ for varying redshift lenses (Figure 2.9). We find similar dependencies on inclination and FWHM as in Figure 2.8. However,

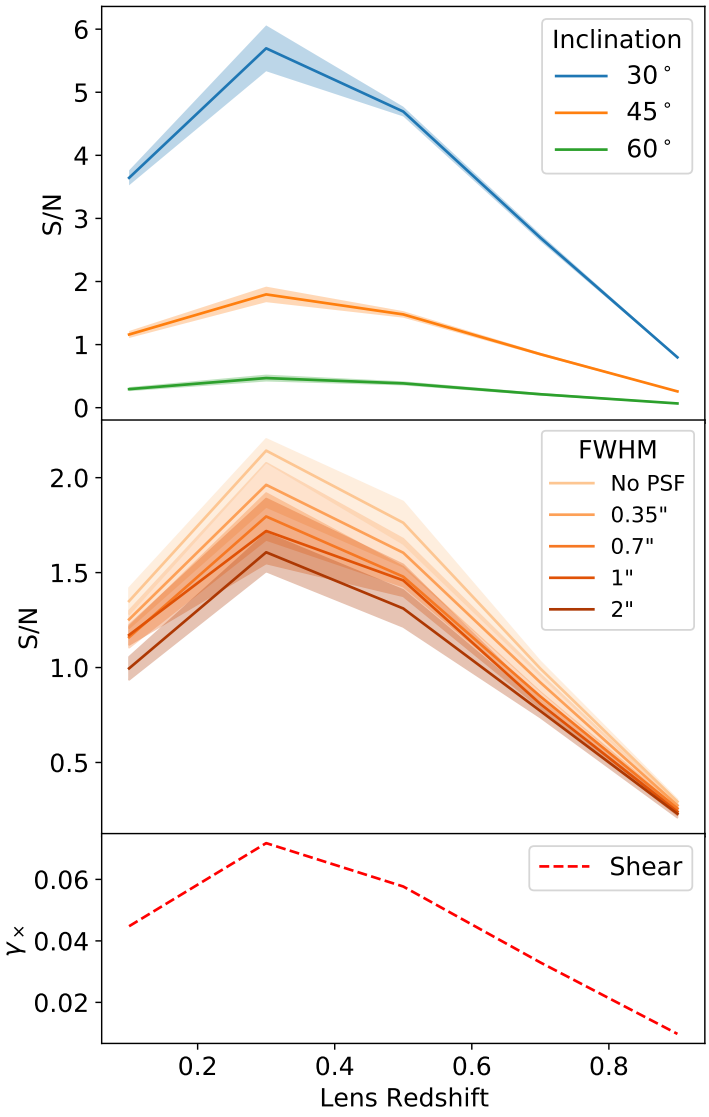

Figure 2.9: The same as Figure 2.8 but holding the source galaxy fixed at $z = 1$ while moving the lens in front of it. The S/N again largely follows the shear magnitude (bottom), which peaks at $z \sim 0.25 - 0.3$ because that is the configuration of angular diameter distances that minimizes the critical radius (Equation 2.5). FWHM^2 per kpc^2 is not shown because it is constant due to the stationary source galaxy.

since shear magnitude scales with the angular diameter distances to the source and the lens (Equation 2.5), shear magnitude peaks at $z \sim 0.3$, falling off sharply from there. In fact, due to how angular diameter distance is defined, for source galaxies further than $z \sim 0.7$, shear magnitude will always be largest for lenses at $0.2 < z < 0.3$. So KWL, like any other lensing technique, will be most sensitive to lenses at these moderate redshifts.

General Strategy

An ideal strategy for a KWL survey would likely be to target low-inclination galaxies that benefit more from the gains imaging can provide. They should be regularly-rotating blue spiral galaxies that are likely to have a high emission line flux for ease of kinematic measurements. The targets should have regular, symmetric isophotes and imaging sufficient to measure image position angles with 1–3 degree uncertainties. If the source galaxy population reaches $z \sim 1$, the ideal lens sample would have a redshift range $z = 0.2$–0.7 to ensure shear magnitudes near the peak of the lensing kernel. Ideally, the major-axis position angles of selected source galaxies should be misaligned with respect to the on-sky direction to the lens center. A 45° offset maximizes the cross-term in the shear. A full optimization of a KWL survey design would take into account the lens and source redshift distributions, the intrinsic variation in galaxy shape, systematic errors in individual galaxies due to dynamical shape noise, and observational constraints such as seeing and exposure time as it relates to brightness dimming, distance, and size.

2.5 Conclusion

We have demonstrated a new formalism for combining imaging and kinematic information that significantly improves the S/N of kinematic weak-lensing observations. Our Bayesian models fit both the kinematic distortion and the photometric offset caused by lensing shear in a given galaxy, leading to decreases in per-galaxy statistical error by a factor of 2 to 6 compared to kinematics alone. If borne out in real observations, this approach opens the door for future studies to more effectively utilize kinematics-based lensing observations of lens samples at moderate redshifts. Even with existing instruments, the methodology appears promising for enabling probes of galaxy cluster halo profiles with greater spatial resolution and S/N while mitigating many of the systematics that affect conventional lensing measurements, like shape noise and intrinsic alignments. Ultimately, this will allow for individual, total mass measurements in the weak-lensing regime for a greater number of clusters.

A purpose-designed survey on a new or existing instrument could provide the observations necessary for a successful KWL measurement. Further study is needed to determine the appropriate redshift range to balance shear magnitude and source density with spatial resolution and surface brightness, while more detailed galaxy rotation models are needed to quantify the systematic effects of kinematic irregularities on KWL measurements.

Chapter 3

The Strength of Bisymmetric Modes in SDSS-IV/MaNGA Barred Galaxy Kinematics

3.1 Introduction

Galactic bars are smooth linear bisymmetric morphological features in the central regions of disk galaxies (Binney & Tremaine 2008). A large fraction of disk galaxies in the local Universe have bars, including the Milky Way (Blitz & Spergel 1991), with more massive, redder galaxies having larger bar fractions (Nair & Abraham 2010; Masters et al. 2011). Barred galaxies have been observed out to $z > 2$ (Guo et al. 2023a), though studies disagree on whether bar fraction decreases with redshift or remains steady (Melvin et al. 2014; Cameron et al. 2010; Sheth et al. 2008; Elmegreen

et al. 2004).

Bars are inherently dynamical structures stemming from perturbations in a galaxy's gravitational potential that lead to destabilizing resonances in stellar orbits (Athanassoula 2002) and the redistribution of angular momentum throughout the disk (Kormendy & Kennicutt 2004). Spontaneous bar formation has been observed in galaxy evolution simulations ranging from relatively simple models of galactic potentials (e.g. Toomre 1981), to low-resolution n-body simulations (e.g. Sellwood & Wilkinson 1993), to modern hydrodynamical simulations (e.g. Rosas-Guevara et al. 2022). Bars can also form due to changes in galactic potential from major mergers or tidal disruptions (Bi et al. 2022) and can evolve over the course of a galaxy's lifetime.

The dynamical structure of bars can be seen through the motions of material within the galaxy. Bars channel interstellar gas radially along their leading edge (Regan et al. 1997), with gas flowing both inwards and outwards (Fragkoudi et al. 2016). This radial motion also redistribute stellar populations within bars, flattening population gradients within the bar as compared to the surrounding disk (Fraser-McKelvie et al. 2019). These motions may play a part in the early quenching of star formation in barred galaxies (Fraser-McKelvie et al. 2020). These structures can also be studied using the Tremaine-Wineberg method (Tremaine & Weinberg 1984), allowing for the determination of bar pattern speed and corotation radius in spatially-resolved spectroscopy of samples of barred galaxies (e.g. Géron et al. 2023; Garma-Oehmichen et al. 2022).

The non-circular motions present in bars cannot be modeled accurately using axisymmetric kinematic models that require a fixed position angle and inclination for

the whole disk (e.g. Andersen & Bershady 2013). Stark et al. (2018) uses the Radon transform to describe position angle variation as a function of radius for galaxies with dynamical disturbances like bars or warps. These techniques can produce accurate models of nonaxisymmetric features in galaxy velocity fields by arbitrarily varying galaxy properties such as position angle, inclination, and rotational velocity in each radial bin, but these independently varying rings are not based on a parametric model. Kinemetry (Krajnović et al. 2006a) uses the techniques of surface photometry to perform harmonic decomposition of the higher-order spatial modes present in 2D velocity fields of irregularly-rotating galaxies. Józsa et al. (2007) uses a series of independent tilted concentric rings to accurately model radial and azimuthal variations in galaxy kinematics.

Velfit (Spekkens & Sellwood 2007; Sellwood & Sánchez 2010, later *DiskFit,* Sellwood & Spekkens 2015) instead proposes a single cohesive model for a galaxy's disk properties. Based on harmonic models from Schoenmakers et al. (1997), the *Velfit* model has global values for inclination and position angle, instead accounting for kinematic distortions with added modes on top of the usual first-order (i.e. completing one sinusoidal velocity oscillation per revolution) tangential velocity of a circularly-rotating disk. They use only physically-motivated terms in their model, restricting it to fitting either first-order radial term that accounts for net inflow/outflow or a combination of second-order radial and tangential terms that are meant to represent bisymmetric motions within bars. These models have had success in describing non-circular motions in radio observations of cold gas rotation in nearby galaxies (e.g. Bisaria et al. 2022; Garma-Oehmichen et al. 2022; Holmes et al. 2015).

In this paper, we build on these earlier kinematic models of non-circular motions to create Nirvana, a flexible code for modeling bisymmetric motions in barred galaxies. We develop our model using a Bayesian forward modeling framework with added constraints within the prior and tuning of the likelihood function that are adjusted to produce more robust, physical-viable results. Additional features include point-spread function (PSF) convolution, dispersion fitting, and surface brightness weighting to make the model more easily applied to lower spatial resolution velocity fields. We investigate the biases present in the model using mock data to calibrate results.

We apply the Nirvana model to a sample of barred galaxies from the SDSS-IV MaNGA(Bundy et al. 2015). Using bar designations from volunteer classifications of MaNGA galaxy morphology from GalaxyZoo: 3D (GZ:3D; Masters et al. 2021), we attempt to fit the stellar and gas-phase velocity fields of all barred MaNGA galaxies and model their non-circular motions with Nirvana, as well as a population-matched sample of unbarred galaxies that we use as a control, generating corresponding samples of velocity field models. We find elevated levels of bisymmetric motion in the barred sample as compared to the unbarred control, and we find that galaxies with elevated bisymmetric velocity terms generally match GZ:3D closely in bar position angle.

This paper is structured as follows: Section 3.2 summarizes the galaxy kinematic data we use and how we prepare it for modeling, as well as the assembly of the samples of barred and unbarred galaxies. Section 3.3 describes our velocity model and PSF convolution methods. Section 3.4 describes Nirvana's fitting algorithm, including the prior and likelihood functions in the Bayesian model. Section 3.5 discusses our eval-

uations of the model's effectiveness when compared to real and mock data. Section 3.6 provides a summary of our work and presents directions for future study.

3.2 MaNGA Data

3.2.1 MaNGA: Mapping Nearby Galaxies at Apache Point Observatory

This paper utilizes data and data products from the Sloan Digital Sky Survey IV (SDSS-IV; York et al. 2000; Blanton et al. 2017) and the Mapping Nearby Galaxies at Apache Point Observatory survey (MaNGA Bundy et al. 2015). MaNGA uses integral field spectroscopy to collect spatially-resolved spectra for ∼10,000 galaxies using the BOSS spectrographs on the 2.5 m telescope at Apache Point Observatory (Gunn et al. 2006). Spectral observations have a resolution of $R \sim 2000$ over a range of 3600 Å $< \lambda <$ 10300 Å with variable exposure time to achieve the desired signal-to-noise ratio (SNR) of 10 in the g-band (Bundy et al. 2015). Fibers are grouped into hexagonal bundles of 19 to 127 fibers that are 12" to 32" in diameter (Drory et al. 2015). Flux calibration and sky subtraction are applied to the observed spectra using simultaneous observations of standard stars and sky within the same field (Yan et al. 2016). The median full-width half-maximum (FWHM) of the point-spread function (PSF) for MaNGA data cubes is 2.5", which roughly corresponds to kiloparsec scales at the targeted redshifts ($z < 0.15$). Observations are dithered and interpolated onto a 0.5" grid of spaxels.

The MaNGA sample is selected to be uniform over i-band absolute magnitude and is divided into two subsamples: the Primary+ sample (∼2/3 of the total sample)

that contains galaxies with spectral coverage out to ∼1.5 effective radii (R_e), and the Secondary sample (∼1/3 of the total sample) where observations extend out to ∼2.5 R_e (Wake et al. 2017). Raw spectroscopic observations are reduced by the MaNGA Data Reduction Pipeline (DRP; Law et al. 2016), and data products such as velocity measurements are derived with the Data Analysis Pipeline (Westfall et al. 2019; Belfiore et al. 2019). All data in this paper are from the seventeenth SDSS data release (DR17; Abdurro'uf et al. 2022), which represents the final data release of the MaNGA survey and contains MaNGA observations and data products from 10,010 unique galaxies. All photometric data in this paper is from the NASA-Sloan Atlas (NSA; Blanton et al. 2011), which uses imaging from SDSS-I, II, and III.

In this paper, we utilize the hybrid binning scheme data products from the DAP, which uses slightly different methods for creating stellar- and gas-phase line-of-sight velocity measurements. For the stellar kinematics, spaxels are Voronoi binned (Cappellari & Copin 2003) to a threshold g-band-weighted SNR of at least 10. These bins are then deconstructed such that the gas kinematics are determined on a spaxel-by-spaxel basis. Both velocity fields are calculated by simultaneously fitting all emission/absorption lines, meaning that all ionized gas tracers are assumed to have the same velocity. For this reason, for the remainder of the paper, when we discuss velocity fields derived from observations of nebular emission, we refer to them as "gas-phase" velocity fields rather than velocity fields associated with a particular emission line. However, each emission line is fit independently for surface brightness and velocity dispersion, so we use the H-alpha values for these quantities when working with gas-phase velocity

data.

3.2.2 Data Processing

Though the MaNGA DAP masks many imperfections in the maps it extracts from the datacubes, there are still outliers in the data that inhibit our ability to produce a successful fit.

Specifically, the DAP also sometimes produces velocity measurements for individual spaxels that differ greatly from the neighboring spaxels due to systematic errors caused by low SNR (Westfall et al. 2019; Belfiore et al. 2019). To identify these spurious velocity measurements, we convolve a kernel to blur the kinematic data that is equivalent to the reported PSF, smearing the data over a scale that should correspond to the observational differences in the data. We then mask any spaxels where the magnitude of the difference between the velocity and dispersion maps and their blurred counterparts, since any spaxels that differ too greatly from their neighbors must be nonphysical. Through experimentation, we determined any spaxels with differences of more than 50 km/s are likely erroneous, so they are masked.

This process also necessitates the masking of any large spatial bins. Such bins are frequently used on the outskirts of stellar velocity fields where the MaNGA DAP groups spaxels together, attempting to reach a minimum required SNR for reliable velocity dispersion measurement. However, because these bins cover such large areas, the differences in velocity between adjacent bins can become large enough to trigger the above clipping threshold, removing spaxels that otherwise contain high-fidelity velocity measurements. For this reason, we mask any bins that consist of more than 10 spaxels.

We then mask out any spaxels that have a surface brightness flux of less than 3×10^{-19} ergs/s/cm^2 per spaxel in the $H\alpha$ flux map or an $H\alpha$ amplitude-to-noise ratio (ANR) of less than 5 for gas velocity fields, or 3×10^{-19} ergs/s/cm^2/$\AA$ per spaxel in the stellar flux map for stellar velocity fields. These values were experimentally determined to best remove low-quality velocity measurements on the outskirts of galaxies.

Finally, we attempt to remove any regions of the velocity field that do not appear to be part of the same rotating system as the rest of the galaxy. Many MaNGA IFUs contain foreground/background sources or merging companions that have distinct velocity fields from the main target, so it would be inappropriate to fit a single rotating disk to the data. To mask these, we perform a preliminary fit to the kinematics using an axisymmetric model and subtract the model from the data to obtain a map of the residuals. If the data are well represented by this model, the residuals should be randomly distributed along a Gaussian distribution according to the Central Limit Theorem, and any deviations from Gaussianity represent possible signatures of asymmetry that we may want to mask. In order to preserve the genuine bisymmetric features we are attempting to model, we mask only the spaxels that differ from the mean of the residuals by more than 10 standard deviations, a value we experimentally determined removes unwanted companions but still preserves real bisymmetric features. After masking these spaxels, we again fit the axisymmetric model and remove the outliers in the residuals, repeating the process until the number of masked spaxels stabilizes.

If, at the end of this process, the galaxy is left with only 20% or less of its original number of spaxels unmasked, the velocity field is considered to be unsuitable

for velocity field fitting and it is not fit.

Our rotation curve models are piece-wise linear functions defined on a set of concentric elliptical rings. To construct the radius of each ring, we determine the position of the minor axis and inclination of the galaxy our preliminary axisymmetric model (see above) and transform the spaxel/bin coordinates into in-plane elliptical coordinates using Equations 3.1 and 3.2. We then subdivide these coordinates into concentric rings using the method described further in Section 3.3. If more than 75% of the spaxels in a given elliptical annulus are masked, all spaxels are discarded and the relevant ring is removed. This prevents a small number of spaxels from having an undue influence on the model, particularly in galactic outskirts. Any galaxies with 2 or fewer elliptical rings are discarded for having insufficient spatial resolution.

3.2.3 Sample

Our goal is to assess the ability of Nirvana to accurately model and quantify bisymmetric distortions in the velocity fields of MaNGA galaxies. To this end, we define two galaxy samples, one of barred galaxies where we expect prominent bisymmetric kinematic distortions, and a second matched control population of galaxies that do not appear to be barred (see Section 3.2.4). To create these samples, we use the existing Galaxy Zoo: 3D catalog (GZ:3D; Masters et al. 2021), a crowd-sourced project for identifying morphological features in SDSS images of MaNGA galaxies. Volunteers drew regions on images of all MaNGA galaxies from the SDSS-I/II survey (Gunn et al. 1998; York et al. 2000) to indicate which morphological feature each pixel belonged to, yielding vote counts for each pixel that we can use to determine which galaxies have

bars as well as the shape of the bar. We chose this catalog over others because it already provides information on bar position and shape within the galaxy, allowing us to more easily compare our models to existing imaging.

We define a pixel as being part of the bar if more than 20% of volunteers designated it as such, and we define a galaxy as "barred" if it has more than at least one spaxel that is part of a bar, the methodology recommended by Krishnarao et al. (2020) and Masters et al. (2021). GZ:3D provides us not only with a binary classification of barred versus unbarred galaxies but also with more detailed spatial information that we will compare to our kinematic modeling results. In the MaNGA sample, there are 1593 such galaxies representing 14.1% of the total sample. Since MaNGA provides both stellar and gas velocity maps, we model both using Nirvana, but fit the two tracers independently.

Major mergers can greatly disrupt the internal kinematics of disk galaxies, so we also remove any galaxies that are obviously undergoing a merger. GZ:3D has volunteers mark the centers of any galaxies that are in the image of the target galaxy and the surrounding area, so we remove any galaxies where the average number of centers marked by volunteers was greater than 1.5, a threshold we experimentally determined to work best. We find a total of 98 mergers in our original list of barred galaxies and remove them from our final sample to reduce extra sources of non-circular motion.

After these cuts, Nirvana successfully converges on suitable velocity models for 973 stellar velocity fields (66.6% of the initial sample) and 1012 gas-phase velocity fields (69.3%). 722 galaxies (49.4%) have both stellar and gas velocity fits, and 1263 unique

galaxies have either a stellar or gas-phase velocity field model. These sets of successfully fit galaxies represents our final Nirvana-MaNGA sample of barred galaxies that we will work with for the remainder of this paper.

The cuts in our data processing tend to bias the Nirvana-MaNGA sample away from redder galaxies because of their lower gas-phase emission flux, resulting in a sample of galaxies that fall almost entirely within the "blue cloud" of galaxies on the color-magnitude diagram. As shown in Figure 3.1, the majority of the sample lies between $10^9 - 10^{11} M_\odot$, as described by the elliptical Petrosian photometry data given in the NASA-Sloan Atlas (NSA; Blanton et al. 2011). The sample is almost entirely blue, as measured by the NSA elliptical Petrosian $NUV - r$, with only a few galaxies in the green valley and red sequence. There are peaks in the mass distribution around $10^{9.3}$ and $10^{10.4}$. The first peak corresponds to a mass range with large representation in the overall MaNGA sample of blue galaxies, and the second indicates a bias towards larger blue galaxies overall within the Nirvana sample.

3.2.4 Control Sample

To isolate the effect of galactic bars on our main sample, we construct a sample of unbarred galaxies to serve as a control. Such a sample will allow us to compare the strength of the bisymmetric distortions measured by Nirvana to our main sample, where the bisymmetric distortions are expected to be more significant. This control should therefore resemble the population of galaxies in our main sample, such that we can effectively isolate the effect of the bars. To build the control sample, we match each barred galaxy in the final sample to a galaxy with similar NSA elliptical Petrosian stellar

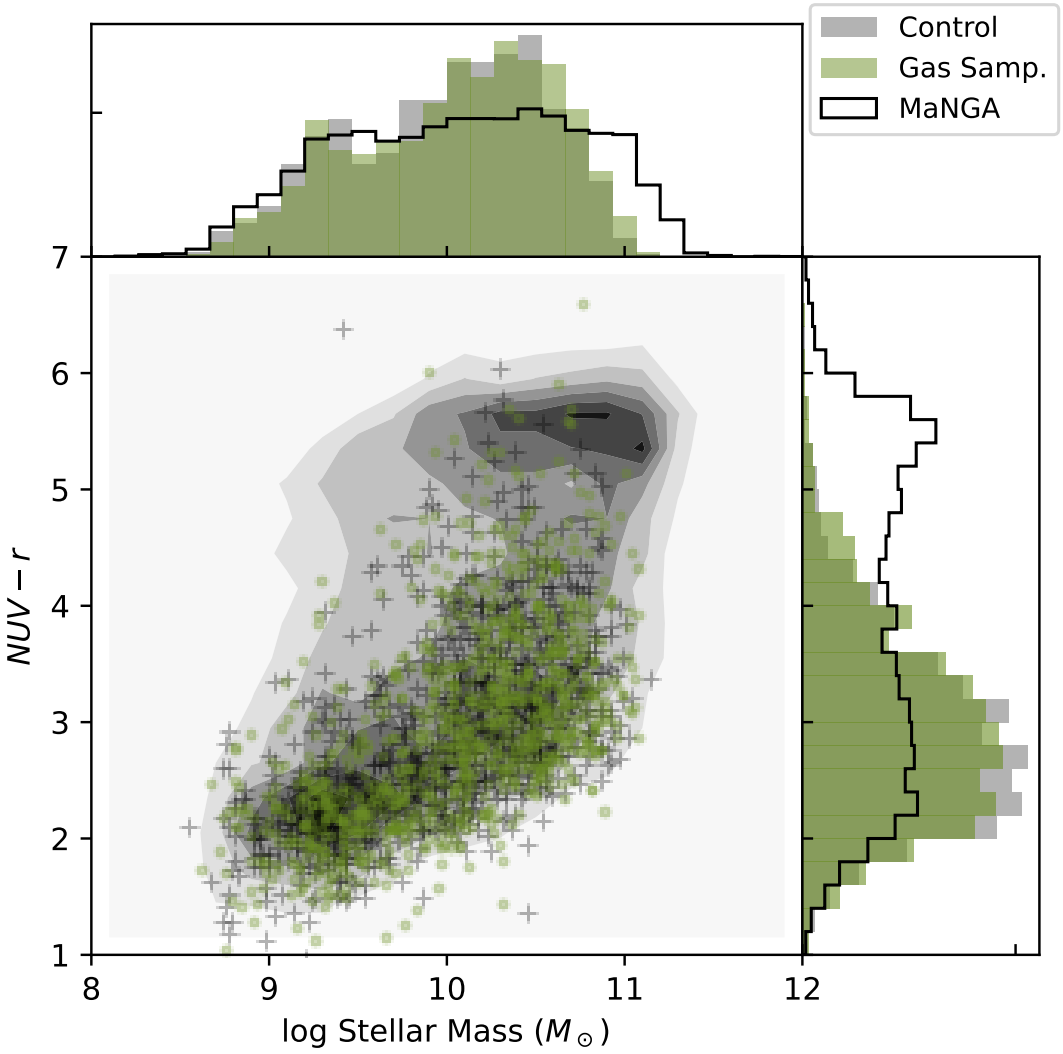

Figure 3.1: Stellar masses and colors of the Nirvana gas-phase sample of barred galaxies (green circles), the population-matched control sample (gray pluses), and the MaNGA sample as a whole (contours). The sample galaxies lie almost entirely within the "blue cloud," with only a small number having green or red colors, and there is a greater fraction of high-mass blue galaxies than in the overall MaNGA sample. The control sample of unbarred galaxies is demographically extremely close to the Nirvana sample by virtue of the matching process.

mass, color, axis ratio (b/a), and effective radius ($R_{\rm eff}$) using linear sum assignment (Crouse 2016), which produces a set of unique galaxy pairs with matched population parameters.

For each of the parameters listed, we normalize the range of the MaNGA population to fall roughly between 0 and 1.[5] The end points of the normalized parameter distributions are as follows:

- Color ($NUV - r$): 0 to 10.
- Log stellar mass: 10^8 to $10^{12} M_\odot$.
- Effective radius: 0 to 18 arcsec.
- Axis ratio: 0 to 1.

The median distance between galaxy pairs in the normalized parameter space 0.038, so the population statistics for the control sample are nearly identical to the barred sample, as seen in Figures 3.1.

3.3 Bisymmetric Kinematic Model

To model non-circular motions in disk galaxies, we adopt a formalism based on Spekkens & Sellwood (2007). Our models use a cylindrical coordinate system, with the disk plan at $z = 0$, projected on the sky. To map the rectilinear on-sky spaxel

[5]Some ranges were chosen to capture the range of galaxies in the full MaNGA sample, so they may appear oversized when considering just our sample of barred galaxies. However, changing the bounds has only a small effect on the overall properties of the galaxies chosen for the control.

coordinates onto the projected galaxy coordinates, we use the following transformations:

$$r = \left[(x - x_c)^2 + (y - y_c)^2\right]^{1/2} \tag{3.1}$$

$$\theta = \arctan\left(\frac{x \sin\phi - y \cos\phi}{\cos i \, (x \cos\phi + y \sin\phi)}\right), \tag{3.2}$$

for x and y center position x_c and y_c and on-sky position angle ϕ, measured from N through E along the direction of the receding side of the major axis.

We split the velocity field $V(r, \theta)$ into its radial and tangential components $V_r(r, \theta)$ and $V_t(r, \theta)$, additionally breaking each component down into its Fourier modes. Spekkens & Sellwood (2007) show that some bisymmetric (second-order) terms are degenerate with a first-order radial term. Here, we neglect the first-order radial term, effectively assuming that most galaxies have no coherent radial inflows or outflows.

We limit our model to only the primary rotation term (first-order tangential) and second-order terms to focus on the bisymmetric flows that are physically associated with bars, rather than higher-order modes that may describe irregularities in velocity fields more exactly (e.g. Krajnović et al. 2006a). However, Spekkens & Sellwood (2007) note that sinusoidal models of order m projected in an elliptical coordinate system are degenerate with models of order $m \pm 1$, so some third-order features are present in the models. We address the first-order degeneracies in Section 3.4.2.

The resulting model is shown below:

$$\begin{aligned} V(r,\theta) &= V_{sys} + \sin i \Big[V_t(r) \cos\theta \\ &\quad - V_{2t}(r) \cos\big(2(\theta-\phi_b)\big) \cos\theta \\ &\quad - V_{2r}(r) \sin\big(2(\theta-\phi_b)\big) \sin\theta \Big]. \end{aligned} \tag{3.3}$$

The bisymmetric position angle ϕ_b is defined as the in-plane angular difference between the first- and second-order rotational terms. We also discretize the kinematic components, V_t, V_{2t}, and V_{2r}, using a piece-wise linear function with breakpoints at equally-spaced in-plane radii. The breakpoint radii are set such that their separation is defined as half of the reconstructed FWHM of the MaNGA PSF along the minor axis of the galaxy, thus Nyquist sampling the changes in velocity along the position angle where they are most compressed. These breakpoint radii are linearly spaced along the minor axis until the edge of the MaNGA IFU is reached, as described in Section 3.2.2. Additional details regarding the construction of the kinematic models are addressed in Section 3.4. We note that the inner-most breakpoint of the functions is at $R = 0$, and we force all velocity components to be 0 km/s at this position.

Nirvana also goes beyond previous works by simultaneously modeling the velocity dispersion of the input galaxy. In addition to providing a more complete kinematic understanding of the galaxy, the dispersion also helps to more accurately model the effects of beam smearing by incorporating both spatial and spectral smearing in the final velocity measurements. The increased fidelity and generality of our beam smearing also differentiates Nirvana from prior work (e.g. Spekkens & Sellwood 2007). Since velocity

dispersion is a second-order moment, we assume that it is radially symmetric (Binney & Tremaine 2008). Therefore, we do not need a complex model to decompose it like we do for the velocity, instead modeling it as a single piece-wise curve $\sigma(r)$ defined over the radius of the galaxy and projected in-plane. However, such simple axisymmetric models may be limited in their ability to describe galaxies that are not axisymmetric themselves.

Once the intrinsic models for velocity and dispersion have been generated, they are convolved with the MaNGA PSF to include the effects of beam smearing, which can be directly compared with the observed data. The convolutions performed are

$$I_{\rm obs} = I * P, \tag{3.4}$$

$$V_{\rm obs} = \frac{(IV) * P}{I_{\rm obs}}, \text{and} \tag{3.5}$$

$$\sigma_{\rm obs} = \left[\frac{I(V^2+\sigma^2) * P}{I_{\rm obs}} - V_{\rm obs}^2\right]^{1/2}, \tag{3.6}$$

where $*$ is the convolution operator, P is the on-sky point-spread function, and the quantities I, V, and σ are all intrinsic properties of the galaxy along the line-of-sight, before convolution with the PSF. Note that a limitation of our model is that we do not model the surface brightness, I, (cf. Varidel et al. 2019) and we do not have access to a higher resolution observations of I; we use the observed surface-brightness distribution.

3.4 Fitting Algorithm

The core function of Nirvana is to represent the input galaxy using the model described above. To fit the above model to the data, we construct a Bayesian forward model. We choose this formalism rather than a least-squares optimizer like Spekkens & Sellwood (2007) because of its ability to compensate for local minima in the likelihood, account for covariances between parameters, and utilize priors when navigating probability space. We specifically chose the Bayesian code `dynesty` (Speagle 2020), a Python package implementing nested sampling (Skilling 2004, 2006) utilizing multi-ellipsoid bounds (Feroz et al. 2009) due to its strengths in describing high-dimensional multi-modal likelihood spaces.

In this section, we describe the prior and likelihood functions used by Nirvana as well as the biases and constraints that led to their design. An example of the results from running the model is given in Section 3.4.3.

3.4.1 Priors

Position angles, velocities, and centers

To keep the fitting process relatively galaxy-agnostic, we endeavored to keep the priors as uninformative as possible. We chose a uniform prior over all angles for position angle ϕ rather than setting a narrower prior probability distribution based on preliminary axisymmetric fits to allow for complicating factors such as irregular galaxy shapes or non-circular motions that could lead to significant biases in the axisymmetric position angle. Similarly, we use a uniform prior over all angles for the second order

position angle ϕ_b since we do not have any information on the likely orientations of higher order components for any of the galaxies.

Rather than attempting to construct an informed prior for the individual velocity components based on predicted rotation curve shapes, we instead attempt to be neutral and keep the model as free from parametric models as possible by using uniform priors over a reasonable velocity range. We allow the magnitudes of the individual in-plane velocity components V_t, V_{2t}, and V_{2r} to vary between 0 and 400 km/s in each bin, with the center bin held fixed at 0 km/s. Similarly, the prior on velocity dispersion magnitude σ is uniform over 0 to 300 km/s.

We have found that axisymmetric fits are almost always capable of recovering the systemic velocity well, so we restrict the V_{sys} to be within $\pm$60 km/s of the value returned by the preliminary fit. We also rely on the MaNGA IFU placement for the position of the center of the galaxy, restricting the galactic center to be within a $4''$ square box surrounding the center of the MaNGA bundle. We determined the size of the bounding box by noticing that in preliminary runs, almost all galaxy models that had kinematic centers more than $2''$ from the IFU center were fit incorrectly, and that the results from the fit were improved by restricting the position of the dynamical center. Essentially all isolated galaxies are centered in the MaNGA IFU, and galaxies with kinematic centers outside of this bounding box are almost always not isolated or are undergoing a merger, making them unsuitable for our modeling approach.

Inclination

The most restrictive prior we have placed on the fitting algorithm is on the inclination, which we tie to the photometric inclination using a relatively tight Gaussian prior. We derive the photometric inclination i_p of each galaxy from its elliptical Petrosian axis ratio q, as provided by the NASA-Sloan Atlas (Blanton et al. 2011). We convert this value to a photometric inclination as follows:

$$\cos^2 i_p = \frac{q^2 - q_0^2}{1 - q_0^2}, \tag{3.7}$$

where q_0 is the intrinsic oblateness of the galaxy. We do not have any information on the value of q_0 for each individual galaxy since such information would require detailed dynamical modeling of each galaxy, though it tends to correlate with scale length in late-type galaxies (Bershady et al. 2010). However, previous studies (e.g. Weijmans et al. 2014; Padilla & Strauss 2008; Lambas et al. 1992) find that for rotating galaxies like disks and fast-rotating ellipticals, $q_0 \approx 0.20 - 0.25$, so we choose a nominal value of $q_0 = 0.2$ for all galaxies in our model, similar to the Bershady et al. (2010) estimate of about 0.06 to 0.20. These inclinations are more reliable than kinematically-derived inclinations from axisymmetric fits that are sometimes adversely affected by kinematic asymmetries.

We originally defined the prior as uniform distribution with bounds $\pm 20°$ from i_p. However, inherent degeneracies in the Nirvana model cause a strong tendency to fit galaxy inclinations that are significantly higher than either the input inclinations (in the case of mock galaxies) or the inclination derived from photometry (in the case of

real data), necessitating a stricter prior to counteract the bias. While we do not expect perfect correspondence between the kinematic and photometric inclinations because they are tracing different components of the galaxy's structure, the systematic bias to high inclination indicated an underlying problem with the current state of the priors. As shown in the top panel of Figure 3.2, most models were driven to the upper limit of this uniform prior.

To mitigate the bias, we instead used a Gaussian prior centered on the photometric inclination and a 3° standard deviation. Unsurprisingly, this tighter constraint leads to much closer agreement with the photometric inclination, with the bias reduced to $4-5°$, as seen in Figure 3.2. A bias of this size is not much larger than that of existing axisymmetric models (e.g. Andersen & Bershady 2013). However, if the photometric and kinematic inclinations are indeed vastly different, e.g. in a galaxy with multiple kinematically-decoupled components, this prior is still flexible enough to allow Nirvana to fit the disk correctly.[6] The bottom panel of Figure 3.2 shows a comparison between the photometric inclinations of MaNGA galaxies calculated using Equation 3.7 and the kinematic inclinations recovered by Nirvana. Due to the inherent degeneracy between inclination and rotational velocity, these stronger priors also have an effect on the recovered velocity profiles; the smaller model inclinations require larger velocity components to match the same line-of-sight velocity observations.

[6]Such misaligned structures are more common in early-type galaxies (Corsini 2014), which are almost entirely absent from the Nirvana-MaNGA sample, so this situation is unlikely to be a major factor when Nirvana is applied to barred spirals.

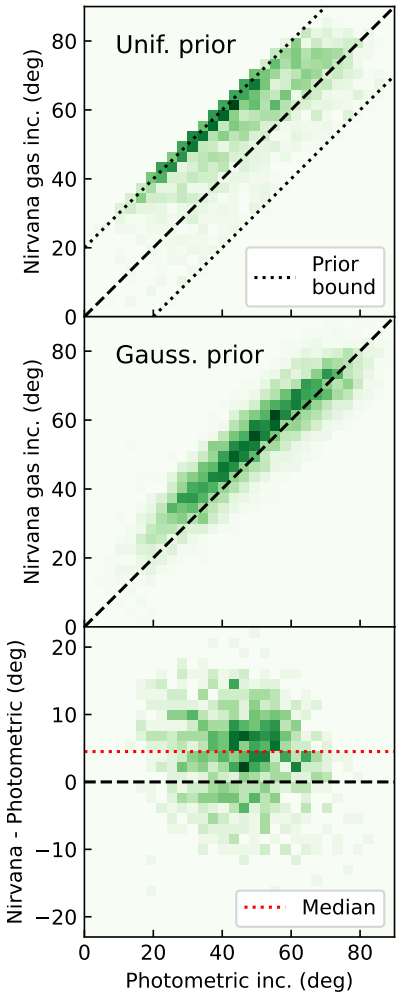

Figure 3.2: The effects of different inclination priors described in Section 3.4.1 on the inclination recovered by Nirvana as compared to inclinations derived from photometry. Top: A uniform prior centered on the photometric inclination with a width of $\pm 20°$. Nirvana has a significant tendency to produce inclinations that are much too high, often running up against the prior bound. Middle: A Gaussian prior centered on the photometric inclination with a standard deviation of $3°$ produces a much better agreement with photometry while still allowing some freedom in the fit. Bottom: A comparison between the inclinations derived from photometry and the inclinations recovered by Nirvana in our sample of barred galaxies with a Gaussian prior. There is a systematic bias of $4 - 5°$, which is in line with biases seen in other similar models.

3.4.2 Likelihood

The Nirvana likelihood function is based primarily on a standard Gaussian likelihood. At each iteration of the fitting process, we generate a velocity field model according to the steps outlined in Section 3.3 using the latest parameter guesses. We then compute a χ^2 value between the original data and the model, weighting each spaxel by its velocity variance σ_v^2 as reported by the MaNGA DAP with an extra error term of 5 km/s added in quadrature, summing over all unmasked spatial elements to obtain one value for the whole galaxy:

$$\chi_v^2 = \sum \frac{(V - V_{\rm mod})^2}{\sigma_v^2}. \tag{3.8}$$

We calculate separate χ^2 likelihoods for the velocity and dispersion data, substituting in the square of the physical velocity dispersion

$$\sigma^2 = \sigma_{\rm obs}^2 - \sigma_{\rm corr}^2, \tag{3.9}$$

where $\sigma_{\rm obs}$ is the velocity dispersion reported by the MaNGA DAP and $\sigma_{\rm corr}$ is an instrumental correction (Westfall et al. 2019).[7] Using the reported errors on dispersion σ_σ plus an extra error of 5 km/s added in quadrature, the resulting chi-squared term is as follows:

$$\chi_v^2 = \sum_{\rm elem.} \frac{(\sigma_- \sigma_{\rm mod})^2}{\sigma_\sigma^2}. \tag{3.10}$$

[7] The correction factor for the gas kinematics is the instrumental resolution at the best-fitting line wavelength; for the stellar kinematics, it is a correction that accounts for the difference in spectral resolution between the MaNGA spectra and the stellar templates used to measure the kinematics.

The resulting chi-squared terms are then added together as part of the final likelihood. In addition to these chi-square terms, we include specific penalty functions that mitigate biases and unphysical results discovered while testing our approach. Although these penalties come at the expense of the objectivity of the modeling procedure, they provide more robust final results. We describe each penalty, P_1 and P_2 in the following two subsections. The final likelihood function L is represented by:

$$\log L = -\chi_v^2 - \chi_\sigma^2 - P_{1,v} - P_{1,\sigma} - P_2. \tag{3.11}$$

Smoothing penalty

To incentivize the model to produce smoother radial profiles, we impose a penalty if the second derivative of the rotation curve shape is high for any of the components. We approximate the second derivative by taking the difference between the kinematic components in each bin and the mean of the values of the same component in neighboring bins. The smoothing penalty P_1 is the sum of the difference between the mean for all bins, scaled by the magnitude of the velocity component in that bin and weighted by a coefficient w_1:

$$P_1 = w_1 \sum_i^{N_{bins}} \frac{V_i - (V_{i-1} + V_{i+1})/2}{V_i}. \tag{3.12}$$

This penalty is applied for all velocity components as well as the velocity dispersion, and the resulting penalty is subtracted from the log likelihood. We determined experimentally that a weight of $w_{1,v} = 10$ for velocity components and $w_{1,\sigma} = 1$ for velocity

dispersion results in fits that fit radial differences in velocity well but help to moderate sharp discontinuities in the shapes of the velocity profiles.

Second-order velocity penalty

Testing of mock galaxies shows a notable covariance in the posteriors of the inclination and the second-order radial component of the velocity V_{2r}. The velocity field residuals for an improper inclination have similar patterns to the effects of V_{2r}, resulting in Nirvana sometimes preferring to return inclinations that were too high and then counteract the residuals from that mistake with elevated V_{2r} values.

This can be seen in Figure 3.3, where galaxies with erroneously high inclinations often also have higher V_{2r}. We construct a set of mock galaxies by feeding model parameters derived from real galaxies at similar inclinations (one unbarred disk and one barred disk with elevated second-order velocity terms) back into the Nirvana code and superimposing real residuals in order to mimic physical galaxies. We then use Nirvana to fit these mock galaxies to test its ability to recover input parameters in realistic data. As mentioned before, Nirvana shows a tendency to fit erroneously high inclinations by utilizing similarly erroneous V_{2r} values, as shown in Figure 3.3.

Additionally, in the limit where $V_2 \equiv V_{2t} = V_{2r}$, we can use the angle-sum identity to rewrite Equation 3.3 as:

$$\frac{V_{\rm los} - V_{\rm sys}}{\sin i} = V_t \cos\theta - V_2 \cos(\theta - 2\phi_b). \tag{3.13}$$

That is, the combination of the second-order components mimic a first-order tangential

component that is phase-shifted by $2\phi_b$, commonly referred to as a position-angle warp. This makes it possible for the model to effectively trade between V_t and V_2 by adjusting the relevant position angles, ϕ and ϕ_b. This degeneracy between mode m and modes $m \pm 1$ was noted by Schoenmakers et al. (1997) and Spekkens & Sellwood (2007), and we noted instances of this degeneracy influencing our model results during Nirvana development.

We disincentivize the ability of the model to trade between first- and second-order components by imposing a penalty on the likelihood for models that have second order velocity terms that are large in comparison to the first order velocity using the following term:

$$P_2 = w_2 \sum_{V=V_{2t},V_{2r}} \frac{\bar{V} - \bar{V}_t}{\bar{V}_t}, \tag{3.14}$$

where barred quantities represent the means of the respective velocity profiles. w_2 is a separate coefficient that we experimentally determined should be set to $w_2 = 500$ to produce results that capture bisymmetric velocity distortions when they are present but do not overfit them when they are not present.

3.4.3 Example Results

An example result from this model for barred MaNGA galaxy 8078-12703 is shown in Figures 3.4 and 3.5 for gas-phase and stellar velocity fields respectively. The nonaxisymmetry of the bar is obvious in both the image and the velocity field, where a large central disturbance is visible in the otherwise orderly rotation of the disk. When the Nirvana model is applied, it recovers a first-order tangential rotation curve that

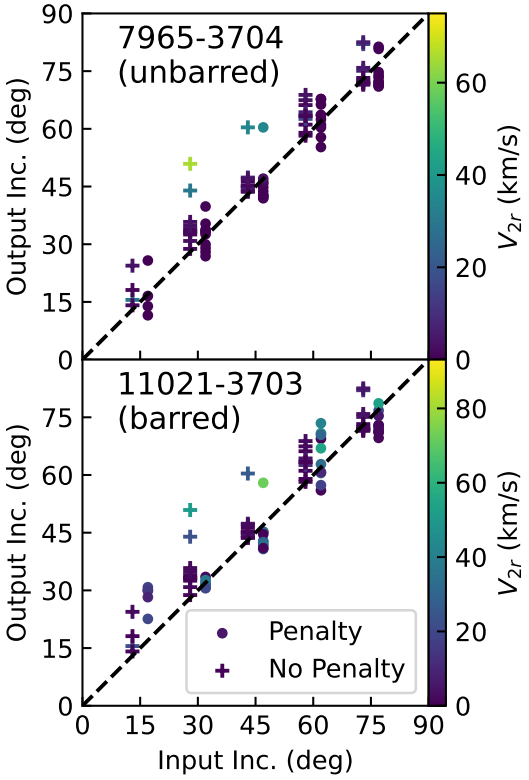

Figure 3.3: The effect of penalizing models that use high second-order velocities on the inclination bias. We construct a set of mock galaxies using the Nirvana velocity fields an unbarred galaxy (MaNGA plate and IFU number 7965-3704) with V_{2t} and V_{2r} close to zero on top, and a barred galaxy with elevated central V_{2t} and V_{2r} (11021-3703) on the bottom. We generate idealized models using these velocity profiles at different inclinations and add real residuals and fit those mocks with Nirvana, allowing us to compare input and output parameters. We find that when unfettered, Nirvana has a tendency to produce erroneously high inclination models, which elevate V_{2r} values due to degeneracies. When we impose a penalty on high second-order velocity terms as described in Section 3.4.2, the bias is greatly reduced.

roughly resembles a conventional model for a disk galaxy, rising quickly to a maximum value before leveling off at larger radii. The second-order components are present as a relatively large component of the rotation in the central part of the galaxy, but their influence quickly diminishes at larger radii as the influence of the bar lessens.

Figures 3.4 and 3.5 also demonstrate that, when compared to an axisymmetric mode, Nirvana is able to more accurately model the observed 2D velocity field. The axisymmetric model leaves large and spatially-correlated residuals, indicating that the model is unable to capture all of the features seen in the data, whereas the Nirvana model's residuals are much smaller and much more randomly distributed. The maps for the individual velocity modes of the Nirvana model as well as the components of the actual MaNGA data those modes are fitting can be seen in Figures 3.4 and 3.5 for gas-phase and stellar velocity fields respectively. The shapes of the components of the data generally match the shape of the velocity mode maps, justifying the physical premise of our model.

The middle row of Figure 3.6 shows a breakdown of the separate velocity components that make up the final velocity field model of the same galaxy. The bottom row shows the residuals left when subtracting different combinations of rotational terms from the original MaNGA data to leave only a single component in the data, yielding views of each component of the data that Nirvana is modelling. Comparing the velocity components of the second row to the residuals in the third row, we see close correspondence between our model terms and the noncircular motions present in the central bar region of the galaxy.

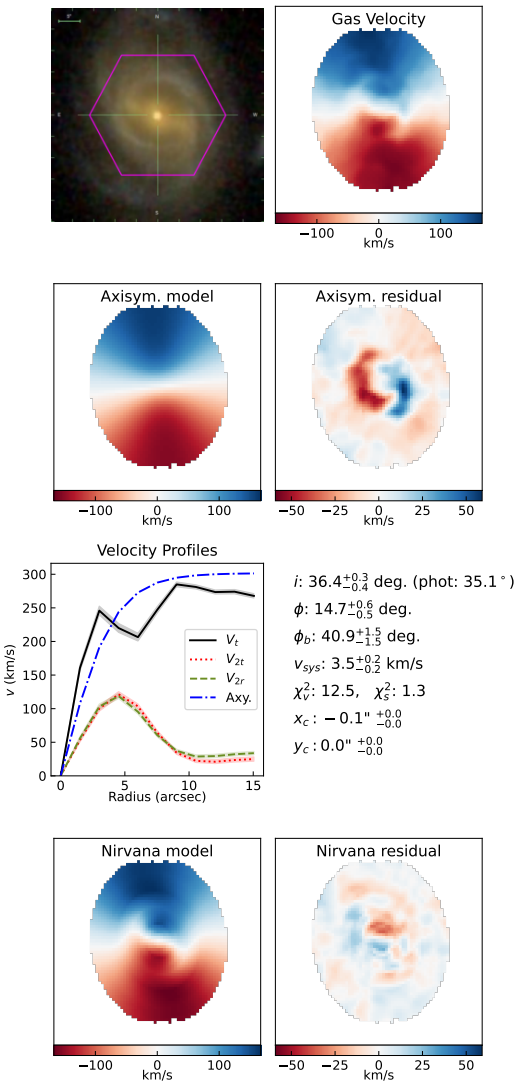

Figure 3.4: The Nirvana model of the gas-phase velocity field of barred MaNGA galaxy 8078-12703. Top row: the SDSS image of the galaxy with the MaNGA IFU boundary overlaid in magenta, and the gas-phase velocity field. Second row: An axisymmetric model of the velocity field and the model residuals. Note the strong deviations near the center. Third row: the best-fitting radial velocity profiles of the three velocity components fit by the Nirvana model (V_t shown in solid black, V_{2t} in dotted red, and V_{2r} in dashed green) with 1σ errors, along with the rotation curve found by our parametric axisymmetric fitting algorithm (dot-dashed blue), and the rest of the parameters from the Nirvana model with 1σ errors. Bottom row: the Nirvana velocity field model of the galaxy, and the residuals from subtracting the Nirvana velocity model from the MaNGA velocity field. Compared to the axisymmetric model, the residuals are significantly reduced and are much less spatially correlated, indicating a more suitable model.

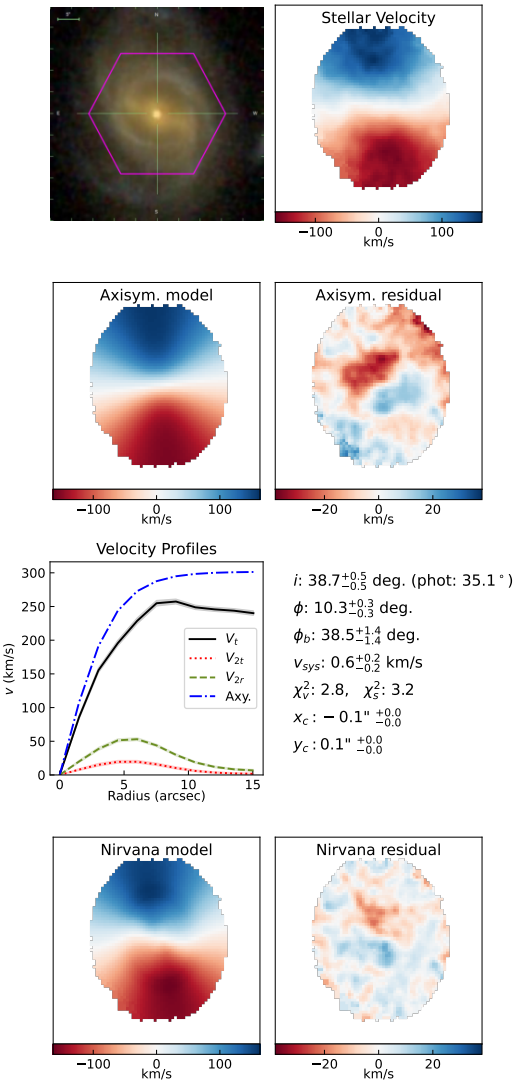

Figure 3.5: The same as Figure 3.4 but for the stellar velocity field.

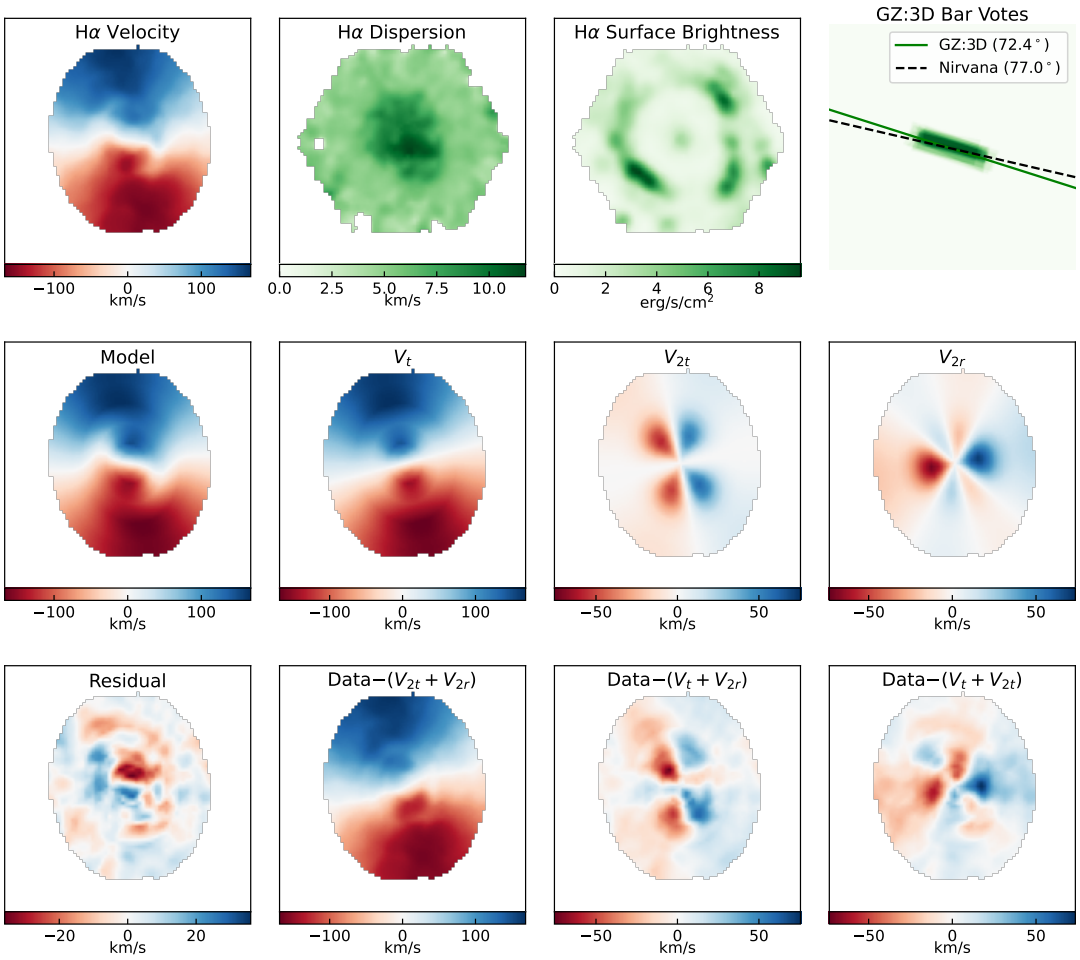

Figure 3.6: The separate pieces of MaNGA data that are fed to the Nirvana model and the individual components of the velocity field model. Top row: the MaNGA $H\alpha$ velocity field, velocity dispersion, and surface brightness. Top right: the bar classification votes from Galaxy Zoo: 3D and resulting on-sky bar position angles from GZ:3D and the independent Nirvana velocity model. Middle row: the Nirvana velocity field model, and all of the individual components of the model broken out separately. Bottom row: The residual of the velocity field model, and the component of the MaNGA velocity data that corresponds to the above velocity component.

3.5 Results

In this section, we discuss the performance of the model on real and simulated galaxies in order to contextualize its results.

3.5.1 Projection biases

When modeling bisymmetric distortions in velocity fields caused by bar in disk galaxies, the angular difference between the position angles of the major axis ϕ (the first order velocity component) and the bar ϕ_b (the second order velocity component) greatly affects how the bar appears in the line-of-sight velocity data. Bars that are diagonal to the major axis will create obvious distortions in the velocity field, whereas bars that are aligned or anti-aligned with the major or minor axis will only appear as small fluctuations in the dominant first order rotational component, as shown in Figure 3.7. Nirvana often models these disturbances without second-order velocity components, leading to significant difficulties in accurately recovering aligned and anti-aligned bars, as mentioned originally by Spekkens & Sellwood (2007).

In the set of mocks shown in Figure 3.8, we see that galaxies with ϕ_b values that are close to aligned/anti-aligned, Nirvana has a preference for increasing relative ϕ_b values between 0° and 45° and decreasing values between 45° and 90°. The effect of this is to bias ϕ_b to be closer to a 45° or 135° offset from ϕ than reality, and the second-order velocity profiles for these biased bars are often less than the input velocity profiles.

The origins of this bias are unclear. Because more diagonal ϕ_b produces a

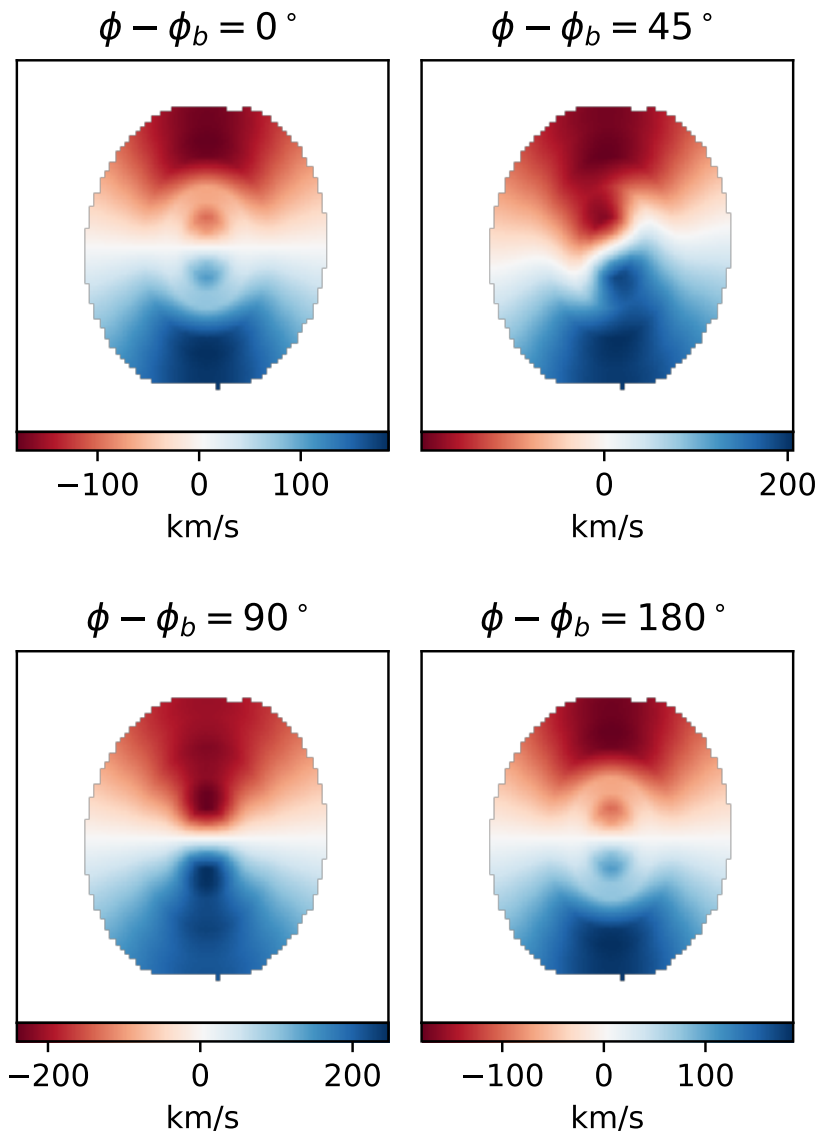

Figure 3.7: A comparison of different relative position angles between the dominant first-order and secondary bar component in model velocity fields. These mock galaxies are based off of the Nirvana rotation curves for MaNGA galaxy 8078-12703 with an inclination of 45°. For relative bar position angles that are not aligned with the major or minor axis, the bisymmetric motion creates clear distortions in the shapes of the isovelocity contours, allowing Nirvana to recognize the bisymmetric velocity component. However, for bars aligned or anti-aligned with the major or minor axis (in-plane angular difference of 0° or 90°), the isovelocity contours only change in magnitude rather than shape, an effect that can be modeled without a bisymmetric component. The 180° periodicity is also evident.

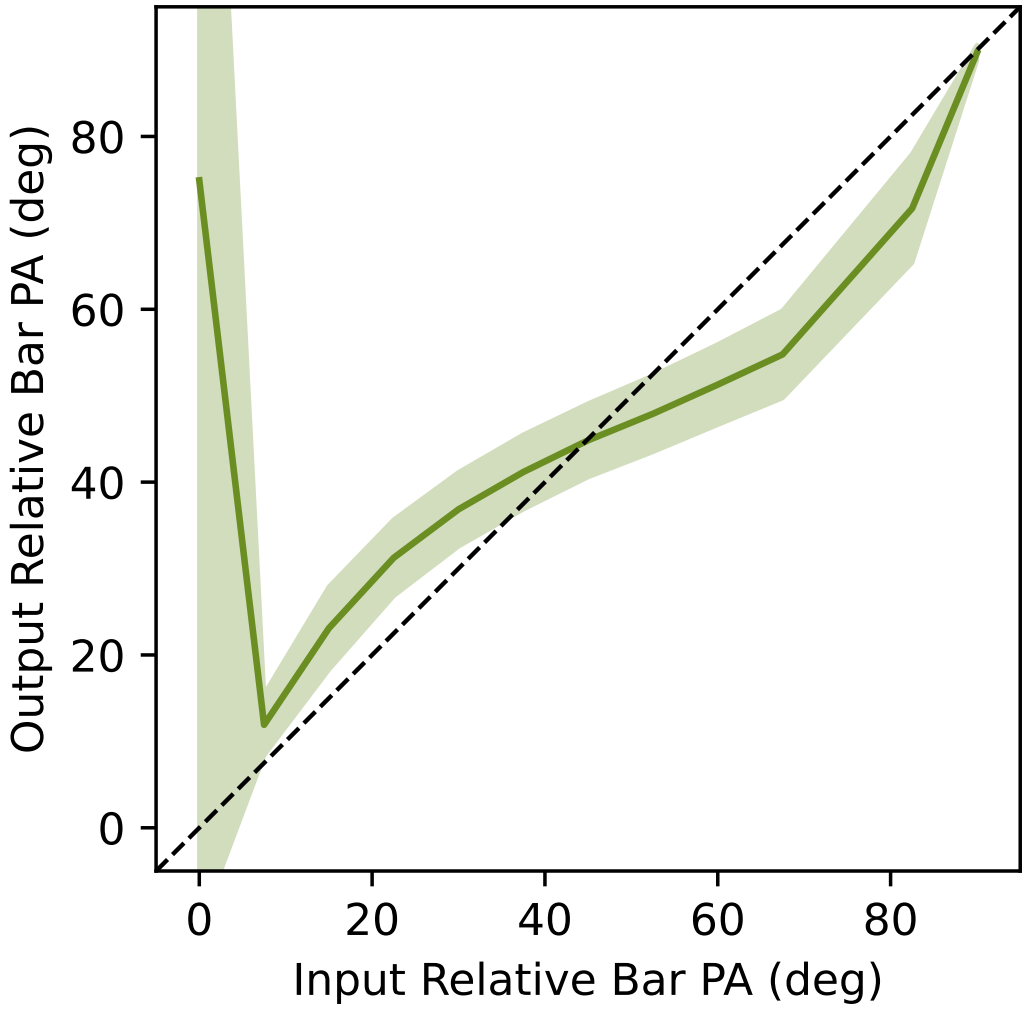

Figure 3.8: The recovered relative position angles and errors on posteriors from a set of mock galaxies similar to those shown in Figure 3.7 projected onto the plane of the sky. Relative position angles that are roughly 45° are recovered faithfully, but diagonal bars are always biased towards 45°, sometimes leading to biases over $5 - 10°$. Aligned and anti-aligned bars are difficult to distinguish in velocity data, leading to inflated or unrealistic errors on bisymmetric position angle, but they have no inherent bias.

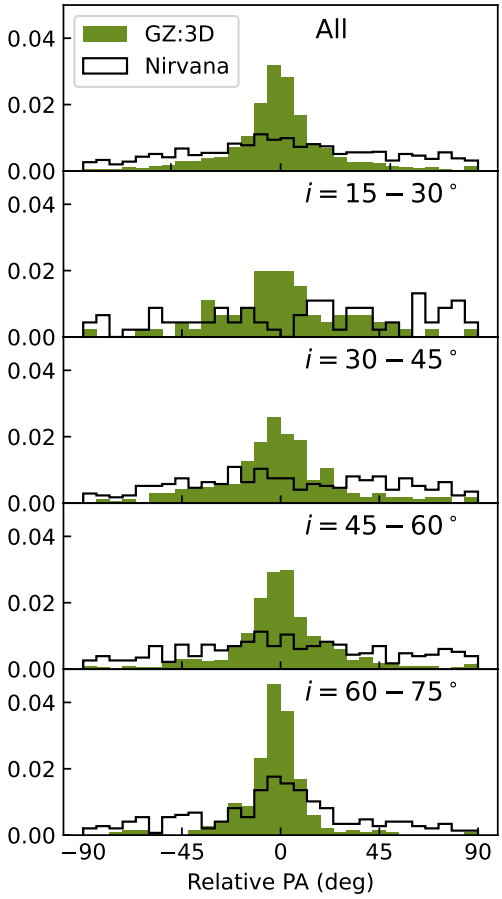

Figure 3.9: Histograms showing the distribution of on-sky relative position angles recovered by Nirvana and Galaxy Zoo:3D for the entire sample of barred galaxies (top) as well as broken down into inclination bins. Nirvana inherently biases towards bars that are at a 45° angle to the major axis because those bars cause larger kinematic asymmetries, but that small bias is overwhelmed by the large GZ:3D bias towards bars that are aligned with the major axis. This bias arises because they are not as distorted by projection effects and are thus easier for volunteers to identify. Both of these biases worsen with inclination.

stronger bisymmetric distortion than a more aligned one, Nirvana requires smaller second order velocity components to explain the same bisymmetric features in the velocity field. This minimizes the P_2 penalty in the likelihood outlined in Section 3.4.2, yielding a potentially more favorable outcome. However, when P_2 is turned off in the code, the bias still remains so this cannot be the explanation.

3.5.2 Comparison with imaging

In order to validate Nirvana's bar position angles, we compare our results to those of GZ:3D (Masters et al. 2021, see Section 3.2.3). Because GZ:3D treats each pixel individually, the GZ:3D bars are irregular in shape, making it difficult to define a bar position angle. We developed the following procedure (shown in figure 3.10) for finding a representative bar position angle for each galaxy. First, we use the votes as weights to find the weighted center of the bar mask, which we take to be the center of the bar. Next, we divide the image into on-sky azimuthal bins, adding up the bar votes within each bin to create an azimuthal distribution of bar votes. We then use a Savitzky-Golay smoothing filter to remove higher order noise from this distribution to obtain a more continuous curve. We then adjust the distribution so its maximum is in the center, yielding a smooth and approximately symmetrical distribution of bar votes. Finally, we calculate the weighted mean of the whole distribution, which gives us our final bar position angle that is robust to visual inspection and relatively resistant to irregular bar shapes and volunteer misclassifications. The process is summarized in Figure 3.10.

The GZ:3D sample displays a bias towards bars aligned with the major axis

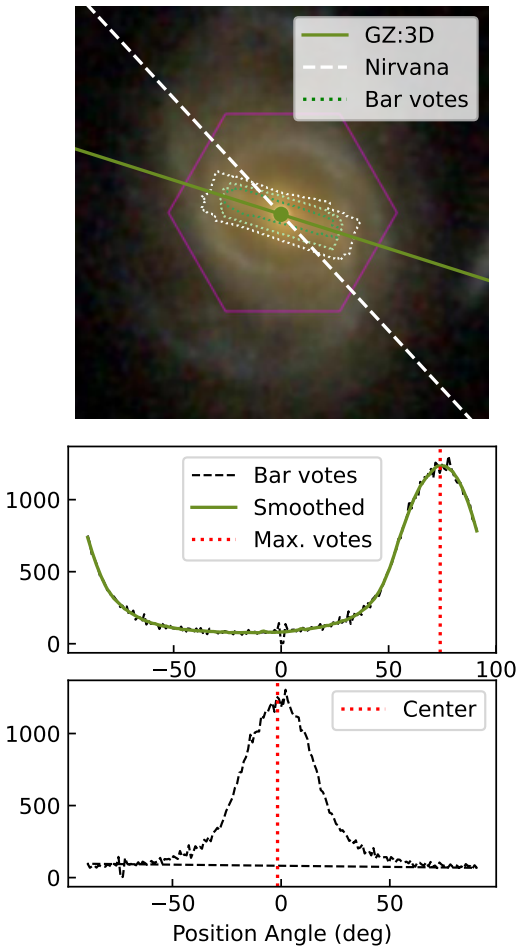

Figure 3.10: A set of subplots summarizing the method used to distill the GZ:3D bar classifications down to a single position angle for a galaxy. Top: The SDSS image of MaNGA galaxy 8078-12703 overlaid with the extent of the MaNGA IFU (magenta), the fraction of votes indicating the presence of a bar (dotted contours), the bisymmetric position angle from the Nirvana model (white dashed) and the GZ:3D bar position angle derived using this method (solid green). The weighted center of the bar votes is marked as a green circle. Middle: The number of GZ:3D bar votes from volunteers that fall into different azimuthal bins (black dashed) are smoothed to remove high-frequency noise (green) and the peak number of smoothed votes is used as a first approximation for the bar position angle (red dotted). Bottom: The azimuthal slices are recentered on this approximation (black dashed) and the weighted center of the peak is calculated (red dotted) to reduce the effect of asymmetric or bimodal peaks. This final position angle is used as the bar position angle in the top subplot. More examples can be seen in Figure 3.12.

that is present in the GZ:3D data set. Projection effects lead to a nonuniform distortion in azimuthal angles in high inclination galaxies, meaning that even a uniform distribution of on-sky bar angles will become biased towards major axis bars when transformed to in-plane coordinates. In addition, because bars along the minor axis are foreshortened due to projection effects, they can be difficult to distinguish from a bulge in inclined galaxies (Bureau & Freeman 1999; Binney & Tremaine 2008), leading to a likely underreporting of bars close to the minor axis by GZ:3D volunteers. These confounding factors lead to a significant overrepresentation of bars that are closely aligned with the major axis in the GZ:3D sample, which in turn introduces the same bias into the Nirvana-MaNGA sample. Thus, we find a drastic dearth of bars perpendicular to the major axis, especially at higher inclinations where projection effects are larger. This is seen in the solid green histograms in Figure 3.9. Though this bias is complementary to the Nirvana's bar position angle bias detailed in Section 3.5.1, we still find correspondence between the two bar classification techniques.

We find a little correspondence between the bar position angles between GZ:3D and the Nirvana-MaNGA barred sample overall. However, the correspondence is greater for galaxies with more bisymmetric motion. We define a subsample consisting of the 10% of Nirvana-MaNGA barred galaxies with the highest gas-phase V_{2r} values at 1/3 of their radius ($V_{2r} \gtrsim 50$ km/s). We choose this characteristic for constructing the subsample because 1) bars are associated with radial motions; and 2) the influence of bars greatly diminishes beyond corotation (Binney & Tremaine 2008), so we focus on the inner region of the galaxy. Galaxies in this subsample display a much tighter correspondence with

GZ:3D in bar position angle, and the remainder of the galaxies with comparatively small second-order motions show little correlation, as shown in Figure 3.11. Thus, we find that only a fraction of visually-identified galactic bars are accompanied by strong non-circular motions according to Nirvana.

Several visual examples of GZ:3D/Nirvana bar correspondence within the high-V_{2r} subsample are found in Figure 3.12.

3.5.3 Velocity components

Nirvana finds higher second-order velocity components on average in the sample of barred galaxies than in the controlled sample of unbarred galaxies, indicating that bars are indeed associated with second-order motions in some galaxies. This trend can be seen in Figure 3.13. The median V_{2r} magnitude measured at 1/3 of the Nirvana model's radius is significantly higher in the gas-phase velocity fields of barred galaxies, with the upper tail of the distribution extending significantly higher indicating a greater fraction of galaxies with larger non-circular motions. The difference is also present in the stellar velocity fields but the difference is not as large, indicating that bars have a lesser influence on stellar kinematics than gas kinematics.

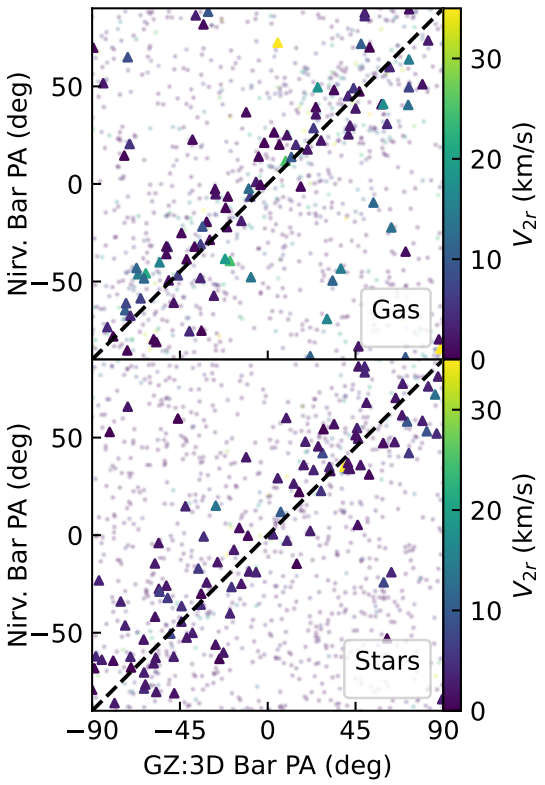

Figure 3.11: Comparisons between the bar position angles derived from Galaxy Zoo: 3D and the on-sky bisymmetric kinematic position angles derived from Nirvana for gas-phase (top) and stellar (bottom) velocity fields for barred galaxies in MaNGA. Our subsample of galaxies in top 10% of V_{2r} magnitude ($\gtrsim$ 50 km/s) at 1/3 of their radius (triangles) show a strong correspondence between kinematically-derived position angles for bisymmetric terms in Nirvana and the imaging-derived bar position angles from GZ:3D, while the Nirvana-MaNGA sample as a whole (circles) shows a weaker correspondence. This indicates that when Nirvana recovers significant second-order motions in a galaxy, it tends to agree with visual classifications on bar angle, although the correspondence is tighter for gas-phase velocity fields than for stellar velocity fields.

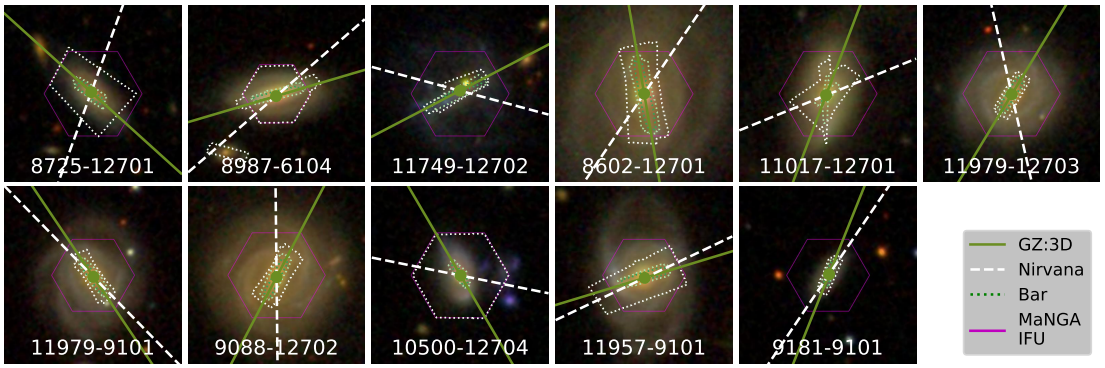

Figure 3.12: A random selection of SDSS images of Nirvana-MaNGA galaxies from the subsample with the highest V_{2r} magnitudes. Overlaid are the boundaries of the MaNGA IFU (magenta), the GZ:3D bar position angle (solid green), the Nirvana bisymmetric position angle (dashed white), the GZ:3D bar votes (dotted contours), and the MaNGA plate and IFU identifiers. Some galaxies show a tight correspondence between the visually-identified GZ bar and the kinematically-identified Nirvana bar, while others show a large difference.

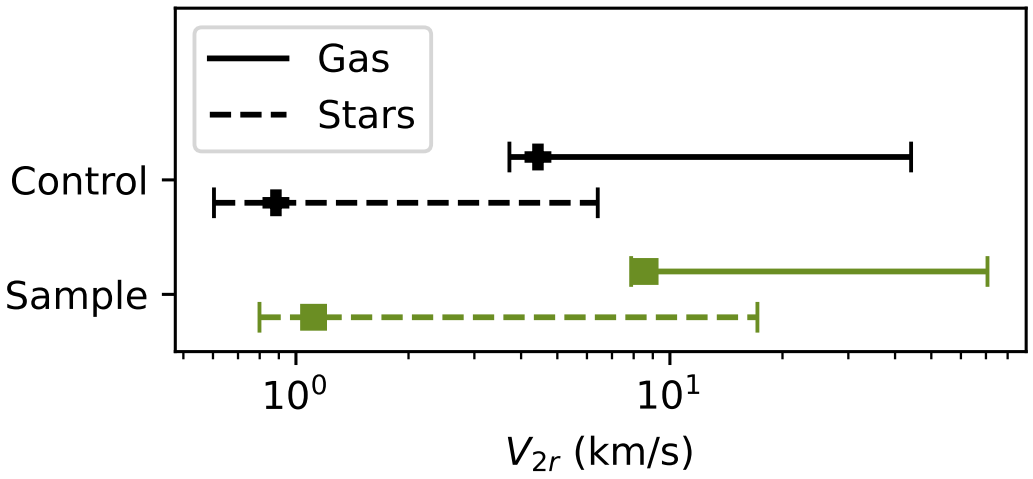

Figure 3.13: The distributions of the magnitudes of second-order radial velocity profiles at 1/3 the radius of the Nirvana models for both the Nirvana-MaNGA barred sample (green squares) and the control sample (black pluses). Medians and 68% intervals are marked for both gas-phase (solid lines) and stellar (dashed lines) velocity field models. There are significant differences in radial motions for both gas and stellar velocity fields, indicating that bars are indeed associated with non-circular motions, but the magnitude of the motions is much greater for gas than for stars.

3.6 Summary

The Nirvana software package is a Bayesian velocity field modeling code that can reliably fit both circular and bisymmetric motions in 2D kinematic data for spiral galaxies. We build on previous works (e.g. DiskFit, Spekkens & Sellwood 2007; Sellwood & Spekkens 2015), adding further capabilities for lower-spatial-resolution kinematic data like modeling velocity dispersion profiles and PSF convolution, and we use a Bayesian framework with physically-informed priors to improve the reliability of our results. We construct our Nirvana-MaNGA sample of over 1000 barred galaxies using the volunteer classifications of barred galaxies from the GalaxyZoo: 3D catalog, along with a control sample of MaNGA disk galaxies matched to the main sample in color, mass, effective radius, and axis ratio. The Nirvana model has been tested against real and mock data to produce reasonable and physically-motivated velocity field models for stellar and gas-phase kinematics in a wide variety of spiral galaxies by using custom prior and likelihood functions and sanitizing its own input data. The resultant models have only relatively small biases in inclination and bar position angle that we explore above.

Nirvana's on-sky second-order position angles show a correspondence with imaging-based bar angles from GZ:3D despite notable biases from projection effects, confirming a relationship between visually-identified bisymmetric structures and kinematic disturbances from non-circular motions. We also find that Nirvana reliably recovers more second-order velocity modes in barred galaxies than in unbarred galaxies, validating the dynamical properties of bars in the largest sample of real galaxies yet assembled. Nirvana finds significantly higher second-order velocity modes in gas-phase

velocity fields than in stellar velocity fields and finds no non-circular terms in many galaxies that would be visually classified as barred, warranting further investigation into the effects of bars on different kinematic components in galaxy centers.

Our spaxel-by-spaxel maps of non-circular motion magnitudes in MaNGA barred spirals allow further study of the influence of bars on other galaxy properties. It is possible to directly search for a correlation between elevated non-circular motions within bars and radial-mixing-driven flattening of stellar population gradients and other population differences in barred galaxies, as has been seen with existing visually-identified barred galaxy samples (e.g. Fraser-McKelvie et al. 2019, 2020; Krishnarao et al. 2020). Our physically-motivated measures of non-circular motions may also provide a new perspective on the influence of kinematic asymmetry on Tully-Fisher scatter (Bloom et al. 2017; Andersen & Bershady 2013), provide new methods for finding galactic inflows and outflows, allow for new estimations of asymmetries in dark matter halos (Sellwood & Sánchez 2010).

The Nirvana code can also easily be applied to other data sets as long as they have information on kinematics, surface brightness, and PSF. The Nirvana-MaNGA sample provides a comprehensive baseline of the kinematic properties of barred galaxies in the local Universe, so a sample of Nirvana models of more distant galaxies would allow for the study of the evolution of bar kinematics over the course of galactic evolution.

Chapter 4

Characterizing Stellar Population Gradients in Kinematically-Identified Bars

4.1 Introduction

Most present-day disk galaxies have a galactic bar (Masters et al. 2011; Nair & Abraham 2010) including the Milky Way (Blitz & Spergel 1991), a smooth linear bisymmetric morphological feature in the galactic center (Binney & Tremaine 2008). Bars appear to form from perturbations that cause instabilities in a disk galaxy's gravitational potential, as seen in gravitational potential simulations, n-body simulations, and hydrodynamical simulations (e.g. Toomre 1981; Sellwood & Wilkinson 1993; Rosas-Guevara et al. 2022), and they create linear resonances in stellar orbits (Athanassoula

2002) and redistribute angular momentum throughout the disk (Kormendy & Kennicutt 2004). Though studies disagree on whether the bar fraction decreases or remains steady with redshift (e.g. Melvin et al. 2014; Cameron et al. 2010; Sheth et al. 2008; Elmegreen et al. 2004), observation evidence shows evidence of bars at $z > 2$ (Guo et al. 2023a) and stable, long-lived bars in the local Universe (Seidel et al. 2016; Gadotti et al. 2015; Pérez et al. 2009).

Bars have been observed to correlate with many features in their host galaxies. Galaxies with visually-identified bars have stellar populations that are overall redder, older, and more metal-poor, with lower star formation rates and dust obscuration than comparable galaxies without bars (Fraser-McKelvie et al. 2020; Kruk et al. 2018). Bars may also be associated with quenching in the galactic core, with bars occurring more often in gas-poor galaxies (Masters et al. 2012), more H I holes (Newnham et al. 2020), and more LI(N)ER regions (Krishnarao et al. 2020), although these results are dependent on bar age since Yu et al. (2022) find elevated central molecular gas and star formation among galaxies with strong photometric bisymmetric distortions like bars, likely caused by gas inflows. Bars are also correlated with mergers or tidal disruptions in their hosts (Bi et al. 2022).

In addition to redistributing angular momentum and elongating stellar orbits, bars also channel gas radially inwards and outwards along their leading edge (Fragkoudi et al. 2016). This gas inflow may cause periods of significantly enhanced central star formation (Coelho & Gadotti 2011; Ellison et al. 2011), and has been observed to cause elevated star formation along the leading edge of the bar (Fraser-McKelvie et al. 2020).

These flows are predicted to lead to flattened gas-phase metallicity and stellar population gradients (Minchev & Famaey 2010; Friedli et al. 1994), and these predictions have been borne out in long-slit spectroscopy across the bar major axis (Sánchez-Blázquez et al. 2011) and across boxy-peanut bulges that are associated with bars in edge-on disks (Williams et al. 2012).

However, to fully understand the effects of a bar's nonaxisymmetric motions on the entirety of the surrounding disk, full two-dimensional spectroscopy is required. Simulations (e.g. Di Matteo et al. 2013; Kubryk et al. 2013) find both radial and azimuthal metallicity variations caused by the dynamical disruption of bars. Observational studies with spatially-resolved spectroscopy confirm this as well, with Seidel et al. (2016) finding flattened iron and magnesium gradients along the bar axis using a sample of 16 galaxies using the SAURON integral field unit (IFU). In addition, Fraser-McKelvie et al. (2019) used a partial sample from the MaNGA survey and morphological classifications from GalaxyZoo: 3D to compare bars with their surrounding disks, finding shallower age and metallicity gradients along the bar axis.

However, despite studying an inherently kinematical phenomenon, all of these previous studies use visual classification to identify their bars. This chapter seeks to build on previous work in two ways. First, we utilize the final data release of SDSS-IV MaNGA to work with the largest sample of 2D kinematic models of bars yet assembled. Second, we base our bar identifications on the Nirvana-MaNGA sample (Chapter 3), which uses a Bayesian forward model based on the nonaxisymmetric kinematic model from Spekkens & Sellwood (2007) to decompose MaNGA galaxy rotation data into

separate rotational modes, enabling the isolation of bisymmetric modes tied to bars. Rather than relying on visual assessments of bar strength as tracers for radial motions, we use kinematic models to directly quantify radial motions, providing the first large-scale direct test of the relationship between bar bisymmetric motions and flattening of stellar population gradients. Even while determining bar and disk regions independent of imaging, we find flattened stellar age and metallicity gradients in agreement with previous studies.

This chapter is structured as follows: Section 4.2 details the data and methodology of the MaNGA survey and the Nirvana-MaNGA sample. Section 4.3 outlines the determination of dynamical regions in the galaxies, and Section 4.4 gives our procedure for calculating population gradients. We detail our results in Section 4.5 before summarizing and looking forward in Section 4.6.

4.2 Data

4.2.1 MaNGA: Mapping Nearby Galaxies at Apache Point Observatory

This chapter relies on data and data products from the seventeenth data release of the Sloan Digital Sky Survey IV (SDSS-IV DR17; York et al. 2000; Blanton et al. 2017; Abdurro'uf et al. 2022) and the Mapping Nearby Galaxies at Apache Point Observatory survey (MaNGA Bundy et al. 2015). MaNGA collected spatially-resolved spectra for ∼10,000 galaxies using the BOSS spectrographs on the 2.5 m telescope at Apache Point Observatory (Gunn et al. 2006), with each IFU being a bundle of optic fibers grouped

into hexagonal bundles of 19 to 127 fibers that are 12" to 32" in diameter (Drory et al. 2015). Spectral observations have a resolution of $R \sim 2000$ over a range of 3600 Å$< \lambda <$ 10300 Å, and exposure times were varied to achieve the target signal-to-noise ratio (SNR) of 10 in the g-band (Bundy et al. 2015). Simultaneous observations of standard stars and sky within the same field allowed for flux calibration and sky subtraction in the observed spectra(Yan et al. 2016). The point-spread function (PSF) for MaNGA data cubes have a median full-width half-maximum (FWHM) of 2.5", which roughly corresponds to kiloparsec scales at the targeted redshifts ($z < 0.15$), though observations are dithered and interpolated onto a 0.5" grid of spaxels.

The MaNGA sample on the whole was selected to be uniform over i-band absolute magnitude. It is divided into two subsamples: the Primary+ sample ($\sim$2/3 of the total sample) with galaxies with spectral coverage out to $\sim$1.5 effective radii (R_e), and the Secondary sample ($\sim$1/3 of the total sample) with observations extend out to $\sim$2.5 R_e (Wake et al. 2017). The raw spectroscopic observations are reduced by the MaNGA Data Reduction Pipeline (DRP; Law et al. 2016), with the Data Analysis Pipeline (Westfall et al. 2019; Belfiore et al. 2019) producing data products such as velocity measurements. DR17 is the final data release of the MaNGA survey, containing MaNGA observations and data products from 10,010 unique galaxies, and all photometric data used in this chapter is from the NASA-Sloan Atlas (NSA; Blanton et al. 2011), which uses imaging from SDSS-I, II, and III.

The data in this chapter use a hybrid binning scheme data products from the DAP that has different stellar- and gas-phase line-of-sight velocity measurement

methodology. Spaxels in stellar kinematic measurements are Voronoi binned (Cappellari & Copin 2003) to a threshold g-band-weighted SNR of at least 10, but gas kinematics are determined on a spaxel-by-spaxel basis. All ionized gas tracers are assumed to have the same velocity, so when we discuss kinematic information derived from observations of nebular emission in the remainder of the paper, we refer to them only as "gas-phase" velocity fields rather than as being associated with a particular emission line. However, each emission line is fit independently for flux and velocity dispersion, so we are able to use individual emission line fluxes. Spaxel-by-spaxel spectral indices are calculated according to the methodology laid out in Worthey et al. (1994), Trager et al. (1998), Burstein et al. (1984), and Faber et al. (1985).

4.2.2 Nirvana: Nonaxisymmetric Irregular Rotational Velocity Analysis

Nirvana is a velocity field fitting code detailed in Chapter 3 that is capable of modeling first- and second-order rotational modes in 2D velocity data. Before modeling the input galaxy, Nirvana applies a number of cuts and filters to prepare the data and assess its suitability for modeling. It removes spaxels with erroneously outlying velocity and velocity dispersion measurements, spaxels with low SNR, spaxels which deviate too greatly from a one-component kinematic model of the data, and large Voronoi bins with poorly-defined centers.

The galaxy is then decomposed into a series of in-plane annular bands. The on-sky spaxel coordinates are projected using the inclination and position angle derived from a basic axisymmetric model (see Westfall et al. in prep.), and the widths of the

annuli are chosen to Nyquist sample the MaNGA PSF along the galaxy's minor axis. Any annuli that has more than 75% of its spaxels masked are removed. If fewer than 20% of the original data remains at the end of these cuts or if the galaxy has fewer than 3 annuli, the galaxy is deemed to be unsuitable for fitting and is discarded. More detailed descriptions of these cuts can be found in Chapter 3.

Nirvana then decomposes the spatially-resolved galaxy kinematics into a set of three non-parametric rotation curves using a model based on Spekkens & Sellwood (2007):

$$\begin{aligned} V(r,\theta) &= V_{sys} + \sin i \Big[V_t(r) \cos\theta \\ &\quad - V_{2t}(r) \cos\big(2(\theta-\phi_b)\big) \cos\theta \\ &\quad - V_{2r}(r) \sin\big(2(\theta-\phi_b)\big) \sin\theta \Big]. \end{aligned} \tag{4.1}$$

The model is defined on the in-plane polar coordinates r and θ, which are projected on-sky with an inclination i and a position angle ϕ. The rotational velocity components V_t, V_{2t}, and V_{2r} are defined at edges of each of the annuli, interpolating for values in between. V_t represents the first-order tangential rotational mode, while V_{2t} and V_{2r} are the second-order tangential and radial modes respectively, with twice the angular frequency. All velocity components share the same inclination, position angle, and center, but the second-order components are offset from the first-order by a position angle ϕ_b.

Velocity dispersion is modeled with a radially-symmetric piece-wise model defined on the same annuli, and the velocity, velocity dispersion, and surface brightness

are used to simulate PSF smearing on the model.

The galaxy kinematics are then fit using the Bayesian modeling code `dynesty` (Speagle 2020), a Python package implementing nested sampling (Skilling 2004, 2006) with multi-ellipsoid bounds (Feroz et al. 2009). Priors are largely uninformed except for the inclination which is tied to the NSA-derived photometric inclination with a Gaussian prior with a 3° standard deviation. Nirvana uses a standard Gaussian likelihood for both the velocity and velocity dispersion models, with added penalties to encourage smooth rotation curves and discourage overzealous use of the second-order terms. Further information on the performance and biases of the Nirvana model are given in Chapter 3.

4.2.3 Nirvana-MaNGA Sample

The kinematic models used in this chapter are from the Nirvana-MaNGA sample, a group of 1263 barred MaNGA galaxies which have Nirvana models for either the stellar or gas-phase velocity fields. These galaxies were selected using GalaxyZoo: 3D (GZ:3D Masters et al. 2021), which used volunteer classifications to designate regions of galaxies that appeared to be bars. Of the 1263 unique galaxies, 973 have stellar velocity field models, 1012 have gas-phase velocity field models, and 722 galaxies have both stellar and gas velocity models.

Biases in the GZ:3D sample of barred MaNGA galaxies and the Nirvana data clipping algorithm lead to the vast majority of the sample being in the "blue cloud" of galaxies on a standard color-magnitude diagram (see Figure 1 of Chapter 3). A majority of the sample lies between $10^9 - 10^{11} M_\odot$ according to NSA elliptical Petrosian

photometry, with a bias towards the high-mass end of the distribution.

The Nirvana-MaNGA dataset also includes a control sample of galaxies matched one-to-one with the main sample. These galaxies are unbarred according to GZ:3D are selected to match as closely as possible in mass, color, effective radius, and axis ratio, and they have nearly identical population statistics as the main sample.

Nirvana finds stronger bisymmetric motions on average in the main sample than in the control, indicating that bars are indeed tied to bisymmetric motions on the whole, although not all galaxies with visually-identified bars have large second-order terms in their kinematic models. To focus specifically on the galaxies with the highest levels of bisymmetric motion, we define a subsample of galaxies which are in the top 10% of second-order velocity at 1/3 of the radius of their largest valid annulus. For these galaxies with strong bisymmetric motions, Nirvana agrees well with GZ:3D on bar position angle.

More details on sample construction, composition, and properties can be found in Chapter 3.

4.3 Nirvana Bar Regions

In order to study the effects of radial mixing in bars on stellar populations, we must first define the the regions of galaxies affected by these motions. Unlike past studies which relied on visually-identified bars to mark regions of high expected radial mixing, the Nirvana-MaNGA sample allows us to directly quantify the bisymmetric motions in each spaxel, giving a precise picture of the galactic regions that should be

most impacted by the bar.

For each of the barred galaxies in the gas-phase Nirvana-MaNGA sample, we construct a set of masks to isolate the bar, inner disk, center, and outer disk regions similar to those used in Fraser-McKelvie et al. (2019). We define the bar axis as a linear region surrounding the gas-phase on-sky bar position angle ϕ_b', and the bar radius as the maximum radius at which the normalized second-order velocities V_{norm} are greater than its mean value across all annular bins, with V_{norm} defined as

$$V_{norm} = \frac{\sqrt{V_{2t}^2 + V_{2r}^2}}{V_t} = \frac{V_2}{V_t}. \tag{4.2}$$

The numerator of V_{norm}, which we call V_2, is defined as such because it represents the resulting amplitude of a wave created by combining two sine waves with a phase offset of 90°. These velocity values are only defined by the Nirvana model at the edges of each annulus, but are interpolated in between to create a smooth distribution across all radii to give a more accurate bar radius.

The inner disk mask is defined as all spaxels that are at in-plane radii less than the bar radius but are not part of the bar. The center mask is defined as all spaxels with in-plane radii less than that of the innermost inner disk spaxel, and the bar mask is defined as all spaxels within 2" of the bar axis that are not in the center. The outer disk is all remaining spaxels outside of the bar radius. A visualization of these different divisions is shown in Figure 4.1.

These masks show modest agreement with visual bar classifications. As recommended by Masters et al. (2021) and Krishnarao et al. (2020), we identify a given

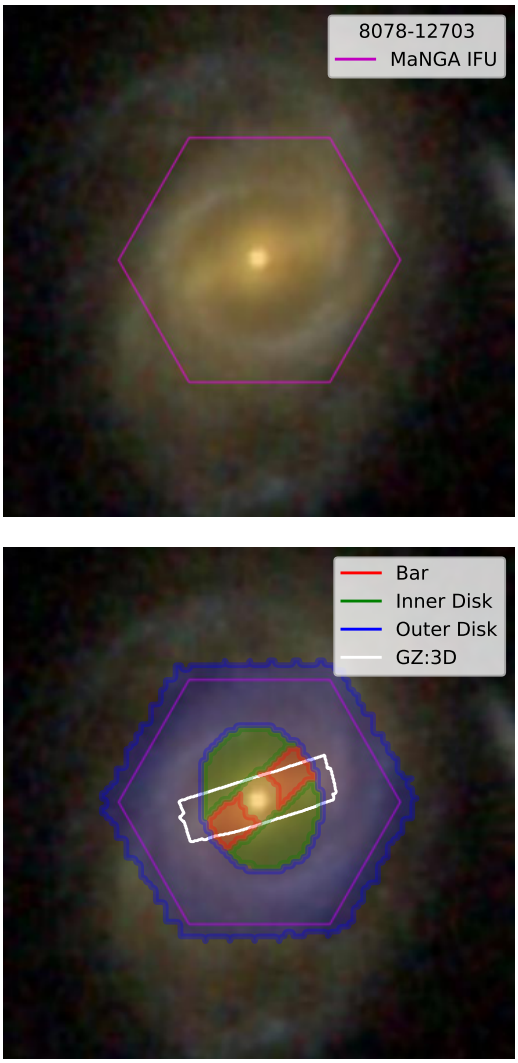

Figure 4.1: An overlay showing how the kinematically-derived masks compare with SDSS imaging for barred MaNGA galaxy 8078-12703. The bar is shown in the red outlined region, inner disk in green, and outer disk in blue. The white contour shows the region marked as a bar by 20% of GZ:3D respondants, and the magenta hexagon shows the rough outline of the MaNGA IFU.

spaxel as part of a bar if more than 20% of GZ:3D volunteers classified it as inside the bar. Galaxies in the Nirvana-MaNGA sample often display different bar radii than the visually-identified bars, indicating that kinematic behavior may not always be tied to visual morphology or that a more robust bar length definition is needed, but on the whole the on-sky bar position angles are comparable (see Figure 11 of Chapter 3).

4.4 Stellar Population Gradients

In addition to the velocity, velocity dispersion, and surface brightness maps used by Nirvana, the MaNGA DAP also produces spaxel-by-spaxel maps of spectral indices. The method by which these are produced is described further in Section 4.2.1. In this section, we use these spectral index maps to trace the gradients of various stellar population parameters as a function of radius.

To define a gradient, we roughly follow the methodology of Fraser-McKelvie et al. (2019) by first dividing the galaxy into a series of annuli with widths of 0.5", projecting the annuli on-sky using the best-fit inclination and position angles from the Nirvana-MaNGA models of each galaxy. We then compute the weighted average of each of the unmasked spaxels in each bin, using the inverse variances reported by the DAP to calculate the weights, and we use the standard deviation of spectral index measurements as the error on the average. We then use a Levenberg-Marquardt least-squares optimizer (Moré 1978; Virtanen et al. 2020) to fit a line to the binned measurements, using the slope of that line as the gradient of the data. An example of this method is shown in Figure 4.2.

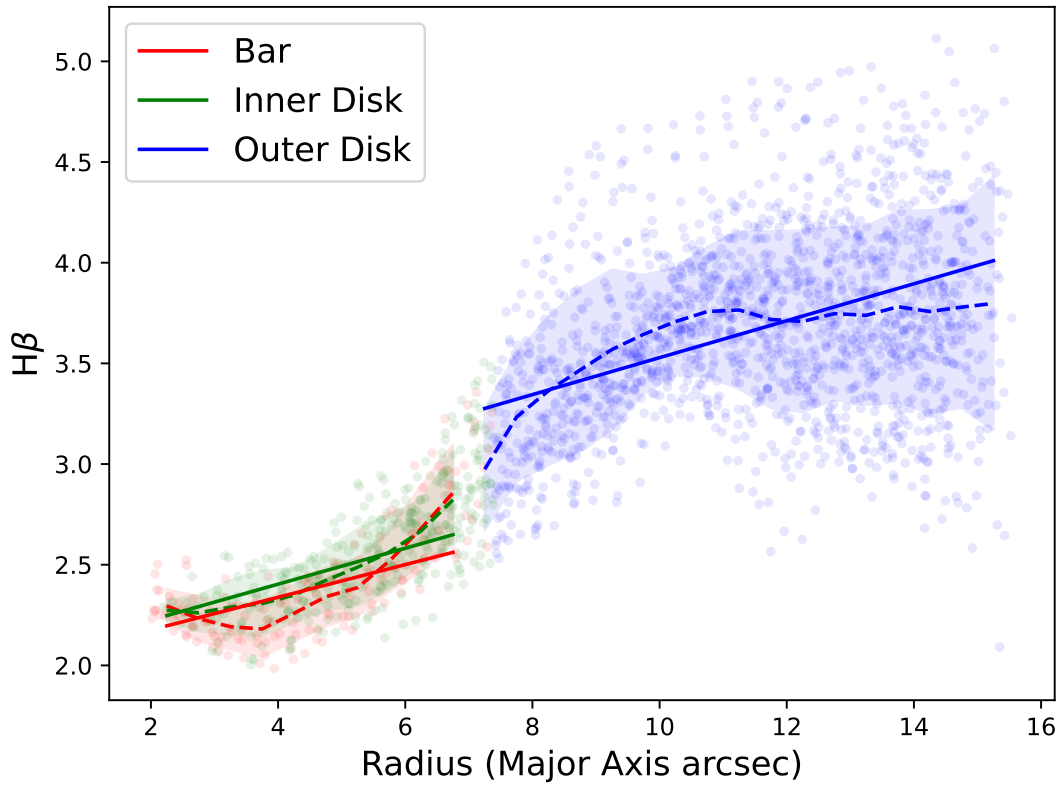

Figure 4.2: An example of the stellar population gradient fitting process for the same galaxy as was shown in Figure 4.1. Points show the values of the Hβ spectral index, with their color indicating which region of the galaxy they are in (bar in red, inner disk in green, outer disk in blue). Dashed lines show the median $H\beta$ values in each 0.5" radial bin, with the shaded regions indicating the 1σ spread within each bin. The solid lines show the best fit gradient to each set of binned values.

We use Hβ as stellar age indicators and MgFe, as defined by

$$\mathrm{MgFe} = \sqrt{(\mathrm{Mg}b(0.72 \times \mathrm{Fe5270} + 0.28 \times \mathrm{Fe5335})}, \tag{4.3}$$

as a stellar metallicity indicator, both of which are largely insensitive to α/Fe ratio changes (González 1993; Fraser-McKelvie et al. 2019). In addition, we use D_n4000 as another stellar age indicator.

4.5 Results

Using the methods described in the previous section, we calculate gradients for the different stellar population tracers for all galaxies with successful gas-phase Nirvana models in the Nirvana-MaNGA sample in both their bar and inner disk regions, separating out the galaxies that fall in our subsample of the top 10% of V_2 values. We then compare the stellar population gradients for the two regions for each galaxy, looking for trends across the population by fitting a line using the Bayesian forward modeling code `emcee` (Foreman-Mackey et al. 2013). We put a floor of 10^{-2} on gradient errors to prevent unreasonably precise fits from having an outsized effect on the model. The main results are summarized in Figure 4.3.

We find that for each of the stellar population parameters, the gradients in barred regions tend to be shallower than the gradients in the inner disk regions, supporting the conclusion that the radial motions within bars flatten stellar population gradients compared to their surrounding disks. The correlation for D_n4000 is highest, as represented by the Pearson R coefficient, with other parameters showing notably

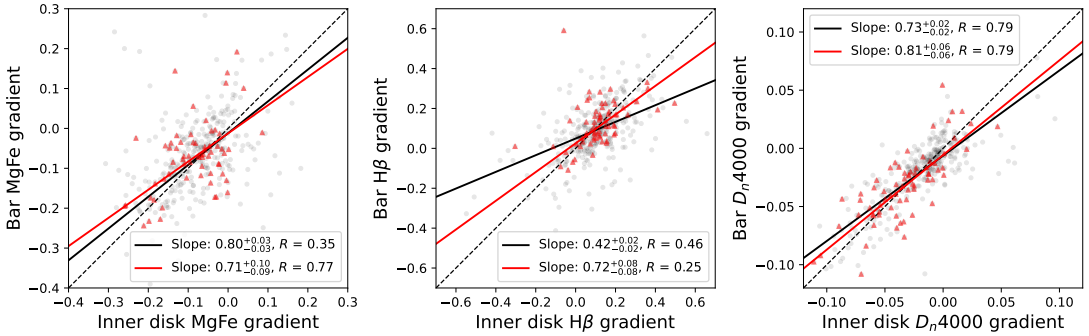

Figure 4.3: Comparisons between various stellar population parameters in kinematically-identified bar regions (x axis) and in the surrounding disk regions (y axis) for the metallicity tracer MgFe (left) and the stellar age tracers Hβ and D_n4000 (middle and right), with black points and lines showing the entirety of the Nirvana-MaNGA gas-phase sample and the red showing our subsample of the 10% of galaxies with the highest second-order terms. All gradients show slopes shallower than one-to-one, indicating shallower stellar population gradients in bar regions than in the surrounding disk, but only Hβ shows a large change from higher second-order velocities. The Pearson R coefficient shows the strength of the correlations, with $Dn4000$ being the strongest.

weaker correlations. This kinematically-derived result agrees with the imaging-based conclusions of Fraser-McKelvie et al. (2019).

We also find that increased second-order velocity motions in Nirvana models largely do not affect the slopes of stellar metallicity gradients. The red triangles and lines in Figure 4.3 show the galaxies in our high V_2 subsample and their best-fit lines, which is indistinguishable from the best-fit line for the whole sample for MgFe gradients, meaning that the increased mixing has no effect on metallicity gradients. However, the two stellar age indicators Hβ and D_n4000 have conflicting results, with Hβ showing a large difference in slope with increased second-order motions while D_n4000 is largely unaffected. We thus conclude that increased mixing has an uncertain effect on stellar age gradients.

These conclusions are supported by directly investigating the relationship be-

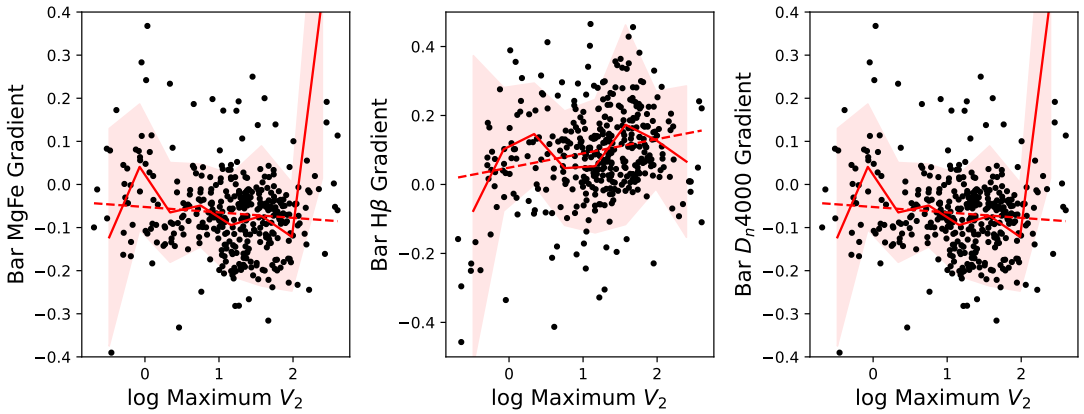

Figure 4.4: Relationships between peak second-order velocities V_2 and various stellar population tracers (MgFe on the left, Hβ in the middle, and D_n4000 on the right. All show a trend with increasing peak V_2, with MgFe and D_n4000 trending downwards while Hβ trends upwards. This indicates mixed results between the relationship between radial mixing and stellar age.

tween these stellar population tracers and the maximum value of the second-order velocity components found by Nirvana, as seen in Figure 4.4. Each of the tracers we use shows a trend for varying peak V_2 values, with MgFe and D_n4000 gradient slope trending downwards with increasing velocity and Hβ trending upwards. This again shows a mixed picture for the relationship between stellar age and radial mixing while supporting a flattening of metallicity gradients.

Though we cannot conclusively link elevated V_2 levels to shallower stellar population gradients, the shallower gradients in the overall sample still validate the conclusion that bisymmetric motions caused by bars smooth out stellar populations along the bar radius. Our bar masks are entirely kinematics-based and do not consider visual bar strength, yet we arrive at the same conclusion as previous works without having to assume that visual bars are directly tied to radial motions.

4.6 Summary

Using the largest sample of kinematic models of barred galaxies yet assembled, we investigate the connection between stellar population gradients and bar-driven radial motions more directly than previous studies. We use the Nirvana-MaNGA sample detailed in Chapter 3 to classify which regions of galaxies are associated with bars and which are associated with the inner and outer disk in order to directly tie radial measurements of stellar populations to kinematic behavior. Using 2D maps of MgFe, Hβ, and D_n4000, we find that kinematically-identified bar regions have lower stellar age and metallicity gradients than disk regions at the same radii, which agrees with previous studies based on visual bar identification (e.g. Fraser-McKelvie et al. 2019; Seidel et al. 2016; Sánchez-Blázquez et al. 2011; Williams et al. 2012) and simulations (e.g. Di Matteo et al. 2013; Kubryk et al. 2013; Minchev & Famaey 2010; Friedli et al. 1994). Though we do not see a clear relationship between high second-order velocity terms and shallow gradients, it is evident that stellar population gradients are flattened along the bar axis so bisymmetric kinematics must play a role.

Further study on this topic has the possibility of clarifying some limitations of the analysis of this paper. First, a more robust kinematic heuristic for bar length and width would allow Nirvana-identified bars, allowing for more precise discrimination between the bar and the surrounding disk and a more accurate determination of their stellar population properties. A more detailed analysis of stellar populations beyond basic spectral indices (e.g. with the full spectral fitting code Starlight, as in Fraser-McKelvie et al. 2019) could also enable more precise understanding of stellar age and

star-formation history along the bar. This would allow for comparisons with studies that found star formation quenching in bars (Krishnarao et al. 2020) and variation in metallicity gradients based on bar age (Yu et al. 2022). The extra dimension of kinematics that the Nirvana-MaNGA sample adds to barred galaxy stellar population studies opens up many possibilities to understand radial mixing more directly.

Chapter 5

Summary and Future Studies

5.1 Summary

This dissertation examined how kinematic models that accurately represent nonaxisymmetries in velocity fields are able to extract additional astrophysical information from the systems they describe compared to simpler models. Without consideration for how these added asymmetric features affect the overall characteristics of kinematic data, these irregular features will be glossed over by velocity field models and their information will be lost.

Chapter 1 gave a historical background on the history of the study of galaxy kinematics, from early observations on the nature of galaxy rotation itself, to characterizations of galaxy rotation curve flattening, to models for describing modern 2D velocity fields and their asymmetries. Many different modifications have been made to the simple rotating thin disk model to suit the purposes of the scientific question being asked, whether it was using rotation curves motivated by halo mass profiles to obtain

dynamical measurements, describing all galaxies in one "universal" parameter space, or more accurately accounting for the components of the disk that were not so simple.

Chapter 2 details one such modification to the thin disk model. By adding consideration for lensing shear to a Bayesian velocity field model, we were able to characterize the effects of gravitational lensing on the velocity field of mock observations, a practice called kinematic weak lensing (KWL). Chapter 2 improves on previous KWL models by simultaneously considering both kinematic and photometric manifestations of lensing, fitting the lensing shear in the velocity fields while also considering their mismatch with position angle measurements derived from imaging. This added information significantly increased the precision of our fit posteriors and broke degeneracies between shear and other fit parameters, allowing for an increase in signal-to-noise of up to a factor of six for mock observations.

Chapter 3 describes the creation of the Nirvana-MaNGA sample, the largest sample yet assembled of bisymmetric models of barred galaxy velocity fields. Additional velocity terms in the thin disk model are able to describe second-order rotational modes present in galaxy bars, and the Nirvana velocity field fitting code goes further than previous works by incorporating this model into a flexible Bayesian framework that is able to characterize a wide range of galaxies with minimal supervision. We apply Nirvana to a sample of barred galaxies in MaNGA, yielding $\sim$1000 models of barred galaxies, which generally show elevated bisymmetric velocity components compared to a matched control sample and which show agreement with visual classifications of bars.

Chapter 4 is the first application of the Nirvana-MaNGA dataset, using its

classifications of bar position angles and bisymmetric velocity components to investigate stellar populations in bars and their surrounding disks. Past observational studies show that stellar age and metallicity gradients are flattened along the visual bar axis as compared to their surrounding disk, and dynamical simulations predict that radial mixing along bars is responsible. The Nirvana-MaNGA sample enables the first direct test of this dynamical theory, showing that kinematically-identified bars have shallower population gradients than their surrounding disks and linking increased second-order velocities to changes in population gradients. This is the first direct and explicit kinematical linking of bars' noncircular motions to changes in stellar population gradients in a large sample.

5.2 Future Work

The work contained in this dissertation opens up a number of further lines of inquiry that I plan to address in the coming years.

5.2.1 Effects of Bars on KWL Errors

Gurri et al. (2021) studies the systematic errors that influence KWL measurements, pointing out an obvious area for synergy between the two major projects in this dissertation: large kinematic and morphological features in disks have the potential to disrupt KWL measurements. The shear posterior in KWL models, including that of Gurri et al. (2020) and our own detailed in Chapter 2, is highly sensitive to the position angle of the disk, and large kinematic features like bars or warps often create distortions

in velocity fields that can appear to be a change in disk position angle to a model that is not equipped to account for them. These biased position angles could lead to spurious KWL measurements, a phenomenon Gurri et al. (2021) calls "shape noise."

By leveraging what we now know about noncircular motions in barred galaxies from the Nirvana-MaNGA sample, it is possible to quantify the effects of this shape noise on our KWL measurements. By replacing the velocity fields in our mock galaxy observations in Chapter 2 with Nirvana-MaNGA velocity fields from Chapter 3, it will be possible to directly measure how bars affect KWL measurements. The Nirvana model allows for us to create disk galaxies with and without bisymmetric features from bars, providing an opportunity to study the effect of adding a bar to a KWL measurement in a controlled environment. This would improve our understanding of KWL errors on more realistic galaxies to inform potential future observing programs.

5.2.2 KWL Pilot Study

Chapter 2 suggests that a KWL-based cluster mass measurement is possible with only a relatively small number of velocity fields for moderate redshift background galaxies. Such observations are difficult to come by because background source density is relatively low and the resolved spectroscopic measurements necessary to construct a velocity field are expensive in terms of telescope time.

However, a small number of suitable data sets that fulfill these criteria already exist. For example, Mahler et al. (2018) presents a deep spectroscopic observation of Abell 2744, a strong lensing cluster at $z \sim 3$ using the MUSE wide-field IFU (Bacon et al. 2010). They observed a $2' \times 2'$ area that already has high-quality Hubble Frontier

Field photometry for a total of 18.5 hours on-sky, resulting in a data cube that captures detailed spectroscopic observations for background galaxies. The size and redshift ranges of these background galaxies are similar to the populations explored in Chapter 2, meaning our analysis techniques should be easily transferable.

Preliminary work on extracting kinematic information from this data set has largely been successful. By applying a modified version of the MaNGA DAP to the data cubes, velocity fields were able to be extracted for ∼100 background galaxies. However, more work is needed in to extend our methods to be able to extract kinematic information from several galaxies simultaneously. Our Bayesian framework lends itself well to a hierarchical model that combines shear information for many galaxies into one cluster mass measurement, so a simultaneous KWL fit may of many background galaxies may be able to provide an independent halo mass determination for the system.

5.2.3 Additional Effects of Bars on Stellar Populations and Kinematics

Chapter 4 represents an initial foray into using the Nirvana-MaNGA sample to probe the effects of bars on their host galaxies, but there are numerous other areas in this category worthy of scientific consideration. For example, recent studies of visually-identified barred galaxies in MaNGA show a correlation between the presence of a bar and galaxy color, dust, metallicity, BPT classification, and age (Fraser-McKelvie et al. 2020; Krishnarao et al. 2020), and other studies have shown links to star formation history central gas concentration (Kruk et al. 2018; Yu et al. 2022). Similar to Chapter 4's independent verification of stellar population gradients using bisymmetric kinematics rather than visual bars, it would also be valuable to directly link these observed galaxy

characteristics to their kinematics.

There are also a number of other lines of study relating bars to kinematics. A number of studies (e.g. Bloom et al. 2017; Andersen & Bershady 2013) have found correlations between galaxy asymmetry and scatter from the TFR, so a detailed study of asymptotic rotation speeds for barred galaxies using the Nirvana-MaNGA sample could determine whether these results are due to properties of the disk or assumptions in kinematic modeling. The Nirvana-MaNGA sample also has a large number of non-parametric second-order rotation curves for central bars, enabling an empirical study to determine a suitable physics-based parametric model for bar rotation curves. Such a model should be rooted in dynamical models for noncircular bar motions so it could give insight on the shape of the bisymmetric potential perturbation in the galaxy's mass distribution.

5.2.4 Modifications to the Nirvana Model

Nirvana was built specifically to describe noncircular motions in barred MaNGA galaxies using a nonparametric bisymmetric velocity field model, but its underlying framework is flexible enough to be adapted to other uses. For instance, were a parametric model like the one mentioned above to be developed, it could be incorporated into the Nirvana framework and, along with a parametric first-order rotation curve model, be used to fit the same sample of barred galaxies. Such a model would greatly reduce the complexity of the model and the time taken to fit a galaxy and potentially lead to easier physical characterization of the barred galaxy sample.

It is also trivial to modify the Nirvana kinematic model to fit first-order radial

inflows and outflows. In Chapter 3, we assumed that the galaxies in the sample had no significant mass inflows or outflows, but weak active galactic nuclei-drive gas outflows called "red geysers" have been found in MaNGA spectroscopic studies (Cheung et al. 2016; Roy et al. 2021). Spekkens & Sellwood (2007) explored using a first-order radial term rather than second-order velocity terms in their kinematic models, so the Nirvana model could easily be replaced with one that is capable of describing these gas outflows in existing red geyser samples and potentially finding as-yet undiscovered kinematic signatures of other inflows or outflows in MaNGA data.

The Nirvana framework is also flexible enough to take in data from other sources besides MaNGA. Any 2D velocity field with information on the spaxel coordinates, PSF, surface brightness, and velocity dispersion should be suitable for modelling, which includes data from many types of instruments. For instance, JWST has found evidence of mature bars as far as $z > 2$ (Guo et al. 2023b), and ALMA has observed velocity fields as far as $z > 9$ (Tokuoka et al. 2022), so the potential to study changes in bar kinematics over cosmic time is obvious. Visual IFU measurements at greater redshifts than the MaNGA sample, such as the aforementioned MUSE data or observations from the upcoming FOBOS (Bundy et al. 2019), also provide opportunities to study bars beyond the regime represented in the Nirvana-MaNGA sample.

Bibliography

Abdurro'uf, Accetta, K., Aerts, C., et al. 2022, ApJS, 259, 35

Aihara, H., Arimoto, N., Armstrong, R., et al. 2018, PASJ, 70, S4

Andersen, D. R., & Bershady, M. A. 2013, ApJ, 768, 41

Argyle, E. 1965, ApJ, 141, 750

Astropy Collaboration, Robitaille, T. P., Tollerud, E. J., et al. 2013, A&A, 558, A33

Astropy Collaboration, Price-Whelan, A. M., Sipőcz, B. M., et al. 2018, AJ, 156, 123

Athanassoula, E. 2002, ApJ, 569, L83

Bacon, R., Accardo, M., Adjali, L., et al. 2010, in Society of Photo-Optical Instrumentation Engineers (SPIE) Conference Series, Vol. 7735, Proc. SPIE, 773508

Bartelmann, M., & Maturi, M. 2017, Scholarpedia, 12, 32440

Begeman, K. G. 1987, PhD thesis, University of Groningen, Kapteyn Astronomical Institute

—. 1989, A&A, 223, 47

Belfiore, F., Westfall, K. B., Schaefer, A., et al. 2019, AJ, 158, 160

Bershady, M. A., Verheijen, M. A. W., Westfall, K. B., et al. 2010, ApJ, 716, 234

Bi, D., Shlosman, I., & Romano-Díaz, E. 2022, ApJ, 934, 52

Binney, J., & Tremaine, S. 2008,

Bisaria, D., Spekkens, K., Huang, S., Hallenbeck, G., & Haynes, M. P. 2022, MNRAS, 509, 100

Blain, A. W. 2002, ApJ, 570, L51

Blanton, M. R., Kazin, E., Muna, D., Weaver, B. A., & Price-Whelan, A. 2011, AJ, 142, 31

Blanton, M. R., Bershady, M. A., Abolfathi, B., et al. 2017, AJ, 154, 28

Blitz, L., & Spergel, D. N. 1991, ApJ, 379, 631

Bloom, J. V., Croom, S. M., Bryant, J. J., et al. 2017, MNRAS, 472, 1809

Bocquet, S., Dietrich, J. P., Schrabback, T., et al. 2019, ApJ, 878, 55

Bundy, K., Bershady, M. A., Law, D. R., et al. 2015, ApJ, 798, 7

Bundy, K., Westfall, K., MacDonald, N., et al. 2019, FOBOS: A Next-Generation Spectroscopic Facility at the W. M. Keck Observatory, arXiv:1907.07195

Bureau, M., & Freeman, K. C. 1999, AJ, 118, 126

Burstein, D., Faber, S. M., Gaskell, C. M., & Krumm, N. 1984, ApJ, 287, 586

Cameron, E., Carollo, C. M., Oesch, P., et al. 2010, MNRAS, 409, 346

Cappellari, M., & Copin, Y. 2003, MNRAS, 342, 345

Cheung, E., Bundy, K., Cappellari, M., et al. 2016, Nature, 533, 504

Chun, M., Lu, J., Lai, O., et al. 2018, in Society of Photo-Optical Instrumentation Engineers (SPIE) Conference Series, Vol. 10703, Proc. SPIE, 107030J

Coelho, P., & Gadotti, D. A. 2011, ApJ, 743, L13

Contini, T., Epinat, B., Bouché, N., et al. 2016, A&A, 591, A49

Corsini, E. M. 2014, in Astronomical Society of the Pacific Conference Series, Vol. 486, Multi-Spin Galaxies, ed. E. Iodice & E. M. Corsini, 51

Courteau, S. 1997, AJ, 114, 2402

Crouse, D. F. 2016, IEEE Transactions on Aerospace and Electronic Systems, 52, 1679

de Burgh-Day, C. O., Taylor, E. N., Webster, R. L., & Hopkins, A. M. 2015, MNRAS, 451, 2161

Di Matteo, P., Haywood, M., Combes, F., Semelin, B., & Snaith, O. N. 2013, A&A, 553, A102

Diemer, B. 2018, ApJS, 239, 35

DiGiorgio, B., Bundy, K., Westfall, K. B., Leauthaud, A., & Stark, D. 2021, ApJ, 922, 116

Drory, N., MacDonald, N., Bershady, M. A., et al. 2015, AJ, 149, 77

Ellison, S. L., Nair, P., Patton, D. R., et al. 2011, MNRAS, 416, 2182

Elmegreen, B. G., Elmegreen, D. M., & Hirst, A. C. 2004, ApJ, 612, 191

Faber, S. M., Friel, E. D., Burstein, D., & Gaskell, C. M. 1985, ApJS, 57, 711

Feroz, F., Hobson, M. P., & Bridges, M. 2009, MNRAS, 398, 1601

Foreman-Mackey, D., Hogg, D. W., Lang, D., & Goodman, J. 2013, PASP, 125, 306

Fragkoudi, F., Athanassoula, E., & Bosma, A. 2016, MNRAS, 462, L41

Fraser-McKelvie, A., Merrifield, M., Aragón-Salamanca, A., et al. 2019, MNRAS, 488, L6

Fraser-McKelvie, A., Aragón-Salamanca, A., Merrifield, M., et al. 2020, MNRAS, 495, 4158

Freeman, K. C. 1970, ApJ, 160, 811

Friedli, D., Benz, W., & Kennicutt, R. 1994, ApJ, 430, L105

Frigo, M., & Johnson, S. G. 2005, Proceedings of the IEEE, 93, 216, special issue on "Program Generation, Optimization, and Platform Adaptation"

Gadotti, D. A., Seidel, M. K., Sánchez-Blázquez, P., et al. 2015, A&A, 584, A90

Garma-Oehmichen, L., Hernández-Toledo, H., Aquino-Ortíz, E., et al. 2022, MNRAS, 517, 5660

Gatti, M., Chang, C., Friedrich, O., et al. 2020, MNRAS, 498, 4060

Gavazzi, R., Adami, C., Durret, F., et al. 2009, A&A, 498, L33

Géron, T., Smethurst, R. J., Lintott, C., et al. 2023, MNRAS, 521, 1775

Glazebrook, K. 2013, PASA, 30, e056

González, J. J. 1993, PhD thesis, -

Gunn, J. E., Carr, M., Rockosi, C., et al. 1998, AJ, 116, 3040

Gunn, J. E., Siegmund, W. A., Mannery, E. J., et al. 2006, AJ, 131, 2332

Guo, Y., Jogee, S., Finkelstein, S. L., et al. 2023a, ApJ, 945, L10

—. 2023b, ApJ, 945, L10

Gurri, P., Taylor, E. N., & Fluke, C. J. 2020, MNRAS, arXiv:2009.10067

—. 2021, MNRAS, arXiv:2012.09175

Harris, C. R., Millman, K. J., van der Walt, S. J., et al. 2020, Nature, 585, 357

Hartke, J., Kakkad, D., Reyes, C., et al. 2020, in Society of Photo-Optical Instrumentation Engineers (SPIE) Conference Series, Vol. 11448, Society of Photo-Optical Instrumentation Engineers (SPIE) Conference Series, 114480V

Häussler, B., McIntosh, D. H., Barden, M., et al. 2007, ApJS, 172, 615

Hikage, C., Oguri, M., Hamana, T., et al. 2019, PASJ, 71, 43

Holmes, L., Spekkens, K., Sánchez, S. F., et al. 2015, MNRAS, 451, 4397

Hubble, E. P. 1926, ApJ, 64, 321

Huff, E., Eifler, T., Krause, E., et al. 2019, BAAS, 51, 423

Huff, E. M., Krause, E., Eifler, T., et al. 2013, arXiv e-prints, arXiv:1311.1489

Hunter, J. D. 2007, Computing in Science & Engineering, 9, 90

Ivezić, Ž., Kahn, S. M., Tyson, J. A., et al. 2019, ApJ, 873, 111

Józsa, G. I. G., Kenn, F., Klein, U., & Oosterloo, T. A. 2007, A&A, 468, 731

Kormendy, J., & Kennicutt, Robert C., J. 2004, ARA&A, 42, 603

Krajnović, D., Cappellari, M., de Zeeuw, P. T., & Copin, Y. 2006a, MNRAS, 366, 787

—. 2006b, MNRAS, 366, 787

Krause, E., Eifler, T. F., Zuntz, J., et al. 2017, arXiv e-prints, arXiv:1706.09359

Krishnarao, D., Tremonti, C., Fraser-McKelvie, A., et al. 2020, ApJ, 898, 116

Kruk, S. J., Lintott, C. J., Bamford, S. P., et al. 2018, MNRAS, 473, 4731

Kubryk, M., Prantzos, N., & Athanassoula, E. 2013, MNRAS, 436, 1479

Kuijken, K., Heymans, C., Hildebrandt, H., et al. 2015, MNRAS, 454, 3500

Lambas, D. G., Maddox, S. J., & Loveday, J. 1992, MNRAS, 258, 404

Laureijs, R., Amiaux, J., Arduini, S., et al. 2011, arXiv e-prints, arXiv:1110.3193

Law, D. R., Steidel, C. C., Erb, D. K., et al. 2009, ApJ, 697, 2057

Law, D. R., Cherinka, B., Yan, R., et al. 2016, AJ, 152, 83

Leauthaud, A., Tinker, J., Bundy, K., et al. 2012, ApJ, 744, 159

Mahler, G., Richard, J., Clément, B., et al. 2018, MNRAS, 473, 663

Mandelbaum, R. 2018, ARA&A, 56, 393

Mandelbaum, R., Seljak, U., Cool, R. J., et al. 2006, MNRAS, 372, 758

Masters, K. L., Nichol, R. C., Hoyle, B., et al. 2011, MNRAS, 411, 2026

Masters, K. L., Nichol, R. C., Haynes, M. P., et al. 2012, MNRAS, 424, 2180

Masters, K. L., Krawczyk, C., Shamsi, S., et al. 2021, MNRAS, 507, 3923

Melvin, T., Masters, K., Lintott, C., et al. 2014, MNRAS, 438, 2882

Minchev, I., & Famaey, B. 2010, ApJ, 722, 112

Miralda-Escude, J. 1991, ApJ, 370, 1

Morales, M. F. 2006, ApJ, 650, L21

Moré, J. J. 1978, in Numerical Analysis, ed. G. A. Watson (Berlin, Heidelberg: Springer Berlin Heidelberg), 105–116

Nair, P. B., & Abraham, R. G. 2010, ApJ, 714, L260

Navarro, J. F., Frenk, C. S., & White, S. D. M. 1997, ApJ, 490, 493

Newnham, L., Hess, K. M., Masters, K. L., et al. 2020, MNRAS, 492, 4697

Oort, J. H. 1932, Bull. Astron. Inst. Netherlands, 6, 249

—. 1940, ApJ, 91, 273

Padilla, N. D., & Strauss, M. A. 2008, MNRAS, 388, 1321

Peng, C. Y., Ho, L. C., Impey, C. D., & Rix, H.-W. 2002, AJ, 124, 266

Pérez, I., Sánchez-Blázquez, P., & Zurita, A. 2009, A&A, 495, 775

Persic, M., Salucci, P., & Stel, F. 1996, MNRAS, 281, 27

Planck Collaboration, Aghanim, N., Akrami, Y., et al. 2018, arXiv e-prints,

arXiv:1807.06209

Regan, M. W., Vogel, S. N., & Teuben, P. J. 1997, ApJ, 482, L143

Rosas-Guevara, Y., Bonoli, S., Dotti, M., et al. 2022, MNRAS, 512, 5339

Roy, N., Bundy, K., Nevin, R., et al. 2021, ApJ, 913, 33

Rubin, V. C., Ford, W. K., J., & Thonnard, N. 1978, ApJ, 225, L107

—. 1980, ApJ, 238, 471

Sánchez-Blázquez, P., Ocvirk, P., Gibson, B. K., Pérez, I., & Peletier, R. F. 2011, MNRAS, 415, 709

Schoenmakers, R. H. M., Franx, M., & de Zeeuw, P. T. 1997, MNRAS, 292, 349

Seidel, M. K., Falcón-Barroso, J., Martínez-Valpuesta, I., et al. 2016, MNRAS, 460, 3784

Sellwood, J. A., & Sánchez, R. Z. 2010, MNRAS, 404, 1733

Sellwood, J. A., & Spekkens, K. 2015, arXiv e-prints, arXiv:1509.07120

Sellwood, J. A., & Wilkinson, A. 1993, Reports on Progress in Physics, 56, 173

Sheth, K., Elmegreen, D. M., Elmegreen, B. G., et al. 2008, ApJ, 675, 1141

Skilling, J. 2004, in American Institute of Physics Conference Series, Vol. 735, Bayesian Inference and Maximum Entropy Methods in Science and Engineering: 24th International Workshop on Bayesian Inference and Maximum Entropy Methods in Science and Engineering, ed. R. Fischer, R. Preuss, & U. V. Toussaint, 395–405

Skilling, J. 2006, Bayesian Analysis, 1, 833

Slipher, V. M. 1913, Lowell Observatory Bulletin, 2, 56

—. 1914, Lowell Observatory Bulletin, 2, 66

Sofue, Y., & Rubin, V. 2001, ARA&A, 39, 137

Speagle, J. S. 2020, MNRAS, 493, 3132

Spekkens, K., & Sellwood, J. A. 2007, ApJ, 664, 204

Spergel, D., Gehrels, N., Baltay, C., et al. 2015, arXiv e-prints, arXiv:1503.03757

Stark, D. V., Bundy, K. A., Westfall, K., et al. 2018, MNRAS, 480, 2217

Teuben, P. J. 2002, in Astronomical Society of the Pacific Conference Series, Vol. 275, Disks of Galaxies: Kinematics, Dynamics and Peturbations, ed. E. Athanassoula, A. Bosma, & R. Mujica, 217–228

Tokuoka, T., Inoue, A. K., Hashimoto, T., et al. 2022, ApJ, 933, L19

Toomre, A. 1981, in Structure and Evolution of Normal Galaxies, ed. S. M. Fall & D. Lynden-Bell, 111–136

Trager, S. C., Worthey, G., Faber, S. M., Burstein, D., & González, J. J. 1998, ApJS, 116, 1

Tremaine, S., & Weinberg, M. D. 1984, ApJ, 282, L5

Troxel, M. A., & Ishak, M. 2015, Phys. Rep., 558, 1

Troxel, M. A., MacCrann, N., Zuntz, J., et al. 2018, Phys. Rev. D, 98, 043528

Tully, R. B., & Fisher, J. R. 1977, A&A, 500, 105

Umetsu, K., Medezinski, E., Nonino, M., et al. 2014, ApJ, 795, 163

Umetsu, K., Sereno, M., Tam, S.-I., et al. 2018, ApJ, 860, 104

Varidel, M. R., Croom, S. M., Lewis, G. F., et al. 2019, MNRAS, 485, 4024

Virtanen, P., Gommers, R., Oliphant, T. E., et al. 2020, Nature Methods, 17, 261

Wake, D. A., Bundy, K., Diamond-Stanic, A. M., et al. 2017, AJ, 154, 86

Warner, P. J., Wright, M. C. H., & Baldwin, J. E. 1973, MNRAS, 163, 163

Weijmans, A.-M., de Zeeuw, P. T., Emsellem, E., et al. 2014, MNRAS, 444, 3340

Weinberg, D. H., Mortonson, M. J., Eisenstein, D. J., et al. 2013, Phys. Rep., 530, 87

Westfall, K. B., Cappellari, M., Bershady, M. A., et al. 2019, arXiv e-prints, arXiv:1901.00856

Williams, M. J., Bureau, M., & Kuntschner, H. 2012, MNRAS, 427, L99

Wittman, D., & Self, M. 2021, ApJ, 908, 34

Worthey, G., Faber, S. M., Gonzalez, J. J., & Burstein, D. 1994, ApJS, 94, 687

Yan, R., Bundy, K., Law, D. R., et al. 2016, AJ, 152, 197

York, D. G., Adelman, J., Anderson, John E., J., et al. 2000, AJ, 120, 1579

Yu, S.-Y., Kalinova, V., Colombo, D., et al. 2022, A&A, 666, A175